DEVELOPMENT OF A FINITE STATE COAXIAL ROTOR DYNAMIC INFLOW MODEL

A Thesis
Presented to
The Academic Faculty

by

Yong-Boon Kong

In Partial Fulfillment
of the Requirements for the Degree
Doctor of Philosophy in the
School of Aerospace Engineering

Georgia Institute of Technology
August 2018

DEVELOPMENT OF A FINITE STATE COAXIAL ROTOR DYNAMIC INFLOW MODEL

Approved by:

Dr. J.V.R. Prasad, Advisor
School of Aerospace Engineering
Georgia Institute of Technology

Dr. Daniel P. Schrage
School of Aerospace Engineering
Georgia Institute of Technology

Dr. Lakshmi N. Sankar
School of Aerospace Engineering
Georgia Institute of Technology

Dr. David A. Peters
Mechanical Engineering & Material Science
Washington University in St. Louis

Dr. Marilyn J. Smith
School of Aerospace Engineering
Georgia Institute of Technology

Date Approved: July 2nd 2018

To my parents and brother for all their love and support

And to my friends who accompanied me through this journey

ACKNOWLEDGEMENTS

This study is supported under the NRTC Vertical Lift Rotorcraft Center of Excellence (VLRCOE) from the U.S. Army Aviation and Missile Research, Development and Engineering Center (AMRDEC) under Technology Investment Agreement W911W6-17-2-0002, entitled Georgia Tech Vertical Lift Research Center of Excellence (GT-VLRCOE) with Dr. Mahendra Bhagwat as the Program Manager. I would like to acknowledge that this research and development was accomplished with the support and guidance of the NRTC.

I would like to thank my thesis advisor Dr. J. V. R. Prasad for his excellent guidance as both an advisor and mentor. I would also like to thank Dr. David A. Peters and Dr. Xin Hong for their guidance and mentorship. Furthermore, I would like to thank my other committee members Dr. Lakshmi N. Sankar, Dr. Marilyn J. Smith and Dr. Daniel P. Schrage for their support, feedback and the opportunity to work with them.

I would like to thank Dr. Chengjian He, Mr. Weibin Chen, and the rest of the team at Advanced Rotorcraft Technilogy for their technical support with FLIGHTLAB®. I would like to thank my friends, colleagues and collaborators that have supported me throughout my graduate studies: Dr. Reema Kundu, Dr. Jee Woong Kim, Dr. Mark Joseph Santos Lopez, Mr. Juan Pablo Afman, Mr. Satyam Patel, Mr. Abhishek, Mishra, Mr. Feyyaz Guner, Mr. Robert A. Walters, Mr. Ian A. Movius, Mr. Chams Eddine Mballo, Ms. Vinodhini Comandur and Ms. Chong Zhou.

Finally, I would like to thank my father Mike, my mother Siang Keng, and my brother Yong Loon for always believing in me and providing unconditional love and support.

TABLE OF CONTENTS

LIST OF TABLES

LIST OF FIGURES

LIST OF SYMBOLS AND ABBREVIATIONS

Greek symbols

λ_0	Uniform induced inflow coefficient
λ_{1c}	First harmonic fore-to-aft induced inflow variation coefficient
λ_{1s}	First harmonic side-to-side induced inflow variation coefficient
α_j^{rc}	Cosine part of inflow states
α_j^{rs}	Sine part of inflow states
$\chi_{\mathbf{mom}}$	Momentum wake skew angle, $\tan^{-1}\left(\frac{\mu}{\lambda_f+\lambda_m}\right)$
δ_n^j	Kroneckter delta
λ_f	Inflow due to free-stream, $V_\infty \cos\chi$
λ_m	Momentum theory inflow at rotor normalised by ΩR
μ	Advance ratio, $V_\infty \sin\chi$
$\nu, \eta, \bar{\psi}$	Ellipsoidal coordinates
Ω	Rotor rotational speed, rad/s
Φ	Pressure potential normalised by $\rho\Omega^2R^2$
Ψ_j^r	Radial shaping function
$\bar{\Psi}_q$	Azimuth of q^{th} blade, rads
ρ	Air density, slug/ft^3
τ_n^{mc}	Cosine part of pressure coefficients
τ_n^{ms}	Sine part of pressure coefficients
ξ	Streamline coordinates

Letter symbols

$\mathbf{C_L}$	Roll moment coefficient
$\mathbf{C_M}$	Pitch moment coefficient
$\mathbf{C_T}$	Thrust coefficient

$\bar{d}, \bar{l}, \bar{h}$	Relative separation distances between 'active' and 'receiving' rotors normalised by R along $\bar{x}, \bar{y}, \bar{z}$, respectively
$[E]$	Inverse of pressure potential superposition inflow model apparent mass matrix, $[E] = [M]^{-1}$
$[L]$	Influence coefficient matrix of pressure potential superposition inflow model
$[M]$	Apparent mass matrix of pressure potential superposition inflow model
M	Total number of harmonics terms
N	Total number of radial terms
$\bar{P}_n^m$	Normalized Legendre function of the first kind
$\bar{Q}_n^m$	Normalized Legendre function of the second kind
L_q	Blade sectional circulatory lift, lbf/ft
Q	Number of blades on one rotor
q	Blade index on rotor
R	Rotor radius, ft
$\bar{r}$	Blade radial coordinate normalised by R
t	Time, seconds
$\bar{t}$	Nondimensional time, Ωt
$\bar{u}, \bar{v}, \bar{w}$	Velocity components normalised by ΩR
$\vec{v}$	Perturbation velocity vector normalised by ΩR
V_∞	Free-stream velocity normalised by ΩR
$[V_m]$	Mass flow parameter
$\mathbf{X_{skew}}$	Wake skew function, $\tan\left(\frac{\chi_{\text{mom}}}{2}\right)$
$\bar{x}, \bar{y}, \bar{z}$	Rotor disk coordinates normalised by R

Operator

$\left(^*\right)$	Derivative with respect to nondimensional time, $\bar{t}$
$\vec{\nabla}$	Gradient operator

Subscript

$()_1$ Upper rotor coordinate system

$()_2$ Lower rotor coordinate system

Superscript

$()^A$ Part of pressure due to unsteadiness

$()^V$ Part of pressure due to convection

Abbreviations

MUAD Maximum Unnoticable Added Dynamics

PPSIM Pressure Potential Superposition Inflow Model

VVPM Viscous Vortex Particle Method

SUMMARY

Accurate modeling of rotor inflow dynamics in flight simulations is crucial for rotorcraft performance and handling qualities evaluations. Both Pitt-Peters and Peters-He inflow models are used to predict induced inflow distribution of a single rotor configuration. For coaxial rotor system, most published work focus on performance related studies (both experimental and numerical simulations), which are not compatible for use in real-time rotor inflow simulations. A novel approach to formulate a coaxial rotor inflow model from first principles by superposition of upper and lower rotor pressure potentials is explored in this thesis. By representing both rotors' pressure and downwash in terms of harmonic and radial expansion terms, a finite state coaxial rotor inflow model known as the Pressure Potential Superposition Inflow Model (PPSIM) is developed. Steady hover inflow predictions from PPSIM match well with results obtained from GT-Hybrid and the Viscous Vortex Particle Method (VVPM), but differences in inflow distributions are observed in steady forward flight. This is attributed to wake contractions/distortions and other real flow effects which PPSIM does not account for.

In order to identify and incorporate real flow effects into coaxial rotor PPSIM, VVPM induced inflow results are used for system identification. The influence coefficient matrix or L-matrix is extracted from VVPM steady-state change in pressure coefficients and inflow states using the least-square-fit method. The extracted L-matrix is then compared against the original PPSIM L-matrix for calculating correction to each element in the L-matrix. Inflow states from the L-matrix corrected PPSIM show good correlations with VVPM inflow data, capturing wake contractions/distortions,

wake diffusion and swirl effects in its new L-matrix. It is also found that these correction terms are insensitive to different upper and lower rotor thrust loading conditions. A second order curve-fitted correlations between elements in the L-matrix correction terms and rotor wake skew functions are found to simplify its implementation into the original coaxial rotor PPSIM L-matrix.

While corrections to PPSIM L-matrix improves its steady-state inflow state correlations with VVPM data, it increases phase differences between the two models when comparing their frequency responses. To address this issue, elements in the off-diagonal apparent mass matrix (M-matrix) blocks are modified. A system identification tool, CIFER® is used to minimize the cost function between L-matrix corrected PPSIM and VVPM frequency response data over 0.35∼5.0 rad/s, which is sufficient for flight dynamics analysis. Average cost functions corresponding to the original PPSIM, L-matrix corrected PPSIM and the newly improved PPSIM (L-matrix corrections and modifications to off-diagonal M-matrix blocks) are compared for hover and various advance ratios. In each comparison, the improved PPSIM has the lowest average magnitude and phase cost functions; indicating that it has the best match with VVPM frequency response data.

The improved coaxial rotor PPSIM correctly captures complex rotor-to-rotor aerodynamic coupling effects in its inflow equation and can be easily implemented for computer simulations. Furthermore, since the corrections and modifications are applied to the L- and M-matrices, respectively, its state-space structure is preserved. This means that the improved PPSIM can also be used for eigenvalue analysis as well as control law development in coaxial rotor aeromechanics problems.

CHAPTER I

INTRODUCTION

1.1 Motivation and background

Rotary-wing aerodynamics modeling is more complicated compared to their fixed-wing counterpart due to the fact that vortices generated by rotor blades remain in close proximity for a significant amount of time, inducing flow changes at the rotor. Spatial variation of rotor inflow has significant effects on rotor performance metrics such as thrust generation and power consumption. In addition, time variations of rotor inflow impact rotor dynamic stability and vehicle flight dynamics [5]. As such, accurate modeling of induced inflow variations with time and across the rotor disk is one of the key elements in real-time rotorcraft flight simulation for both performance and handling qualities evaluations. Inflow predictions based on momentum theory give excellent results in hover, but are clearly inadequate in forward flight [30, 32]. On the other hand, vorticity-based method models such as the Viscous Vortex Particle Method (VVPM) [11, 10], VorTran-M/VorTran-M2 [44, 45, 46, 43] and GT-Hybrid [27] provide a higher level of sophistication in inflow modeling. While these approaches give accurate inflow predictions across the rotor disk, the computational effort needed to calculate the solutions makes them difficult for use in real-time flight simulations.

In the 1980s, Pitt and Peters developed a three-state dynamic inflow model (Pitt-Peters inflow model) from potential flow theory [36] that relates transient rotor loads such as thrust, aerodynamic roll moment and pitch moment to the overall inflow responses across the rotor. Peters and He later generalized the Pitt-Peters model with an arbitrary number of inflow harmonics and radial terms to develop what is

now known as the Peters-He inflow model [8, 31]. Inflow distribution predictions from the Peters-He inflow model correlate well with the Laser Doppler Velocimetry (LDV) inflow measurements of an isolated rotor collected at NASA Langely wind tunnel for various advance ratios [35]. One key aspect of Pitt-Peters and Peters-He inflow models is that they are computationally efficient compared to other higher fidelity models, yet still able to predict rotor inflows with reasonable accuracy. The Pitt-Peters and Peters-He inflow models are widely used in standard rotorcraft flight simulation software such as FLIGHTLAB® [3] and Rotorcraft Comprehensive Analysis System (RCAS) [41]. Furthermore, these dynamic inflow models are structured in state-space form which is compatible for control law development and aeromechanics analysis [33]. One limitation of the Pitt-Peters and Peters-He inflow models is that they are restricted to modeling of inflows for helicopters with single rotor configuration. For multi-rotor configurations such as a coaxial rotor system, other methods to model the inflows are needed.

1.2 Literature review

Most recent published work on coaxial rotor configurations are limited to performance related experimental and numerical studies [4, 6, 13, 21, 23, 24], which are not suitable for real-time simulation of rotor inflows. The main challenge in coaxial rotor inflow modeling is to account for mutual aerodynamic interference effects between upper and lower rotors as shown in simulation studies using OVERFLOW by Yoon [49, 48]. One approach to overcome this issue is to employ system identification techniques on an actual coaxial rotor vehicle and extract relevant dynamic models from input-output flight data [15, 20]. Frequency sweeps covering the range of interests are applied to the vehicle (without any stability augmentation) collective, cyclic and pedal controls. The resulting responses such as hub moments and body rates are recorded and filtered to remove sensor noises. Control signals and filtered sensor measurements are input

into software such as CIFER® [40] to extract transfer functions that are used to model the vehicle dynamics, which include the effect of upper and lower rotor aerodynamic interference. However, such methodology is only feasible for small scale coaxial rotor Unmanned Aerial Vehicles (UAVs) where cost and level of complexity in conducting flight tests are relatively low. For inflow modeling of full scale coaxial rotor vehicles, such as Sikorsky S-97 Raider, mathematical models are still the desirable option.

Zhao and He [50] enhanced the finite state dynamic wake model with VVPM results, to account for the complex aerodynamic interference inherent to coaxial rotor configuration. Downwash across each rotor is modeled using the Peters-He inflow model with augmentations to the influence coefficient matrix and mass flow parameter extracted from inflow results of a coaxial rotor model developed in VVPM simulation. Wake distortion effects are accounted for by introducing corrections to each rotor's influence coefficient matrix while the impact of other rotor on its mass flow parameter is captured by a parameter which depends on both the wake skew angle and vertical separation distance between upper and lower rotors. By adopting this approach, state-space form of the finite state inflow model is preserved while first order effect of mutual aerodynamic interference on rotor inflows is captured through augmentations to the upper and lower rotor influence coefficient matrices and mass flow parameters.

Similar to the work by Zhao, Xin et al. [47] modeled inflows across each rotor in a coaxial rotor configuration using the Pitt-Peters inflow model. The key difference is that no augmentations are applied to the influence coefficient matrices nor the mass flow parameters in the upper and lower rotor inflow equations. Instead, off-rotor induced velocities computed from inflow equations with the same state-space structure as the Pitt-Peters model are used. The apparent mass and influence coefficient matrices for the off-disk inflow equations are extracted from induced velocities corresponding to a plane above or below a single rotor model developed using a free-vortex wake model. For example, off-disk inflow equation corresponding to a plane below

the rotor is used to calculate interference velocities on the lower rotor based on upper rotor pressure loading, and vice-versa. Steady rotor downwash results from the free-vortex model are used to calculate the influence coefficient matrices corresponding to each plane. The apparent mass matrix for each plane is identified from time history data of mean downwash (or downwash gradients) and thrust (or hub moments) in response to step input of collective (or cyclic pitch angles) settings of a single rotor model. The identified apparent mass and influence coefficient matrices are precalculated and stored in a look-up table indexed by wake skew state and disk loading for use in real-time flight simulations.

In the recent work by Rand et al. [38, 37], system identification techniques are used to extract a finite state inflow model using results obtained from a free-wake model. The inflow equation is similar to Pitt-Peters except that elements in the M- and L-matrices are identified using frequency analysis. First, single frequency periodic excitation is individually applied to each forcing component (C_T, C_L, C_M) on each rotor in the free-wake model. Inflow variations (λ_0, λ_{1c}, λ_{1s},) are computed from time histories of the rotor inflow distributions predicted by the free-wake model. Both cosine and sine terms are then extracted from the inflow variations using FFT which are then used to identified elements in the M- and L-matrices at a given frequency. This process is repeated across a range of frequencies to compute average values in the M- and L-matrices.

On a similar token, He et al. [9] formulated a state-space rotor induced inflow model for predicting lower rotor induced inflows using upper rotor inflow states. The model parameters are identified using induced inflow data from VVPM simulation runs. Pressure loading perturbations using a sinusoidal frequency sweep from steady-state is first injected to the upper rotor. Induced velocity time histories at both rotors are sampled and converted to inflow states. These signals are then input to CIFER®

for identifying parameters in the state-space model which outputs interference velocities at the lower rotor based on upper rotor inflow states. Similarly, a state-space model for computing upper rotor interference induced velocities are also identified by perturbing lower rotor pressure loading.

Although the work by Zhao and Xin have shown some promising results in modeling inflows of a coaxial rotor configuration, the governing equations they used are loosely based on finite state single rotor inflow models. Both the augmentation and off-rotor induced velocities approaches are somewhat ad hoc methods to include mutual interference effects inherent in coaxial rotor systems into a single rotor inflow model. The black-box system identification approach by Rand and He provided limited insights on the complex mutual interference effects within a coaxial rotor system. A more general approach to model coaxial rotor inflows is to develop a finite state dynamic inflow model analytically from first principles, taking into account the rotors' interference effects in the inflow equation.

1.3 Objective

It can be concluded from the literature reviews conducted in section 1.2 that more work are still needed to model rotor inflows beyond single rotor configurations in real-time flight simulations. As such, the purpose of this thesis is to develop methodologies for modeling rotor inflows of a coaxial rotor system. Specifically, the following objectives are to be examined,

1. Develop a finite state coaxial rotor dynamic inflow model from first principles.

2. Evaluate steady inflow predictions from the coaxial rotor inflow model against results from higher fidelity models.

3. Incorporate real flow effects, such as wake contractions/distortions and diffusion into the coaxial rotor inflow model and re-evaluate its steady-state responses.

4. Improve dynamic characteristics of the coaxial rotor inflow model through correlations with higher fidelity model frequency responses.

CHAPTER II

FINITE STATE DYNAMIC INFLOW MODEL

In formulating the finite state dynamic inflow model, it is assumed that wakes generated by rotor disks are incompressible. In addition, flows around the actuator disks are assumed to be irrotational, i.e. no viscous effects.

2.1 Governing equations

The continuity and momentum equations are simplified for flows that are incompressible, inviscid and irrotational

$$\vec{\nabla} \cdot \vec{v} = 0 \tag{1}$$

$$\frac{\partial \vec{v}}{\partial \bar{t}} - V_\infty \frac{\partial \vec{v}}{\partial \xi} = -\vec{\nabla}\Phi \tag{2}$$

where $\vec{v}$ is the perturbation velocity vector, $\bar{t}$ is the non-dimensional time, V_∞ is the free-stream velocity, ξ is the streamline coordinates and Φ is the pressure. From the momentum equation shown in Eq. (2), it is observed that spatial variation of pressure can be considered as the superposition of contributions from a term due to local unsteadiness of the flow field and another term due to gradient of velocity along the streamline coordinates (convection). As such, the pressure term is divided into two parts; one part due to unsteadiness (Φ^A) and one part due to convection (Φ^V) as shown

$$\Phi = \Phi^A + \Phi^V \tag{3}$$

In a multi-rotor system, pressure experienced by a rotor is the sum of its own pressure and all other rotor pressure fields. As a consequence, the momentum equation

corresponding to a multi-rotor configuration is rewritten as

$$\frac{\partial \vec{v}}{\partial \bar{t}} - V_\infty \frac{\partial \vec{v}}{\partial \xi} = -\vec{\nabla}(\Phi_1 + \Phi_2 + \ldots + \Phi_K) \tag{4}$$

where the subscripts '1' and 'K' in the pressure terms refer to rotor-1 and rotor-K coordinates, respectively. Next, substitute the pressure term in Eq. (3) corresponding to each rotor into Eq. (4) which results in two equations to be solved separately

$$-\frac{\partial \vec{v}}{\partial \bar{t}} = \vec{\nabla}(\Phi_1 + \Phi_2 + \ldots + \Phi_K)^A \tag{5}$$

$$V_\infty \frac{\partial \vec{v}}{\partial \xi} = \vec{\nabla}(\Phi_1 + \Phi_2 + \ldots + \Phi_K)^V \tag{6}$$

By taking the gradients of Eqs. (5) and (6) and using the continuity equation in Eq. (1), it is clear to see that each part of the total pressure, $(\Phi_1 + \Phi_2 + \ldots + \Phi_K)^A$ and $(\Phi_1 + \Phi_2 + \ldots + \Phi_K)^V$ satisfy the Laplace's equation

$$\vec{\nabla}^2(\Phi_1 + \Phi_2 + \ldots + \Phi_K)^A = 0 \tag{7}$$

$$\vec{\nabla}^2(\Phi_1 + \Phi_2 + \ldots + \Phi_K)^V = 0 \tag{8}$$

Thus, the term $(\Phi_1 + \Phi_2 + \ldots + \Phi_K)$ also satisfies the Laplace equation which implies that Φ_1, Φ_2, ..., Φ_K can be represented as potential functions

$$\begin{aligned} \vec{\nabla}^2\Phi_1 &= 0 \\ \vec{\nabla}^2\Phi_2 &= 0 \\ &\vdots \\ \vec{\nabla}^2\Phi_K &= 0 \end{aligned} \tag{9}$$

2.2 Pressure potential and inflow distribution expansions

Now rewrite Eq. (9) in ellipsoidal coordinates $(\nu, \eta, \bar{\psi})$, the Laplace's equations associated with a circular disk is solved analytically by separation of variables method

(see Appendix A) yielding

$$\Phi_1 = \sum_{m=0}^{M} \sum_{n=m+1,m+3...}^{N} \bar{P}_n^m(\nu_1)\bar{Q}_n^m(i\eta_1)[(\tau_n^{mc})_1 \cos(m\bar{\psi}_1) + (\tau_n^{ms})_1 \sin(m\bar{\psi}_1)] \quad (10)$$

$$\Phi_2 = \sum_{m=0}^{M} \sum_{n=m+1,m+3...}^{N} \bar{P}_n^m(\nu_2)\bar{Q}_n^m(i\eta_2)[(\tau_n^{mc})_2 \cos(m\bar{\psi}_2) + (\tau_n^{ms})_2 \sin(m\bar{\psi}_2)]$$

$$\vdots$$

$$\Phi_K = \sum_{m=0}^{M} \sum_{n=m+1,m+3...}^{N} \bar{P}_n^m(\nu_K)\bar{Q}_n^m(i\eta_K)[(\tau_n^{mc})_K \cos(m\bar{\psi}_K) + (\tau_n^{ms})_K \sin(m\bar{\psi}_K)]$$

where $\bar{P}_n^m$ and $\bar{Q}_n^m$ are associated Legendre functions of the first and second kind, respectively; τ_n^{mc} and τ_n^{ms} are cosine and sine parts of the pressure coefficients, respectively. In Eq. (10), all terms with even values of $n+m$ are discarded because $\bar{P}_n^m(\nu)$ do not match the boundary condition of zero pressure at the disk edge. In addition, terms of type $\bar{P}_n^m(i\nu)$ and $\bar{Q}_n^m(\eta)$ are rejected as they do not give zero pressure at infinity.

The pressure coefficients, τ_n^{mc} and τ_n^{ms} are calculated from blade sectional circulatory lift, L_q (that can be evaluated from any lifting theory) using the following equations [34]

$$\tau_n^{0c} = \frac{1}{2\pi} \sum_{q=1}^{Q} \int_0^1 \frac{L_q}{\rho\Omega^2 R^3} \Psi_n^0(\bar{r}) d\bar{r} \quad (11)$$

$$\tau_n^{mc} = \frac{1}{\pi} \sum_{q=1}^{Q} \int_0^1 \frac{L_q}{\rho\Omega^2 R^3} \Psi_n^m(\bar{r}) d\bar{r} \cos(m\bar{\Psi}_q) \quad (12)$$

$$\tau_n^{ms} = \frac{1}{\pi} \sum_{q=1}^{Q} \int_0^1 \frac{L_q}{\rho\Omega^2 R^3} \Psi_n^m(\bar{r}) d\bar{r} \sin(m\bar{\Psi}_q) \quad (13)$$

where Q is the total number of blades, q is the blade index, ρ is air density, Ω is the rotor's rotational speed, R is rotor radius, $\bar{r}$ is the non-dimensional blade radial coordinate, $\bar{\Psi}_q$ is azimuth of the q^{th} blade and Ψ_n^m is an arbitrary radial distribution function (or shaping function).

In order to establish a relation between induced downwash across lifting rotors and pressure loading on the blades, induced flow distribution for each rotor is represented

in terms of a harmonic variation in azimuth and a shaping function, Ψ_j^r; analogous to the expansion used for the pressure potentials

$$\begin{aligned}
\bar{w}_1 &= \sum_{r=0}^{M} \sum_{j=r+1,r+3\ldots}^{N} \Psi_j^r(\nu_1)[(\alpha_j^{rc})_1 \cos(r\bar{\psi}_1) + (\alpha_j^{rs})_1 \sin(r\bar{\psi}_1)] \\
\bar{w}_2 &= \sum_{r=0}^{M} \sum_{j=r+1,r+3\ldots}^{N} \Psi_j^r(\nu_2)[(\alpha_j^{rc})_2 \cos(r\bar{\psi}_2) + (\alpha_j^{rs})_2 \sin(r\bar{\psi}_2)] \\
&\vdots \\
\bar{w}_K &= \sum_{r=0}^{M} \sum_{j=r+1,r+3\ldots}^{N} \Psi_j^r(\nu_K)[(\alpha_j^{rc})_K \cos(r\bar{\psi}_K) + (\alpha_j^{rs})_K \sin(r\bar{\psi}_K)]
\end{aligned} \tag{14}$$

where $\bar{w}_1$ and $\bar{w}_K$ are downwash corresponding to rotor-1 and rotor-K, respectively; α_j^{rc} and α_j^{rs} are unknown induced inflow states corresponding to the cosine and sine terms, respectively. Notice from Eq. (14) that the total number of harmonic terms, M and radial terms, N are the same as the pressure potential expansions. This is necessary to relate all unknown inflow states to known pressure coefficient terms so that induced downwash can be calculated from given rotor pressure loading. It is found that the following shaping function provides good on-disk downwash predictions [28]

$$\Psi_j^r(\nu) = \frac{\bar{P}_j^r(\nu)}{\nu} \tag{15}$$

2.3 Multi-Rotor Pressure Potential Superposition Inflow Model (PPSIM)

The next step is to substitute all rotors' pressure potential in Eq. (10) and downwash expansions from Eqs. (14) into the z-component of Eq. (5). By making use of the orthogonality properties of associated Legendre functions of the first kind (see

Appendix B) and trigonometric functions, the resulting equations are

$$\begin{aligned}
\{\overset{*}{\alpha}_1\} &= \frac{E_{11}}{2}\{\tau_1^A\} + \frac{E_{12}}{2}\{\tau_2^A\} + \ldots + \frac{E_{1K}}{2}\{\tau_K^A\} \\
\{\overset{*}{\alpha}_2\} &= \frac{E_{21}}{2}\{\tau_1^A\} + \frac{E_{22}}{2}\{\tau_2^A\} + \ldots + \frac{E_{2K}}{2}\{\tau_K^A\} \\
&\vdots \\
\{\overset{*}{\alpha}_K\} &= \frac{E_{K1}}{2}\{\tau_1^A\} + \frac{E_{K2}}{2}\{\tau_2^A\} + \ldots + \frac{E_{KK}}{2}\{\tau_K^A\}
\end{aligned} \tag{16}$$

where $\{\alpha\}$ and $\{\tau\}$ are column vectors consisting of both cosine and sine terms as shown in Eqs. (17) and (18), respectively; $E_{11}, E_{12}, \ldots, E_{KK}$ are linear operations on $\{\tau^A\}$ to obtain $\{\overset{*}{\alpha}\}$.

$$\{\alpha_i\} := \begin{Bmatrix} (\alpha_j^{rc})_i \\ (\alpha_j^{rs})_i \end{Bmatrix} \quad r = 0, 1 \ldots M; \quad j = r+1, r+3 \ldots N \tag{17}$$

$$\{\tau_i\} := \begin{Bmatrix} (\tau_n^{mc})_i \\ (\tau_n^{ms})_i \end{Bmatrix} \quad m = 0, 1 \ldots M; \quad n = m+1, m+3 \ldots N; \quad i = 1, 2, \ldots K \tag{18}$$

Similarly, substitute Eqs. (10) and (14) into the z-component of the convective term in Eq. (6) and using the orthogonality properties, results in the following equations

$$\begin{aligned}
V_\infty\{\alpha_1\} &= \frac{L_{11}}{2}\{\tau_1^V\} + \frac{L_{12}}{2}\{\tau_2^V\} + \ldots + \frac{L_{1K}}{2}\{\tau_K^V\} \\
V_\infty\{\alpha_2\} &= \frac{L_{21}}{2}\{\tau_1^V\} + \frac{L_{22}}{2}\{\tau_2^V\} + \ldots + \frac{L_{2K}}{2}\{\tau_K^V\} \\
&\vdots \\
V_\infty\{\alpha_K\} &= \frac{L_{K1}}{2}\{\tau_1^V\} + \frac{L_{K2}}{2}\{\tau_2^V\} + \ldots + \frac{L_{KK}}{2}\{\tau_K^V\}
\end{aligned} \tag{19}$$

where $L_{11}, L_{12}, \cdots, L_{KK}$ are linear operations on $\{\tau^V\}$ to obtain $\{\alpha\}$.

Now, combine Eqs. (16) and (19) gives

$$\begin{bmatrix} E_{11} & \cdots & E_{1K} \\ \vdots & \ddots & \vdots \\ E_{K1} & \cdots & E_{KK} \end{bmatrix}^{-1} \begin{Bmatrix} \overset{*}{\alpha}_1 \\ \vdots \\ \overset{*}{\alpha}_K \end{Bmatrix} + V_\infty \begin{bmatrix} L_{11} & \cdots & L_{1K} \\ \vdots & \ddots & \vdots \\ L_{K1} & \cdots & L_{KK} \end{bmatrix}^{-1} \begin{Bmatrix} \alpha_1 \\ \vdots \\ \alpha_K \end{Bmatrix} = \begin{Bmatrix} \frac{\tau_1}{2} \\ \vdots \\ \frac{\tau_K}{2} \end{Bmatrix} \tag{20}$$

The inflow equation shown in Eq. (20) is valid for perturbations about the free-stream velocity, V_∞. A nonlinear version of Eq. (20) can be obtained by replacing V_∞ with a mass flow parameter, $[V_m]$ and using <u>total</u> values of $\{\alpha\}$ and $\{\tau\}$ as suggested in Ref. [35]. Finally, the Pressure Potential Superposition Inflow Model (PPSIM) is presented as

$$\begin{bmatrix} M_{11} & \cdots & M_{1K} \\ \vdots & \ddots & \vdots \\ M_{K1} & \cdots & M_{KK} \end{bmatrix} \begin{Bmatrix} \overset{*}{\alpha}_1 \\ \vdots \\ \overset{*}{\alpha}_K \end{Bmatrix} + [V_m] \begin{bmatrix} L_{11} & \cdots & L_{1K} \\ \vdots & \ddots & \vdots \\ L_{K1} & \cdots & L_{KK} \end{bmatrix}^{-1} \begin{Bmatrix} \alpha_1 \\ \vdots \\ \alpha_K \end{Bmatrix} = \begin{Bmatrix} \frac{\tau_1}{2} \\ \vdots \\ \frac{\tau_K}{2} \end{Bmatrix} \tag{21}$$

where

$$\begin{bmatrix} M_{11} & \cdots & M_{1K} \\ \vdots & \ddots & \vdots \\ M_{K1} & \cdots & M_{KK} \end{bmatrix} := \begin{bmatrix} E_{11} & \cdots & E_{1K} \\ \vdots & \ddots & \vdots \\ E_{K1} & \cdots & E_{KK} \end{bmatrix}^{-1}$$

In Eq. (21), diagonal blocks in the matrices relate self-induced inflow states to the rotor's pressure coefficients, similar to those used in the Peters-He inflow model. The effect of other rotors' pressure loading on the rotor inflow states is accounted for by the off-diagonal blocks, capturing the complex aerodynamic interference effects among the rotors in a multi-rotor system. The equations to compute each element in the M- and L-matrices are given in Appendix C. In addition, $[V_m]$ is a diagonal matrix consisting of each rotor's mass flow parameter, i.e. $\text{diag}([V_{m1}], ..., [V_{mK}])$.

2.4 Coaxial rotor PPSIM

In a coaxial rotor system, the upper rotor is denoted as rotor '1' and lower rotor as rotor '2'. As such, the inflow equation for coaxial rotor PPSIM [29] is simplified from Eq. (21) and written as shown in Eq. (22). Again, equations to compute elements in

M- and L-matrices in Eq. (22) are included in Appendix D.

$$\begin{bmatrix} M_{11} & M_{12} \\ M_{21} & M_{22} \end{bmatrix} \begin{Bmatrix} \overset{*}{\alpha}_1 \\ \overset{*}{\alpha}_2 \end{Bmatrix} + \begin{bmatrix} V_{m1} & 0 \\ 0 & V_{m2} \end{bmatrix} \begin{bmatrix} L_{11} & L_{12} \\ L_{21} & L_{22} \end{bmatrix}^{-1} \begin{Bmatrix} \alpha_1 \\ \alpha_2 \end{Bmatrix} = \begin{Bmatrix} \tau_1/2 \\ \tau_2/2 \end{Bmatrix} \tag{22}$$

where

$$V_m := \mathrm{diag}(V_T, V, \ldots V) \tag{23}$$

$$V = \frac{\mu^2 + (\lambda_m + \lambda)\lambda}{V_T} \tag{24}$$

$$V_T = \sqrt{\mu^2 + \lambda^2} \tag{25}$$

$$\lambda = \lambda_m + \lambda_f \tag{26}$$

2.5 Limitations of coaxial rotor PPSIM

While the theoretical formulations for both Peters-He inflow model and PPSIM are similar, there are some drawbacks in the latter model due to its application in coaxial rotor (or multi-rotor) systems. In particular, the limitations are,

1. The assumption of rigid, cylindrical wake geometries in a coaxial rotor system is no longer valid in forward flight. This is because strong mutual aerodynamic interference between the upper and lower rotors distorted the wake geometries, especially at low advance ratios [50].

2. Time delay effects associated with propagation of upper rotor inflow perturbations onto the lower rotor are not captured in PPSIM. It is assumed that upper rotor pressure load changes have an instantaneous effect on lower rotor inflows. Only time lag are modeled in the M-matrix.

Note that there are no closed-form solutions for off-diagonal blocks in PPSIM M- and L-matrices. They are precomputed numerically before use in real-time simulations. In addition, elements in L-matrix are stored in a lookup table indexed by wake skew function, X_{skew}. Each set of precalculated M- and L-matrices table is only applicable

to one coaxial rotor configuration, specifically the separation distance between upper and lower rotors. Wake contraction effects can be taken into account by correcting the streamline coordinates when computing the L-matrix numerically.

CHAPTER III

EVALUATION OF COAXIAL ROTOR PPSIM STEADY INFLOWS

Due to lack of experimental data on coaxial rotor induced inflow distributions in open literature, the study will make use of vorticity-based method models in generating results for comparison against the analytical coaxial rotor inflow model. One model used is GT-Hybrid, a free-wake model developed in Georgia Tech [27] which has shown to have good correlations in terms of thrust and torque coefficients with the Harrington coaxial rotor wind tunnel data [14]. Next is the FLIGHTLAB Viscous Vortex Particle Method (VVPM), a commercial software developed by Advanced Rotorcraft Techonology (ART). Similarly, results from VVPM show good agreement with the Haringoton coaxial rotor experimental data as well [50, 9]. As such, induced inflow distribution results from these two models will provide a good benchmark for evaluating the coaxial rotor PPSIM inflow predictions [17].

3.1 GT-Hybrid free-wake model

GT-Hybrid uses the Navier-Stokes solver for viscous flow over the blade and full potential solver for far away regions. It uses the Reynolds Averaged Navier-Stokes methodology for viscous flow over the blade in near field defined by the blade grid. Influences of other blades and trailing vorticities in the far field wake are accounted for by modeling them as a collection of piece-wise linear bound and trailing tip vortex elements, respectively. This hybrid Navier-Stokes/wake modeling approach reduces computation time because the flow field is only resolved in the blade grid rather than the entire flow field containing the rotor system, as is typically done in wake-capturing

software.

The three-dimensional unsteady Navier-Stokes equations are solved in the transformed body-fitted coordinate system using a time-accurate, finite volume scheme. A third order spatially accurate Roe scheme is used for computing the inviscid fluxes. The Navier-Stokes equations are integrated in time by means of an approximate LU-implicit time marching scheme which is first order in temporal accuracy. Viscous non-slip boundary condition is imposed at the solid surface. The vortex model is based on a Lagrangian wake approach where a collection of vortex elements are shed from the rotor blade trailing edge and are convected downstream by a combination of free-stream and self-induced velocities. The vortex filaments are allowed to move freely in space and interact with each other, inherently capturing any wake distortion effects in the flow field.

In addition to specifying flight conditions in GT-Hybrid, individual blade pitch angles at each azimuth step must be predefined for one rotor revolution in an input file before simulation. These pitch angles are held constant during the simulation run. GT-Hybrid main output variables include the blades' pressure loading, thrust coefficients, wake geometry as well as wake circulation strength along the filaments. By using the Biot-Savart law, induced velocities at the rotor plane are computed from the wake information. Subsequently, the rotors' pressure and induced inflow distributions are obtained after post-processing GT-Hybrid output file.

3.2 Viscous Vortex Particle Method (VVPM)

VVPM solves for the vorticity field directly from the vorticity-velocity form of incompressible Navier-Stokes equations using a Lagrangian formulation. It involves solving the governing equations in a convection-diffusion process which applies to regions with vorticities only. In addition, it does not require any grid generation effort. VVPM captures the fundamental vorticity dominated flow physics for both vorticity

stretching and diffusion due to airflow viscosity effect.

The VVPM rotor wake model is coupled with a lifting line based blade element model for vorticity source generation, which is directly related to blade bound circulation from the Kutta-Joukowski Theorem. This allows the prescription of desired airloads distribution across the rotor disk, without the need for airfoil properties such as lift and drag coefficients. As such, this model can be used to simulate induced inflows of any generic rotor blade designs. Furthermore, VVPM is fully parallelized using both OpenMP on multi-core CPUs and CUDA on compatible GPUs, rendering it an extremely efficient higher fidelity solution for vorticity dominated flow analysis.

The main inputs to VVPM consist of flight conditions and prescribed pressure loading distributions on the rotor disk. In addition, pressure loading can be varied during run time which is very useful when analysing transient responses. Minimal post-processing effort is required since VVPM logged the rotors' pressure loading and induced velocities in its output file.

3.3 Comparison methodology

Since the finite state coaxial rotor PPSIM is formulated based on perturbation theory, it is instructive to compare perturbed induced inflows between the analytical model and GT-Hybrid/VVPM. While the most direct method for comparison of inflow distributions between different models is through contour plots of downwash variation across the rotor disks, this approach provides very little quantitative information about inflow differences. A more appropriate method is to compare the inflow states computed using PPSIM and those extracted from GT-Hybrid and VVPM results. For flight dynamics analysis, three fundamental inflow states; consisting of uniform (α_1^{0c}), fore-to-aft variation (α_2^{1c}) and side-to-side variation (α_2^{1s}) are extracted from GT-Hybrid and VVPM induced inflow distribution results using Eqs. (27) through (29) [9]. In the equations, $\bar{r}$ and $\bar{\psi}$ are the radial and azimuthal position of each

sample flow point, respectively. The sampled downwash, $\bar{w}$ is non-dimensional with respect to the rotor tip speed. Lastly, $\bar{P}$ is normalised Legendre function of the first kind which depends on radial station only. Similarly, three inflow states are also used in the coaxial rotor PPSIM.

$$\alpha_1^{0c} = \frac{1}{2\pi}\int_0^{2\pi}\int_0^1 \bar{r}\bar{P}_1^0(\bar{r})\bar{w}(\bar{r},\bar{\psi})d\bar{r}d\bar{\psi} \tag{27}$$

$$\alpha_2^{1c} = \frac{1}{\pi}\int_0^{2\pi}\int_0^1 \bar{r}\bar{P}_2^1(\bar{r})\bar{w}(\bar{r},\bar{\psi})\cos(\bar{\psi})d\bar{r}d\bar{\psi} \tag{28}$$

$$\alpha_2^{1s} = \frac{1}{\pi}\int_0^{2\pi}\int_0^1 \bar{r}\bar{P}_2^1(\bar{r})\bar{w}(\bar{r},\bar{\psi})\sin(\bar{\psi})d\bar{r}d\bar{\psi} \tag{29}$$

Next, pressure loading on both upper and lower rotors must be identical for all three models. This ensures that any differences observed in the extracted inflow states are due to different modeling approach used in each model. Pressure coefficients, τ_1^{0c}, τ_2^{1c} and τ_2^{1s} are extracted from the blade sectional circulation lift, $\mathrm{L_q}$ using Eqs. (11) through (13) with shaping functions given in Eqs. (30) and (31). Hence, these pressure coefficients are used to make sure that PPSIM and VVPM are subjected to the same rotor pressure loading as GT-Hybrid.

$$\Psi_1^0(\bar{r}) = \frac{\bar{P}_1^0(\bar{r})}{\nu} \tag{30}$$

$$\Psi_2^1(\bar{r}) = \frac{\bar{P}_2^1(\bar{r})}{\nu} \tag{31}$$

$$\nu = \sqrt{1-\bar{r}^2}$$

As shown in Ref. [39], post-multiplying inverse of L-matrix ($[L]^{-1}$) by the mass flow parameters ($[V_m]$) gives better correlation with experimental data and the vortex lattice method. As such, Eq. (22) is rewritten as shown in Eq. (32) where $[V_m]'s$ are on the right side of $[L]^{-1}$. This version of the coaxial rotor PPSIM inflow equation is used in this thesis.

$$\begin{bmatrix} M_{11} & M_{12} \\ M_{21} & M_{22} \end{bmatrix} \begin{Bmatrix} \overset{*}{\alpha}_1 \\ \overset{*}{\alpha}_2 \end{Bmatrix} + \begin{bmatrix} L_{11} & L_{12} \\ L_{21} & L_{22} \end{bmatrix}^{-1} \begin{bmatrix} V_{m1} & 0 \\ 0 & V_{m2} \end{bmatrix} \begin{Bmatrix} \alpha_1 \\ \alpha_2 \end{Bmatrix} = \begin{Bmatrix} \tau_1/2 \\ \tau_2/2 \end{Bmatrix} \tag{32}$$

Mass flow parameters are not known explicitly from GT-Hybrid or VVPM output data and is calculated by time-marching Eq. (32). Time histories of pressure coefficients are extracted from VVPM blade loading results. Induced inflow, λ_m for each rotor is computed by using the relationship $\lambda_m = \sqrt{3}\alpha_1^{0c}$ given in Ref. [35] with the respective rotor's uniform inflow state. Based on momentum theory, both upper and lower rotors' wake skew angles are computed using Eq. (33). These values of wake skew angles are used to look-up precomputed L-matrix table. Finally, time histories of both rotors' mass flow parameters, momentum wake skew angles and inflow states are obtained by solving Eq. (32) through time-marching.

$$\chi_{\text{mom}} = \tan^{-1}\left(\frac{\mu}{\lambda_f + \lambda_m}\right) \tag{33}$$

3.4 Description of procedures

The procedures used to carry out the simulations is summarized below.

1. Predetermined blade pitch angles for both upper and lower rotors are input to GT-Hybrid and allow simulation to run for fixed number of revolutions. This is to ensure the solutions reach steady-state condition and pressure coefficients are extracted from GT-Hybrid rotor blade loading.

2. Same pressure coefficients are used in VVPM and coaxial rotor PPSIM simulations. Steady-state induced inflow distributions over rotor planes are sampled in VVPM.

3. Small perturbation to rotor pitch angle is injected to GT-Hybrid model and run the simulation to steady-state. The percentage change in pressure coefficients are computed.

4. Same pressure coefficient variations from step 3 are used in VVPM and coaxial rotor PPSIM simulations and steady-state induced inflow results are logged.

5. Extract inflow states (before and after perturbations) from induced inflow distributions results predicted by GT-Hybrid and VVPM.

6. Compute the percentage change in inflow states for each model.

3.5 Scope of work and simulation setup

For this study, comparison of inflow states among the three models is carried out for hover and advance ratios from 0.07 to 0.20, which covers the typical flight envelope of a vertical lift aircraft. In addition, only perturbation to the upper rotor collective pitch angle in GT-Hybrid is conducted. This is to study effects of upper rotor wake interference on the lower rotor induced velocities; which possibly have significant effects on its performance. Furthermore, lower rotor loading perturbations have minimal impact on upper rotor induced inflows with increasing advance ratios since its wake is swept downstream, far away from the upper rotor. A positive pitch angle perturbation of 1 degree is used.

Geometric properties from the Harrington coaxial rotor, Rotor 1 [7] are used to create isolated coaxial rotor models in GT-Hybrid and VVPM. The rotor radius is 12.5 ft and upper rotor is offset from the lower rotor by 2.38 ft (19 percent of rotor radius). The rotational speed of upper and lower rotors is 37.5 rad/s. In GT-Hybrid, a series of NACA four-digit airfoil is used to model the blade's planform in order to match the thickness ratio profile given in Ref. [7]. Other modeling parameters such as vortex core size (for GT-Hybrid) and particle resolutions (for VVPM) are kept the same as those used in Refs. [14] and [9], respectively.

In GT-Hybrid and VVPM, steady-state condition is achieved when changes to the rotors' thrust coefficients between revolutions are less than a specified tolerance which is chosen to be in the order of 10^{-6}. For coaxial rotor PPSIM, the computed inflow states are used to check if sufficient simulation time is given for reaching steady-state conditions.

3.6 Comparison of steady-state inflow states change

For ease of comparison between models, perturbations in inflow states are expressed in terms of percentage change from the respective model's steady-state values before step input.

$$\Delta\% = \frac{a-b}{|b|} \times 100\% \tag{34}$$

where

a = steady-state values after step input

b = steady-state values before step input

In Eq. (34), the steady-state values are averaged over ten rotor revolutions. To avoid values of $\Delta\%$ from blowing up due to division by a small number, it is intentionally set to zero if $|b|$ is less than some threshold. For example, if the side-to-side inflow state is one order of magnitude less than the uniform or fore-to-aft inflow states, value of $\Delta\%$ corresponding to side-to-side inflow state is set to zero. This prevents the percentage change in side-to-side inflow state from overshadowing other inflow component results.

Table. 1 shows the change in upper and lower rotor pressure coefficients in hover, corresponding to one degree step input to upper rotor collective pitch angle in GT-hybrid coaxial rotor model. Due to aerodynamic interactions between the two rotors, lower rotor uniform pressure coefficient is reduced by about 2.5% while a 12.5% increase in upper rotor uniform pressure coefficient is observed. All three models are subjected to the same pressure coefficients perturbations.

The corresponding change in inflow states due to pressure coefficient perturbations is shown in Table. 2. Results from coaxial rotor PPSIM, GT-Hybrid and VVPM are shown. Since the isolated coaxial rotor is operating in hover flight condition, only the uniform inflow states are affected. Prediction from PPSIM shows a change of 3.5% in upper rotor uniform inflow state which is comparable with both GT-Hybrid (3.6%)

Table 1: Pressure coefficient perturbations equivalent to 1 degree upper rotor collective change in GT-Hybrid isolated coaxial rotor model

	Upper rotor[1]			Lower rotor		
Adv. ratio	τ_1^{0c}	τ_2^{1c}	τ_2^{1s}	τ_1^{0c}	τ_2^{1c}	τ_2^{1s}
Hover	12.5233	0.0000	0.0000	-2.5934	0.0000	0.0000
0.07	11.3292	-0.9743	-11.8439	-1.5561	-2.0699	-0.5355
0.12	10.3317	-0.7032	-9.8060	-1.2396	-4.7735	0.2495
0.16	9.9335	0.1967	-8.7656	-0.6437	-4.2580	-0.0984
0.20	9.3225	3.8993	-7.6916	-0.6280	-5.2043	-0.2077

[1]Values are expressed in $\Delta\%$, using Eq. (34)

and VVPM (4.6%). Good agreement in lower rotor inflow states between PPSIM and GT-Hybrid/VVPM are also observed.

In forward flight, collective pitch angle perturbation to upper rotor will generate uniform, fore-to-aft and side-to-side gradient pressure coefficients change on both rotors. This is clearly seen in Table. 1 where all three pressure coefficient components in upper and lower rotors are perturbed at advance ratio of 0.07. From the table, uniform pressure coefficient increased by 11%, a slight reduction in fore-to-aft component of 1% and drop in side-to-side of 12%. Reduction in pressure coefficients at the lower rotor is less than 3%. The change in upper rotor inflow states at advance ratio of 0.07 is found in Table. 2. For uniform inflow states, GT-Hybrid, PPSIM and VVPM results are close to each other with a maximum difference of about 0.5% between VVPM and PPSIM. PPSIM under estimated fore-to-aft inflow state compared to both GT-Hybrid and VVPM, with a maximum difference of 1.5% between PPSIM and VVPM. Similarly, the lower rotor uniform states for all 3 models are close to each other. But there are considerable differences in terms of fore-to-aft gradient inflow states between PPSIM and VVPM. In fact, differences between GT-Hybrid and VVPM are also observed in the fore-to-aft inflow states for both upper and lower rotors. This is because GT-Hybrid and VVPM use different approaches in modeling rotor wakes, affecting the level of wake distortions at low advance ratios. In VVPM,

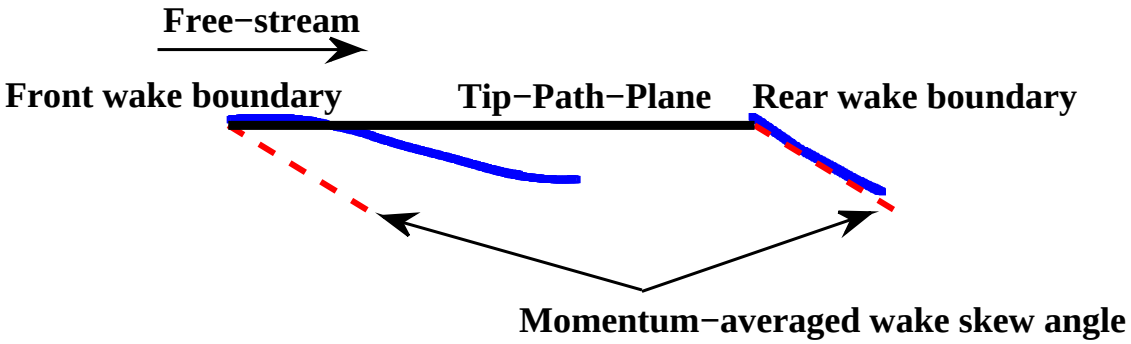

(a) Upper rotor (Side view)

(b) Lower rotor (Side view)

Figure 1: Distorted geometries (solid line) of coaxial rotor wakes in forward flight from GT-Hybrid at advance ratio of 0.07

viscosity effects are taken into account when solving the Navier-Stokes equations in vorticity-velocity form to obtain each particle's vorticity strength. On the other hand, in free wake models, the wakes are based on potential flow theory with empirical parameters such as vortex core growth, wake dissipation, etc to account for viscous effects. Finally, change in side-to-side inflow states are small and are dropped.

A comparison of the rotor wake geometries between momentum theory and those extracted from GT-Hybrid at advance ratio of 0.07 is shown in Fig. 1. The front and rear wake boundaries predicted by GT-Hybrid are different compared to momentum theory for both upper and lower rotors as shown in Figs. 1(a) and Figs. 1(b), respectively. In GT-Hybrid (or other vorticity-based method models), wake geometries are allowed to convect freely in space based on induced velocities from the rotors and free-stream; changing the shape of the wake boundaries. But in PPSIM, the wakes are assumed to be rigid with skewed angles computed from momentum theory as shown in Fig. 2.

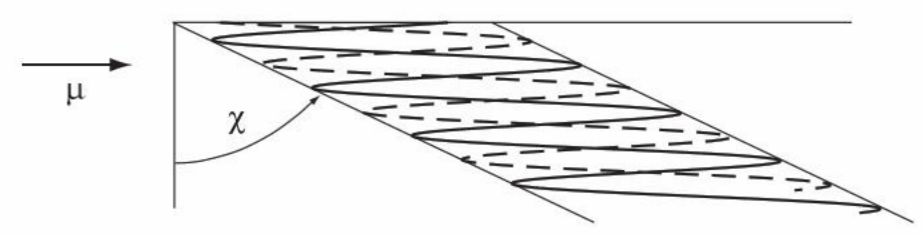

(a) Side view

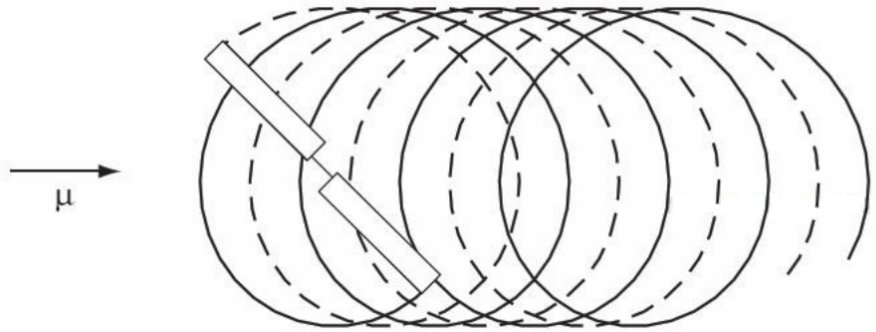

(b) Top view

Figure 2: Tip vortex geometry of rotor wake in forward flight without wake distortion effects [42]

Next, change in pressure coefficients and inflow states at advance ratio of 0.12 are also presented in Table. 1 and Table. 2, respectively. The three models have similar uniform inflow states perturbations. Here PPSIM also under-estimates the fore-to-aft inflow states, but the differences are less compared to the advance ratio of 0.07 case. This is because at higher advance ratios, free-stream inflows are significantly larger than induced velocities and this caused the wake geometries to resemble that of a rigid, skewed cylindrical wake (which is assumed in PPSIM). Hence, it is expected that inflow state results from PPSIM will have a better correlation with GT-Hybrid/VVPM predictions at higher advance ratios. At the lower rotor, PPSIM fore-to-aft inflow states are smaller compared to both GT-Hybrid and VVPM.

Wake geometries from both rotors at advance ratio of 0.16 extracted from GT-Hybrid model are shown in Fig. 3. The momentum-averaged skewed wakes (dotted line) are also superimposed onto the same figure for comparison. Here, it is clear

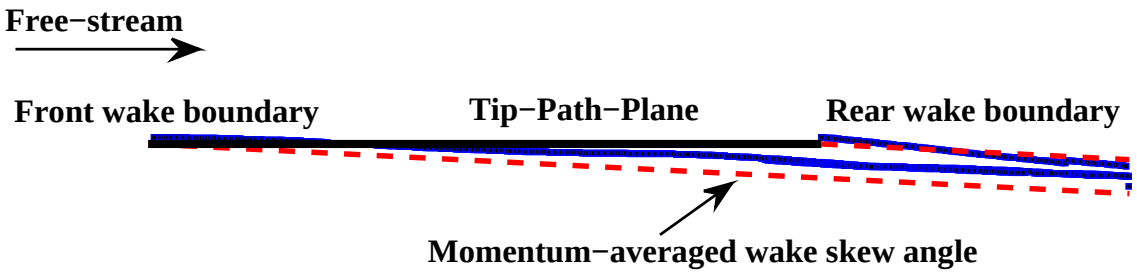

(a) Upper rotor (Side view)

(b) Lower rotor (Side view)

Figure 3: Geometries (solid line) of coaxial rotor wakes in forward flight from GT-Hybrid at advance ratio of 0.16

that the front and rear wake boundaries corresponding to GT-Hybrid are very close to momentum theory. This observation supports the fact that inflows at higher advance ratios are dominated by free-stream component which reduces wake distortions caused by rotor-to-rotor interference induced velocities. Finally, perturbed inflow state results for advance ratios of 0.16 and 0.20 are also found in Table. 2. Inflow predictions by PPSIM are comparable to both GT-Hybrid and VVPM results at these high advance ratios. Just like previous flight conditions, change in side-to-side inflow components are relatively small compared to uniform and fore-to-aft inflow states and are dropped.

From the comparisons, it can be concluded that real flow effects must be included in coaxial rotor PPSIM to improve its inflow state correlations with GT-Hybrid/VVPM (or other higher fidelity models) data. This includes air viscosity, wake contractions/distortions as well as wake roll-up influences on rotor induced inflows. The next chapter will describe how these effects are incorporated into coaxial rotor PPSIM inflow equation, in particular the L-matrix.

Table 2: Comparison of inflow state changes between PPSIM, GT-Hybrid and VVPM due to pressure coefficient perturbations listed in Table.1

		Upper rotor[1]			Lower rotor		
Adv. ratio	Models	α_1^{0c}	α_2^{1c}	α_2^{1s}	α_1^{0c}	α_2^{1c}	α_2^{1s}
	PPSIM	3.4113	0.0000	0.0000	3.2548	0.0000	0.0000
Hover	GT-Hybrid	3.6402	0.0000	0.0000	3.5035	0.0000	0.0000
	VVPM	4.5920	0.0000	0.0000	3.4046	0.0000	0.0000
	PPSIM	4.1951	2.4080	0.0000	3.6846	1.7610	0.0000
0.07	GT-Hybrid	3.9625	2.7374	0.0000	3.7998	1.5948	0.0000
	VVPM	4.6303	4.0089	0.0000	3.8184	4.0709	0.0000
	PPSIM	4.6756	3.5631	0.0000	4.2472	3.2706	0.0000
0.12	GT-Hybrid	4.6589	4.7483	0.0000	4.8445	5.0210	0.0000
	VVPM	5.1886	5.0543	0.0000	4.0899	4.3475	0.0000
	PPSIM	4.8966	4.5585	0.0000	4.3051	4.8223	0.0000
0.16	GT-Hybrid	3.7037	5.1823	0.0000	4.0104	4.9212	0.0000
	VVPM	5.2378	5.3031	0.0000	4.0275	4.3716	0.0000
	PPSIM	4.6166	4.8279	0.0000	3.5166	4.2418	0.0000
0.20	GT-Hybrid	3.7244	4.7458	0.0000	4.2860	4.8251	0.0000
	VVPM	4.8394	5.2712	0.0000	3.4630	4.0935	0.0000

[1]Values are expressed in $\Delta\%$, using Eq. (34)

CHAPTER IV

CORRECTIONS TO PPSIM L-MATRIX FOR STEADY-STATE INDUCED INFLOWS

Due to upper and lower rotor wake interactions, induced inflows at the respective rotor planes are more complicated compared to a single rotor case. In particular during hover and low advance ratios, induced velocities from the upper rotor affects both its own as well as the lower rotor's wake structure. On a similar token, the lower rotor also changes upper rotor's wake geometry which have an impact on the upper rotor self-induced inflows. Furthermore, wake vortices from both rotors may coalesce, inducing strong inflows on upper and lower rotors. These phenomena are not taken into account in PPSIM formulation, which is based on potential flow theory. Since the finite state coaxial rotor inflow model is formulated as a first order ordinary differential equation, corrections due to wake contractions/distortions and other real flow effects are applied to the influence coefficient matrix (L-matrix). The apparent mass matrix or M-matrix only affect the dynamics part of the inflow equation. A system identification approach is used to capture L-matrix correction terms using higher fidelity model inflow data which is done in a two-step process [16]. First, L-matrix is extracted from the model inflow results using the least-square-fit method. After which, each element in the extracted L-matrix is compared against the original coaxial rotor PPSIM formulation to compute the differences.

4.1 Extraction of L-matrix from VVPM data

The VVPM is used to generate rotor induced inflow data for L-matrix identification. The advantage of using VVPM is the freedom to prescribe any pressure loading

distributions on the rotor disk. In Eqs. (35) and (36), the blade lift distribution, $L_q(\bar{r}, \bar{\psi}_q)$ is calculated from desired pressure coefficients, τ_n^{mc} and τ_n^{ms}. Using Kutta-Joukowski Theorem, the blade bound circulation is known and used to compute the source vorticity in VVPM. By adopting this approach, change in induced inflows on upper and lower rotors can be directly related to one specific pressure coefficient perturbation.

$$L_{qn}^{mc}(\bar{r}, \bar{\psi}_q) = \frac{2\pi}{Q}\rho\Omega^2 R^3 \tau_n^{mc} \bar{r}\sqrt{1-\bar{r}^2}\Psi_n^m \cos(m\bar{\psi}_q) \tag{35}$$

$$L_{qn}^{ms}(\bar{r}, \bar{\psi}_q) = \frac{2\pi}{Q}\rho\Omega^2 R^3 \tau_n^{ms} \bar{r}\sqrt{1-\bar{r}^2}\Psi_n^m \sin(m\bar{\psi}_q) \tag{36}$$

Studies conducted by Kong et al. [18, 19] showed that corrections to L-matrix for wake distortion effects are less sensitive to different flight conditions by using perturbed quantities. This means that perturbed values of pressure coefficients and corresponding change in inflow states are used to compute the L-matrix, shown in Eq. (37). In the equation, $[L_{11}]_{\text{VVPM}}$, $[L_{12}]_{\text{VVPM}}$, $[L_{21}]_{\text{VVPM}}$ and $[L_{22}]_{\text{VVPM}}$ are L-matrix blocks extracted from VVPM data. Variables $\{\Delta\tau_1\}$ and $\{\Delta\tau_2\}$ correspond to upper and lower rotor pressure coefficient perturbations, respectively. $\{\Delta\alpha_{11}\}$ and $\{\Delta\alpha_{21}\}$ are the change in steady-state inflow states on upper and lower rotors, respectively due to step input on the upper rotor's pressure coefficient. Similarly, $\{\Delta\alpha_{12}\}$ and $\{\Delta\alpha_{22}\}$ are the change in upper and lower rotors steady-state inflow states, respectively because of lower rotor's pressure coefficient perturbation. Note that the inflow states and pressure coefficients column vectors are defined as shown in Eqs. (38) and (39), respectively.

$$\begin{aligned}
[L_{11}]_{\text{VVPM}} &= 2V_1\{\Delta\alpha_{11}\}\{\Delta\tau_1\}^+ \\
[L_{12}]_{\text{VVPM}} &= 2V_2\{\Delta\alpha_{12}\}\{\Delta\tau_2\}^+ \\
[L_{21}]_{\text{VVPM}} &= 2V_1\{\Delta\alpha_{21}\}\{\Delta\tau_1\}^+ \\
[L_{22}]_{\text{VVPM}} &= 2V_2\{\Delta\alpha_{22}\}\{\Delta\tau_2\}^+
\end{aligned} \tag{37}$$

where

$$\{\Delta\tau_1\}^+ = [\{\Delta\tau_1\}^T\{\Delta\tau_1\}]^{-1}\{\Delta\tau_1\}^T$$
$$\{\Delta\tau_2\}^+ = [\{\Delta\tau_2\}^T\{\Delta\tau_2\}]^{-1}\{\Delta\tau_2\}^T$$

$$\{\alpha\} := \begin{Bmatrix} \alpha_1^{0c} \\ \alpha_2^{1c} \\ \alpha_2^{1s} \end{Bmatrix} \tag{38}$$

$$\{\tau\} := \begin{Bmatrix} \tau_1^{0c} \\ \tau_2^{1c} \\ \tau_2^{1s} \end{Bmatrix} \tag{39}$$

As seen from Eq. (37), each column in the L-matrix is calculated by perturbing one pressure coefficient component at a time. In other words, by perturbing all six pressure coefficients separately (three each for upper and lower rotors), the L-matrix is computed analytically. There is no need to predetermine the L-matrix structure, i.e. assuming there are no cosine and sine couplings. As such, it is important that only one pressure coefficient is excited during the system identification process and VVPM provides the means to do so. Note that steady-state values of $V's$ before perturbation are used in Eq. (37) since the perturbation approach is linearized about this flight condition. Furthermore in real-time flight simulation applications, only $V's$ at previous time step is known as the inflow states are obtained by forward time-marching. As advance ratios increase, change in induced velocities due to perturbations will be much smaller compared to free-stream component which dominate the mass flow parameters.

The FLIGHTLAB coaxial rotor model used earlier to correlate inflow results with GT-Hybrid and coaxial rotor PPSIM is used for system identification purposes. At

each time step, induced inflows are sampled at 30 radial and 48 azimuthal locations at each rotor plane. Both rotor induced inflows data are generated using VVPM by adopting the procedures summarized below.

1. Load a coaxial rotor model into FLIGHTLAB scope environment.
2. Define flight advance ratio and prescribed pressure coefficients on upper/lower rotors.
3. Run the FLIGHTLAB-VVPM coaxial rotor model until it achieves steady-state condition.
4. Specify the pressure coefficient component to perturb and amount of step change.
5. Time march the model to remove transients due to the step input.
6. Save time histories of variables such as blade loading and induced velocities at pre-defined flow sampling points into an output file.

4.2 Computation of L-matrix corrections, ΔL

At each advance ratio and initial upper/lower rotors prescribed pressure coefficients, L-matrix blocks are extracted from VVPM data and compared against the original coaxial rotor PPSIM formulation. The differences or delta L-matrix capture real flow effects such as wake contractions/distortions, viscosity and flow swirls, not modeled in potential flow. Corrections to each L-matrix block are computed as follows

$$
\begin{aligned}
[\Delta L_{11}] &= [L_{11}]_{\text{VVPM}} - [L_{11}] \\
[\Delta L_{12}] &= [L_{12}]_{\text{VVPM}} - [L_{12}] \\
[\Delta L_{21}] &= [L_{21}]_{\text{VVPM}} - [L_{21}] \\
[\Delta L_{22}] &= [L_{22}]_{\text{VVPM}} - [L_{22}]
\end{aligned}
\tag{40}
$$

where $[L_{11}]$, $[L_{12}]$, $[L_{21}]$ and $[L_{22}]$ are original coaxial rotor PPSIM L-matrices. Now gather the delta L-matrices to form a L-matrix corrected PPSIM inflow equation as shown

$$\begin{bmatrix} M_{11} & M_{12} \\ M_{21} & M_{22} \end{bmatrix} \begin{Bmatrix} \overset{*}{\alpha}_1 \\ \overset{*}{\alpha}_2 \end{Bmatrix} + \begin{bmatrix} L_{11}+\Delta L_{11} & L_{12}+\Delta L_{12} \\ L_{21}+\Delta L_{21} & L_{22}+\Delta L_{22} \end{bmatrix}^{-1} \begin{bmatrix} V_{m1} & 0 \\ 0 & V_{m2} \end{bmatrix} \begin{Bmatrix} \alpha_1 \\ \alpha_2 \end{Bmatrix} = \begin{Bmatrix} \tau_1/2 \\ \tau_2/2 \end{Bmatrix} \tag{41}$$

4.2.1 Single rotor validation

The method of extracting a L-matrix from VVPM data is applied on a single rotor case for validation against the Peters-He model. One rotor was removed from the Harrington coaxial rotor FLIGHTLAB model to simulate a single rotor test case. Only one pressure coefficient; uniform, fore-to-aft or side-to-side gradient component is perturbed during each VVPM simulation run. Based on the least-square-fit method, change in rotor pressure coefficient and inflow states extracted from VVPM data (together with mass flow parameters computed using momentum theory) are used to compute each column in the L-matrix. For example, first column of the L-matrix is calculated if only uniform pressure coefficient is perturbed. Similarly, the second column is analytically computed if a step change is injected to the fore-to-aft gradient pressure coefficient only.

In this test case, the initial prescribed uniform pressure coefficient is set to be 0.003 ($C_T = 0.0035$) while the other two components are set to zero. For each pressure coefficient component perturbation, a step change of 0.0003 (10% of uniform pressure coefficient) was used. The L-matrix extracted from VVPM data at hover flight condition is shown in Eq. (42). Most of the off-diagonal terms are zeros, except the coupling terms between cosine and sine parts. This is due to effect of flow swirls where influence of cosine (sine) part of pressure loading affect the sine (cosine) inflow states. In potential flow theory, swirls are neglected resulting in these cosine-sine coupling terms to be zero. For comparison against Peters-He L-matrix, the elements are

summarized in Table. 3. Note that only non-zero elements in the L-matrix extracted from VVPM data are shown. The diagonal terms. $L(1,1)$, $L(2,2)$ and $L(3,3)$ extracted from VVPM data are very close to Peters-He inflow model with less than 5% difference. This is likely due to errors introduced while extracting inflow states from VVPM induced inflow distribution data using numerical double integration methods.

$$[L]_{\text{VVPM,hover}} = \begin{bmatrix} 0.7757 & 0.0000 & 0.0000 \\ 0.0000 & 0.6545 & -0.1772 \\ 0.0000 & 0.1826 & 0.6519 \end{bmatrix} \tag{42}$$

Similarly, Table. 3 also compares the L-matrix extracted from VVPM against Peters-He inflow model at advance ratio of 0.04. Some elements such as $L(1,1)$, $L(2,1)$ and $L(2,2)$, showed lower magnitude compared to those in Peters-He L-matrix. This indicates that uniform and fore-to-aft gradient pressure loading (thrust and pitching moments) have smaller effects on rotor downwash in real flows compared to potential theory. The main reason is because of higher up-wash effects near the fore disk and blade tip regions predicted by VVPM in forward flight. Another possible reason for this difference could be due to diffusion caused by air viscosity (since wake has traveled downstream at advance ratio of 0.04), which is neglected in potential flow. Interestingly, coupling effects between sine and cosine parts, i.e. $L(2,3)$ and $L(3,2)$ have weakened compared to hover case. Lastly, $L(3,3)$ extracted from VVPM inflow data is larger than Peters-He values, which is likely due to wake roll-ups generated at the advancing and retreating sides during forward flight.

L-matrix elements extracted from VVPM data showed good match with the Peters-He inflow model to a large extent. This means that the procedures used to carry out the VVPM simulation and extraction of L-matrix from the data is done correctly. With the same approach, L-matrix blocks, i.e. $[L_{11}]$, $[L_{12}]$, $[L_{21}]$ and $[L_{22}]$ are extracted from VVPM coaxial rotor simulation data as shown in the next section.

Table 3: Comparison of single rotor L-matrix elements

Hover		
Elements[1]	Extracted from VVPM[2]	Peters-He
$L(1,1)$	0.7757	0.7500
$L(2,2)$	0.6545	0.6250
$L(2,3)$	-0.1772	0.0000
$L(3,2)$	0.1826	0.0000
$L(3,3)$	0.6519	0.6250
Adv. ratio = 0.04		
Elements	Extracted from VVPM	Peters-He
$L(1,1)$	0.7272	0.7500
$L(1,2)$	-0.2516	-0.2261
$L(2,1)$	0.2412	0.4522
$L(2,2)$	0.4316	0.4955
$L(2,3)$	-0.1329	0.0000
$L(3,2)$	0.1211	0.0000
$L(3,3)$	0.8396	0.7546

[1]First index is row number and second index is column
[2]Only non-zero elements in extracted L-matrix are shown

4.2.2 Coaxial rotor

All 36 elements in the L-matrix blocks are extracted from VVPM induced inflows by perturbing one pressure coefficient on each rotor separately. In other words, by perturbing upper rotor pressure coefficients, elements in $[L_{11}]$ and $[L_{21}]$ are extracted from VVPM results using the least-square-fit method. Similarly, $[L_{12}]$ and $[L_{22}]$ are extracted from change in upper and lower rotor inflow states, respectively due to lower rotor pressure coefficient perturbations. Both upper and lower rotors have initial prescribed pressure coefficient of 0.003 each. A step change of 0.00015 (5% of uniform pressure coefficient) is injected to each pressure coefficient component. Equation (43) shows the extracted L-matrix blocks from VVPM data in hover.

$$[L_{11}]_{\text{VVPM,hover}} = \begin{bmatrix} 0.8615 & 0.0000 & 0.0000 \\ 0.0000 & 0.7164 & 0.1522 \\ 0.0000 & -0.1628 & 0.7114 \end{bmatrix} \tag{43}$$

$$[L_{12}]_{\text{VVPM,hover}} = \begin{bmatrix} 0.4172 & 0.0000 & 0.0000 \\ 0.0000 & 0.1333 & -0.2688 \\ 0.0000 & 0.2521 & 0.1213 \end{bmatrix}$$

$$[L_{21}]_{\text{VVPM,hover}} = \begin{bmatrix} 1.0125 & 0.0000 & 0.0000 \\ 0.0000 & 0.8192 & 0.2284 \\ 0.0000 & -0.2469 & 0.8060 \end{bmatrix}$$

$$[L_{22}]_{\text{VVPM,hover}} = \begin{bmatrix} 0.8851 & 0.0000 & 0.0000 \\ 0.0000 & 0.5463 & -0.6473 \\ 0.0000 & 0.6031 & 0.5146 \end{bmatrix}$$

Comparison of the extracted elements against PPSIM L-matrix in hover is presented in Table. 4. First, extracted elements $L_{11}(1,1)$, $L_{21}(1,1)$ and $L_{22}(1,1)$ are about 5$\sim$15% higher compared to those predicted by PPSIM. This means that potential theory slightly under-estimates effect of uniform pressure loading on both self-induced and interference uniform inflow changes. A possible reason is effect of wake roll-ups due to air viscosity, which remain close to the rotors during hover flight condition. As the wake roll-ups are axi-symmetric in hover, these strong vortices induced uniform inflows on both upper and lower rotors. This results in slightly higher $L_{11}(1,1)$, $L_{21}(1,1)$ and $L_{22}(1,1)$. Next, the cosine and sine terms along the diagonal, i.e. indices (2,2) and (3,3) differs from PPSIM values by at most 15%, except for L_{12} (relates upper rotor inflows due to lower rotor pressure loading). Due to steady uniform downwash from upper rotor onto the lower rotor, fore-to-aft and side-to-side perturbations will have diminished effects on upper rotor inflows. In other words, lower rotor pressure loading effects would have diffused significantly when propagating against upper rotor downwash (which is also seen in $L_{12}(1,1)$). Finally, flow swirls (elements in indices (2,3) and (3,2)) are seen in all extracted L-matrix blocks. In particular, swirl effects are significant in $[L_{22}]$ which is expected since the lower rotor operates within upper rotor wake, altering the flow fields at the lower rotor.

Next, L-matrix elements are extracted from VVPM data at an advance ratio of 0.12 and compared against PPSIM in Table. 5. Unlike the hover flight condition, terms associated with uniform inflow states, i.e. indices (1,1) and (1,2) are closer to those precomputed in PPSIM. This is because at high advance ratios, the flow field around the rotor disks are dominated by free-stream component resulting in higher Reynolds number compared to hover and low speeds. What this means is that the air flow behaves more like a potential flow and air viscosity effects are diminished. Terms related to fore-to-aft inflow states, such as indices (2,1) and (2,2) are slightly different than what PPSIM calculated. This might be due to small wake distortion

Table 4: Comparison of coaxial rotor PPSIM L-matrix elements in hover

Elements[1]	Extracted from VVPM[2]	PPSIM
$L_{11}(1,1)$	0.8615	0.7500
$L_{11}(2,2)$	0.7164	0.6250
$L_{11}(2,3)$	0.1522	0.0000
$L_{11}(3,2)$	-0.1628	0.0000
$L_{11}(3,3)$	0.7114	0.6250
$L_{12}(1,1)$	0.4172	0.5290
$L_{12}(2,2)$	0.1333	0.3382
$L_{12}(2,3)$	-0.2688	0.0000
$L_{12}(3,2)$	0.2521	0.0000
$L_{12}(3,3)$	0.1213	0.3382
$L_{21}(1,1)$	1.0125	0.9709
$L_{21}(2,2)$	0.8192	0.9118
$L_{21}(2,3)$	0.2284	0.0000
$L_{21}(3,2)$	-0.2469	0.0000
$L_{21}(3,3)$	0.8060	0.9118
$L_{22}(1,1)$	0.8851	0.7500
$L_{22}(2,2)$	0.5463	0.6250
$L_{22}(2,3)$	-0.6473	0.0000
$L_{22}(3,2)$	0.6031	0.0000
$L_{22}(3,3)$	0.5146	0.6250

[1]First index is row number and second index is column
[2]Only non-zero elements in extracted L-matrix are shown

effects present in the coaxial rotor system at this advance ratio. Interestingly, only fore-to-aft pressure coefficients have influences on the side-to-side inflow states, although the effect is small as seen from terms with indices (3,2). Finally, side-to-side pressure coefficient perturbation only excites side-to-side inflow states on upper and lower rotors; with negligible effects on other inflow state components, i.e. very small elements in indices (1,3) and (2,3). This is in agreement with the analytical coaxial rotor PPSIM.

After conducting the analysis on extracted L-matrix elements, the next step is to apply L-matrix corrections (ΔL) on PPSIM. A step change (same magnitude used in VVPM simulation) to one pressure coefficient component is injected to both the original and L-matrix corrected coaxial rotor PPSIM. The resulting change in inflow states from the two models are then compared against VVPM results to illustrate the effectiveness of L-matrix corrections.

Figures 4 and 5 compare the change in rotors steady-state inflow states due to individual perturbations on upper and lower rotor pressure coefficients, respectively in hover flight condition. First, comparison of inflow state changes at hover flight conditions due to perturbations of upper rotor pressure loading are examined. In Fig. 4(a), appropriate corrections to the L-matrix increased the uniform inflow states for upper and lower rotors close to what VVPM predicts. Swirl effects are also correctly captured by the L-matrix corrected PPSIM as seen in Fig. 4(b), where upper and lower rotor side-to-side inflow states are perturbed due to change in fore-to-aft pressure coefficient. Similarly, side-to-side pressure coefficient also induced fore-to-aft inflow states on both upper and lower rotors in the L-matrix corrected PPSIM in Fig. 4(c). Next, effects of lower rotor pressure coefficient perturbations on inflow state changes are compared in Fig. 5. As expected, corrections to the L-matrix elements correctly captured wake diffusion effects on upper rotor inflows due to lower rotor uniform pressure coefficient perturbations in Fig. 5(a). Lastly, Figs. 5(b) and

Table 5: Comparison of coaxial rotor PPSIM L-matrix elements at advance ratio of 0.12

Elements[1]	Extracted from VVPM[2]	PPSIM
$L_{11}(1,1)$	0.7100	0.7500
$L_{11}(1,2)$	-0.2360	-0.4041
$L_{11}(2,1)$	0.8361	0.8082
$L_{11}(2,2)$	0.1148	0.2113
$L_{11}(2,3)$	0.0823	0.0000
$L_{11}(3,1)$	0.1367	0.0000
$L_{11}(3,2)$	-0.1753	0.0000
$L_{11}(3,3)$	0.8318	1.0387
$L_{12}(1,1)$	0.5276	0.5291
$L_{12}(1,2)$	-0.1697	-0.2587
$L_{12}(1,3)$	0.0435	0.0000
$L_{12}(2,1)$	0.5002	0.5173
$L_{12}(2,2)$	0.0632	0.1209
$L_{12}(2,3)$	-0.0379	0.0000
$L_{12}(3,1)$	-0.0707	0.0000
$L_{12}(3,2)$	0.1317	0.0000
$L_{12}(3,3)$	0.5096	0.5555
$L_{21}(1,1)$	0.5979	0.6259
$L_{21}(1,2)$	-0.2236	-0.4542
$L_{21}(2,1)$	0.8821	0.9085
$L_{21}(2,2)$	-0.0676	-0.1919
$L_{21}(2,3)$	0.0687	0.0000
$L_{21}(3,1)$	0.1496	0.0000
$L_{21}(3,2)$	-0.1600	0.0000
$L_{21}(3,3)$	0.6293	0.8778
$L_{22}(1,1)$	0.7687	0.7500
$L_{22}(1,2)$	-0.2625	-0.3982
$L_{22}(1,3)$	0.0544	0.0000
$L_{22}(2,1)$	0.9600	0.7964
$L_{22}(2,2)$	0.0508	0.2234
$L_{22}(2,3)$	-0.0378	0.0000
$L_{22}(3,1)$	-0.1150	0.0000
$L_{22}(3,2)$	0.2165	0.0000
$L_{22}(3,3)$	0.9109	1.0266

[1]First index is row number and second index is column
[2]Only non-zero elements in extracted L-matrix are shown

5(c) showed changes in inflow states due to lower rotor fore-to-aft and side-to-side pressure coefficient perturbations, respectively. Here, lower rotor pressure loading change have smaller effects on upper rotor inflow states compared to what potential theory predicts. This is largely due to air viscosity and diffusion effects as explained earlier. Coupling between cosine and sine parts are also seen on both upper and lower rotors.

The comparison of inflow states between PPSIM and VVPM results at an advance ratio of 0.12 is presented in Figs. 6 and 7. In Fig. 6(a), small differences in uniform and fore-to-aft inflow states between original PPSIM and VVPM results are observed. This is expected because at higher advance ratios, air viscosity have weaker effects on flows around the rotors. In addition, elements in both upper and lower rotor mass flow parameters are dominated by free-stream components; which means change in induced velocities due to rotor loading perturbations are negligible. Interestingly, secondary effects due to uniform pressure coefficient perturbations show up as small changes to side-to-side inflow states in VVPM results. These effects on upper and lower rotors are captured by $\Delta L_{11}(3,1)$ and $\Delta L_{21}(3,1)$, respectively (refer to Table. 5). Next, inflow state changes due to perturbation in upper rotor fore-to-aft pressure coefficient is shown in Fig. 6(b). Minor corrections to uniform and fore-to-aft inflow states due to small wake distortions and secondary effects on side-to-side inflow states are are well captured by ΔL. Lastly, side-to-side pressure coefficient perturbations mainly changes upper and lower rotor side-to-side inflow states as seen in Fig. 6(c). Inflow state changes due to perturbations of lower rotor pressure coefficients comparison between L-matrix corrected, original PPSIM and VVPM are shown in Fig. 7. Similarly, minor corrections to inflow states via ΔL improves correlations with VVPM results. Swirl effects captured by corrections to original PPSIM L-matrix are also seen upper and lower rotor inflow results.

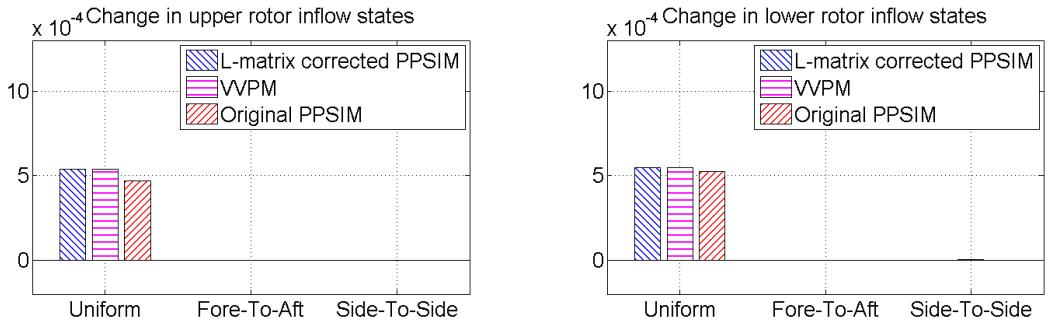

(a) Perturbation of upper rotor uniform pressure coefficient

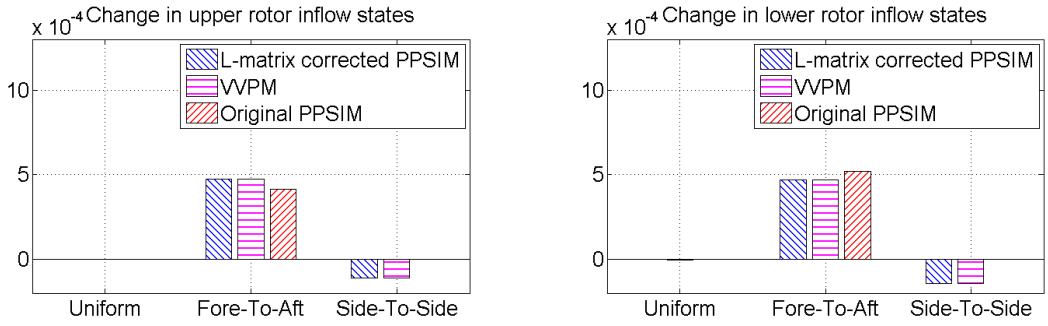

(b) Perturbation of upper rotor fore-to-aft pressure coefficient

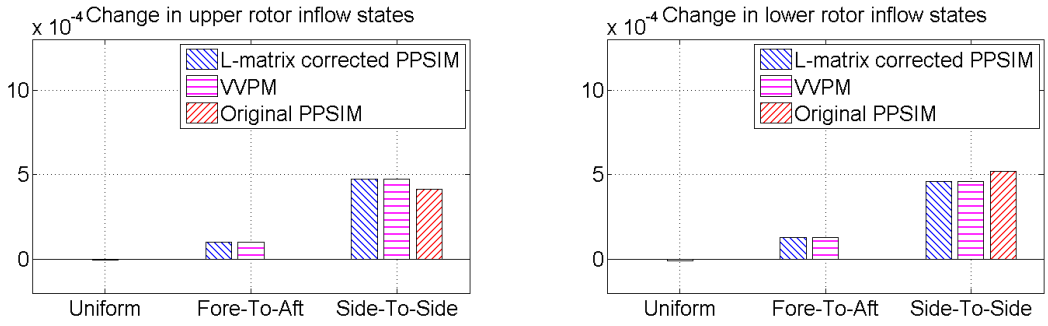

(c) Perturbation of upper rotor side-to-side pressure coefficient

Figure 4: Comparison of steady-state inflow states due to upper rotor pressure coefficient perturbations in hover

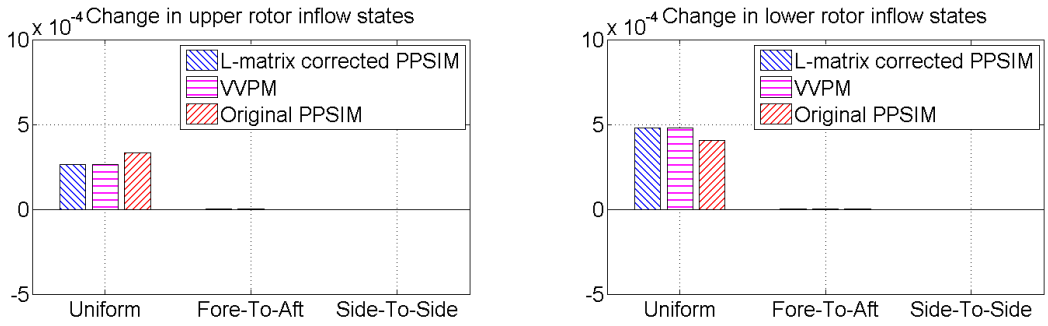

(a) Perturbation of lower rotor uniform pressure coefficient

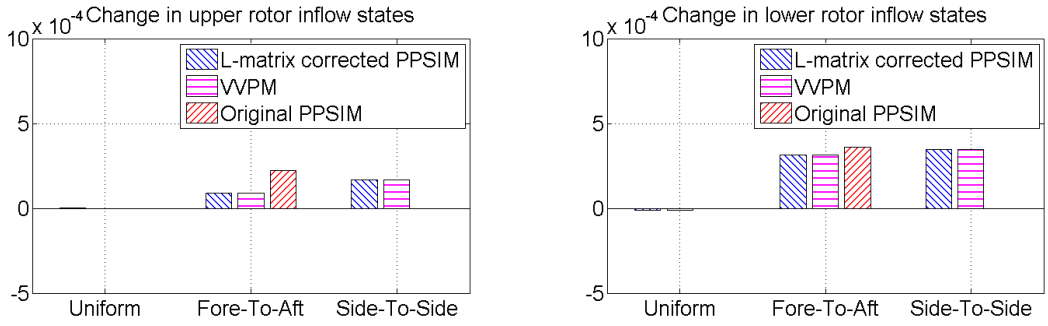

(b) Perturbation of lower rotor fore-to-aft pressure coefficient

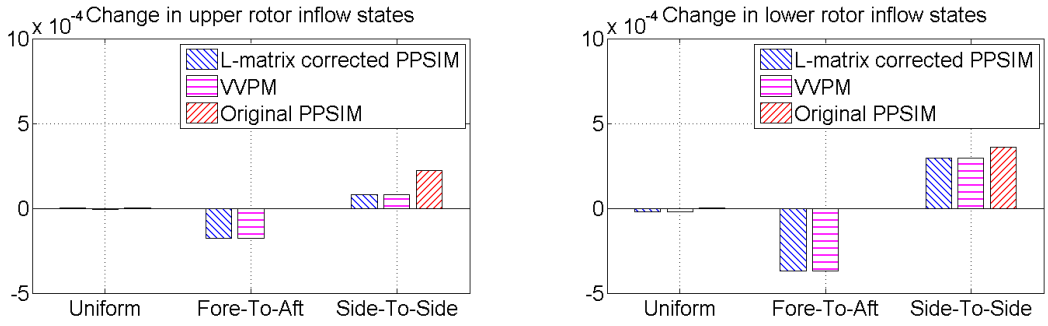

(c) Perturbation of lower rotor side-to-side pressure coefficient

Figure 5: Comparison of steady-state inflow states due to lower rotor pressure coefficient perturbations in hover

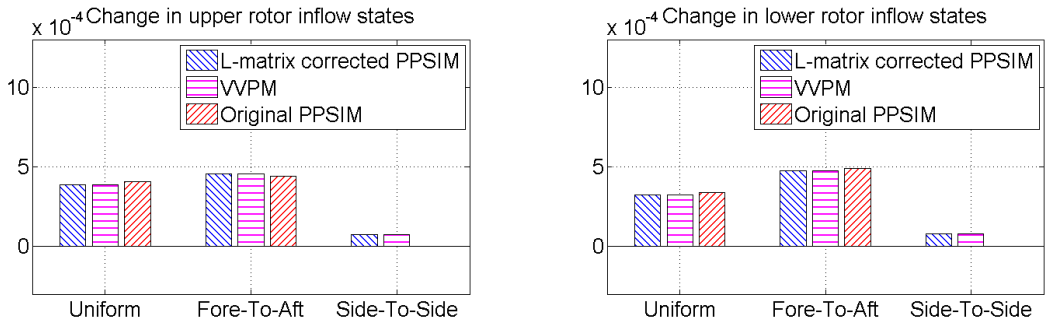

(a) Perturbation of upper rotor uniform pressure coefficient

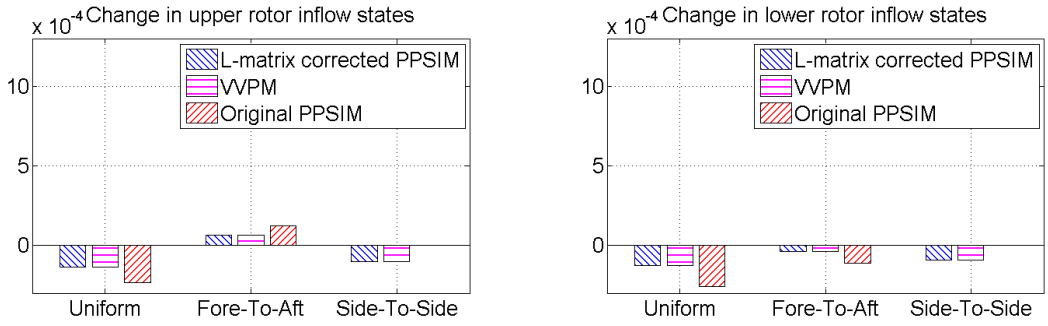

(b) Perturbation of upper rotor fore-to-aft pressure coefficient

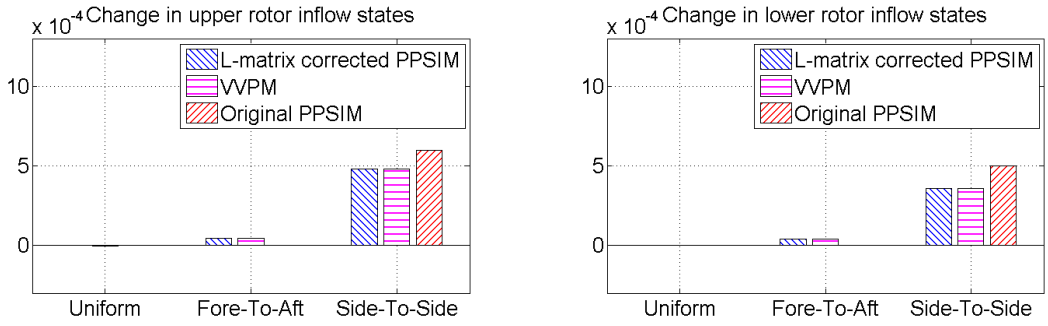

(c) Perturbation of upper rotor side-to-side pressure coefficient

Figure 6: Comparison of steady-state inflow states due to upper rotor pressure coefficient perturbations at advance ratio 0.12

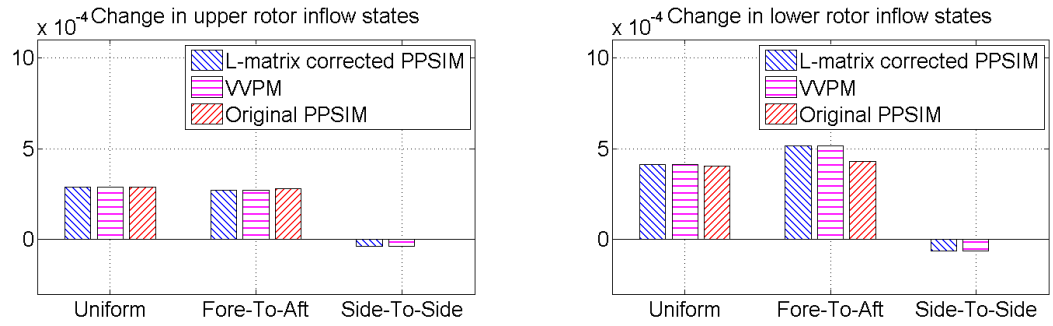

(a) Perturbation of lower rotor uniform pressure coefficient

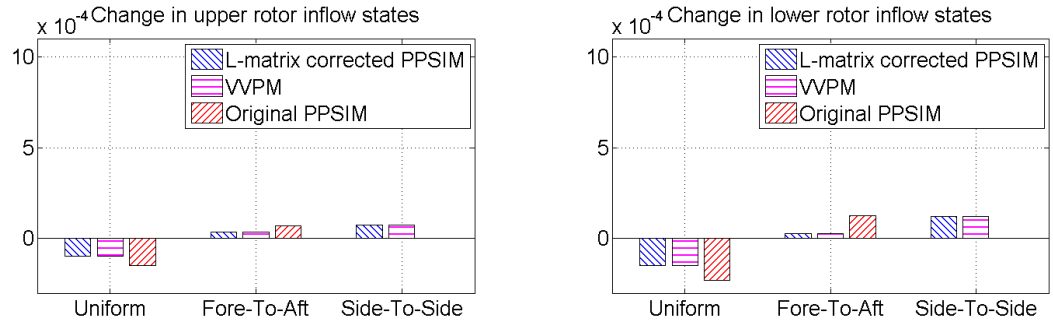

(b) Perturbation of lower rotor fore-to-aft pressure coefficient

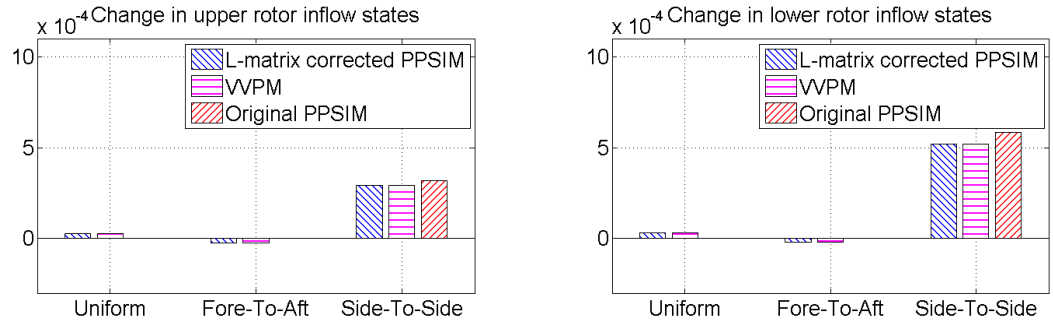

(c) Perturbation of lower rotor side-to-side pressure coefficient

Figure 7: Comparison of steady-state inflow states due to lower rotor pressure coefficient perturbations at advance ratio 0.12

While comparing inflow state changes due to individual pressure coefficient perturbations between PPSIM and VVPM provides detailed insights to effectiveness of L-matrix correction terms, it is useful to quantify the results into a few values for ease of comparison among different flight conditions. In view of this, the 2-norm of all inflow states change corresponding to original PPSIM, L-matrix corrected PPSIM and VVPM results for every pressure coefficient perturbations are computed using Eq. (44). Since three inflow states are used to represent induced downwash at each rotor, the limit of summation is fixed at $6 \times 6 = 36$, i.e. 6 pressure coefficient perturbations, each with 6 inflow states corresponding to both upper and lower rotors. Furthermore, 2-norm of inflow state differences between PPSIM and VVPM are also calculated as shown in Eq. (45).

$$\|A\|_2 = \sqrt{\sum_{i=1}^{36} |\Delta\alpha_i|^2} \tag{44}$$

$$\|\Delta A\|_2 = \sqrt{\sum_{i=1}^{36} |\Delta\alpha_{i,\text{PPSIM}} - \Delta\alpha_{i,\text{VVPM}}|^2} \tag{45}$$

Values of $\|A\|_2$ corresponding to the original and L-matrix corrected PPSIM are compared against VVPM results across a range of advance ratios shown in Table. 6. Corrections to L-matrix elements in the original PPSIM are effective in reducing inflow state differences with VVPM results. A significant portion of $\|\Delta A\|_2$ corresponding to the original PPSIM in hover is mainly due to neglect of cosine-sine coupling effects, although correlation of uniform inflow states with VVPM data is good. In terms of overall trend in VVPM inflow data, it is noticed that $\|A\|_2$ is higher at advance ratio of 0.07 compared to hover case. This is because in hover, coupling between pressure coefficients and inflow states (except cosine-sine) are relatively weak. But as advance ratio increases, coupling effects becomes significant, i.e. uniform pressure coefficient perturbation now induces inflow state changes to uniform and fore-to-aft components.

Table 6: Comparison of $\|A\|_2$ for different advance ratios with $C_{T,1} = C_{T,2}$

Adv. ratio	VVPM	L-matrix corrected PPSIM	Original PPSIM[1]
Hover	1.5322×10^{-3}	1.5321×10^{-3}	1.4208×10^{-3} (6.7162×10^{-4}, 43.83%)
0.07	1.7392×10^{-3}	1.7392×10^{-3}	1.8130×10^{-3} (5.3356×10^{-4}, 30.68%)
0.12	1.4597×10^{-3}	1.4597×10^{-3}	1.5864×10^{-3} (4.0733×10^{-4}, 27.90%)
0.20	9.7976×10^{-4}	9.7971×10^{-4}	1.0304×10^{-3} (3.5996×10^{-4}, 36.74%)

[1]Bracket values represent $\|\Delta A\|_2$ and $\frac{\|\Delta A\|_2}{\text{VVPM } \|A\|_2} \times 100\%$, respectively

As such, this resulted in slight increase in $\|A\|_2$. As advance ratio increases to 0.12, $\|A\|_2$ drops which is brought about by significant decrease in induced inflows as flow fields are dominated by free-stream component. Further increase of advance ratio to 0.20 results in larger drop in induced inflows on both upper and lower rotors, which showed up as having the smallest $\|A\|_2$.

4.2.3 Sensitivity of extracted L-matrix to different initial rotor loading

The results presented so far are based on same initial upper and lower rotor uniform pressure coefficients of 0.003. In other words, the thrust sharing ratio is unity, i.e. $C_{T,1}/C_{T,2} = 1.0$; where $C_{T,1}$ and $C_{T,2}$ corresponds to upper and lower rotor thrust coefficients, respectively. In real flight situations, this might not always be the case due to balancing of upper and lower rotor torques. In particular at hover and low advance ratios, inflows are mainly induced by rotors' thrust coefficients. As such, a sensitivity study is conducted to investigate how elements of extracted L-matrix from VVPM data change with different thrust sharing ratios at different advance ratios. From experiments conducted on isolated coaxial rotors [23, 4], upper rotor thrust coefficient

is typically about 10∼20% higher than that of the lower rotor for torque balancing. In view of this, the sensitivity study investigates the case of $C_{T,1}/C_{T,2} = 1.2$ and $C_{T,1}/C_{T,2} = 0.8$ to represent upward and downward thrust directions, respectively.

With the procedure described in earlier chapter, elements in each delta L-matrix blocks are extracted from simulation runs of VVPM coaxial rotor model operating at different thrust sharing ratio and advance ratios. Each element in $[\Delta L_{11}]$ and $[\Delta L_{21}]$ are plotted against upper rotor wake skew function, as shown in Figs. 8 and 9, respectively. Similarly, elements in $[\Delta L_{12}]$ and $[\Delta L_{22}]$ are plotted against the lower rotor wake skew function shown in Figs. 10 and 11, respectively. Every subplot corresponds to one element in the delta L-matrix block with each point representing the correction at one X_{skew}. Notice that each cluster of points corresponds to one advance ratio, with each point in the cluster representing different thrust sharing ratios. In addition, curve-fitted correlation between each correction element and X_{skew} are shown as solid lines. For simplicity and practical application, the maximum order of fit is limited to two which is a quadratic function.

To assess the fitting quality, goodness-of-fit for each correlation are quantified using the coefficient of determination or R^2 statistic. In regression analysis, R^2 is a statistical measure of how close the data is to the fitted regression line by computing the square of correlation between the two. It can take on any value between 0 and 1, with a value closer to 1 indicating that a larger proportion of variance is accounted for by the fitted curve, i.e. good fit to given data. Table. 7 summarized the goodness-of-fit (R^2) for each curve-fit in the delta L-matrix blocks. Most of the correlations has R^2 above 0.90, meaning that the quadratic curve-fits capture variances in ΔL elements due to different thrust sharing ratio and advance ratios. This means that corrections to the L-matrix are known for any given X_{skew}; similar to the table look-up process. In other words, during real-time flight simulations, both the original L-matrix elements and corresponding correction terms are obtained from values of X_{skew}.

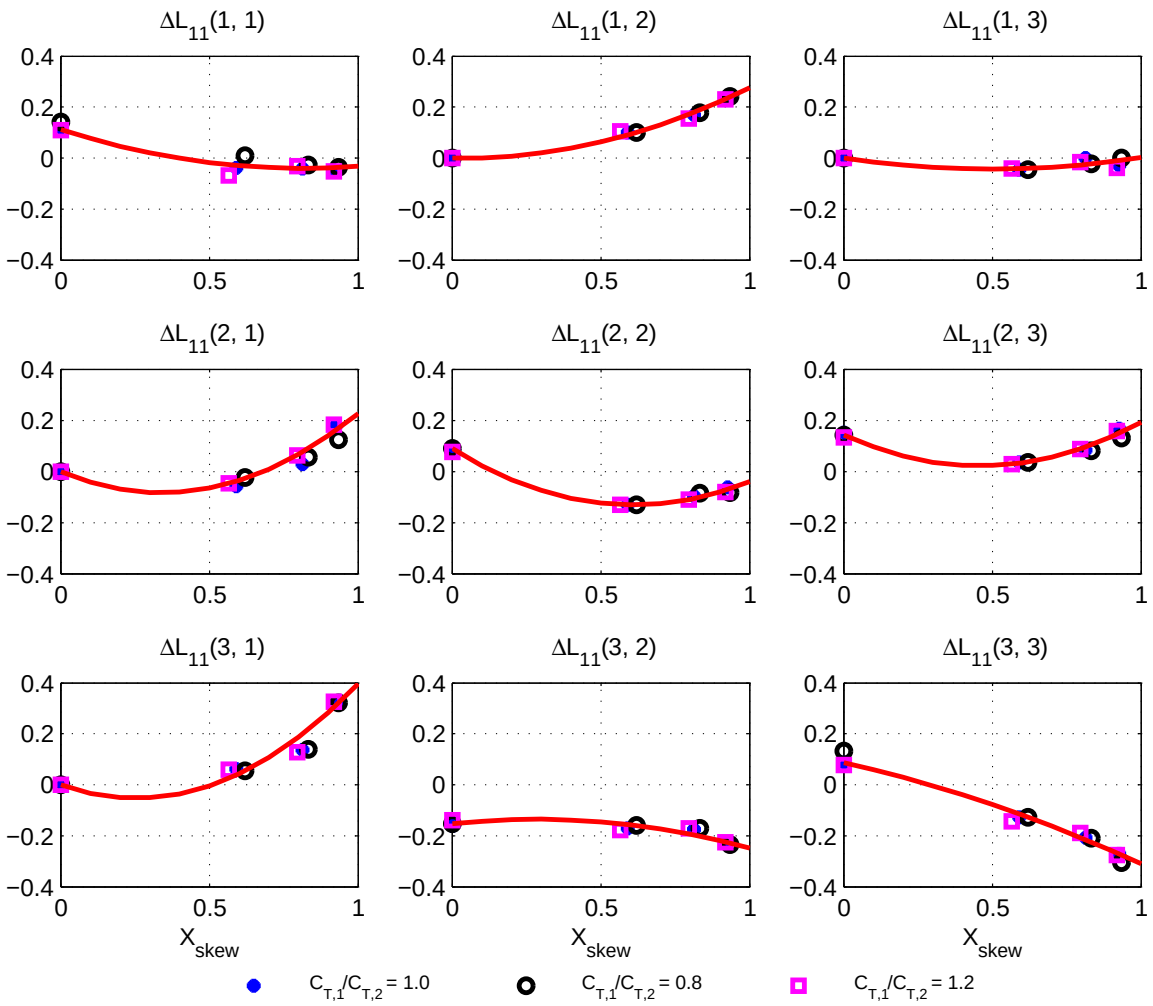

Figure 8: Curve-fitted correlation (solid line) between elements in $[\Delta L_{11}]$ and upper rotor wake skew function

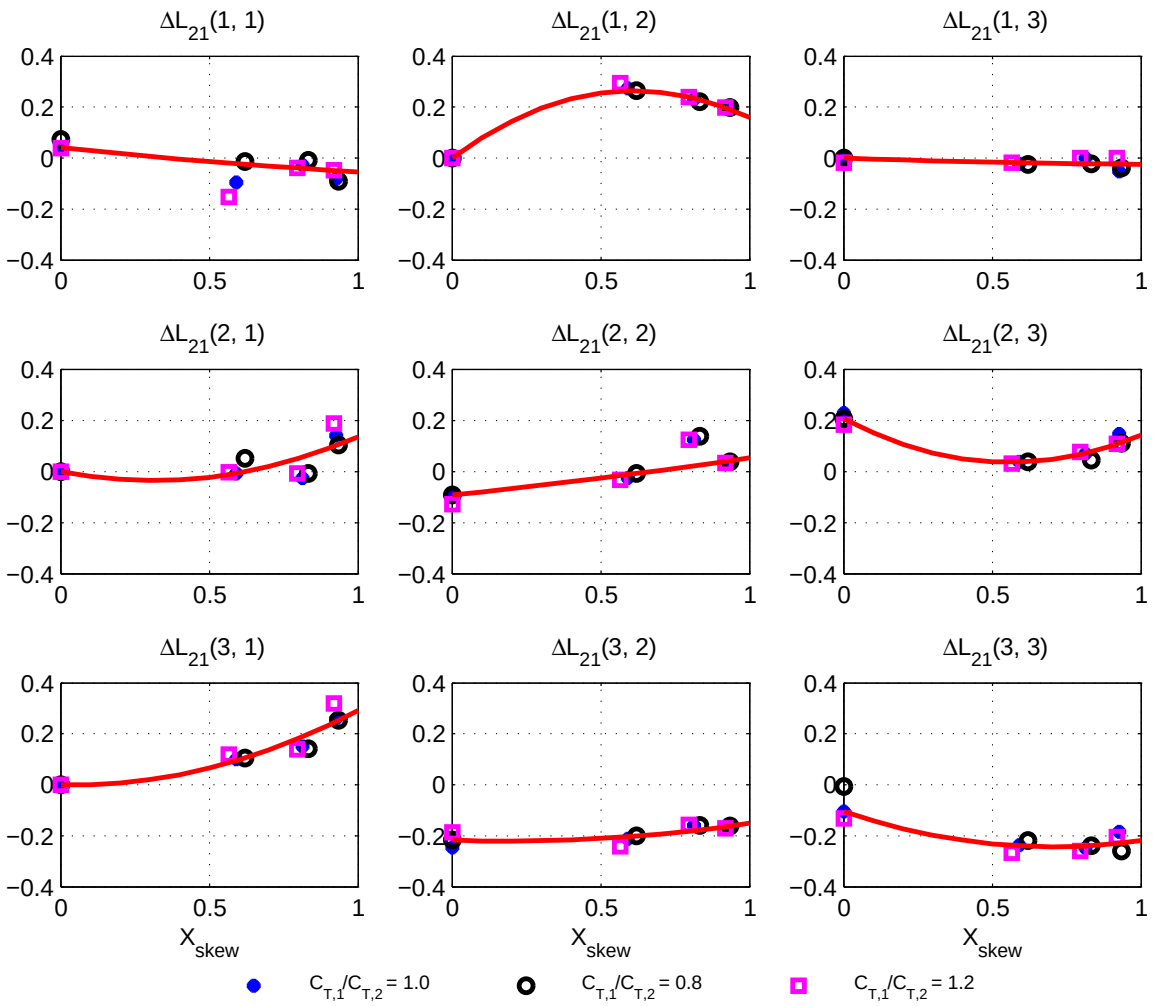

Figure 9: Curve-fitted correlation (solid line) between elements in $[\Delta L_{21}]$ and upper rotor wake skew function

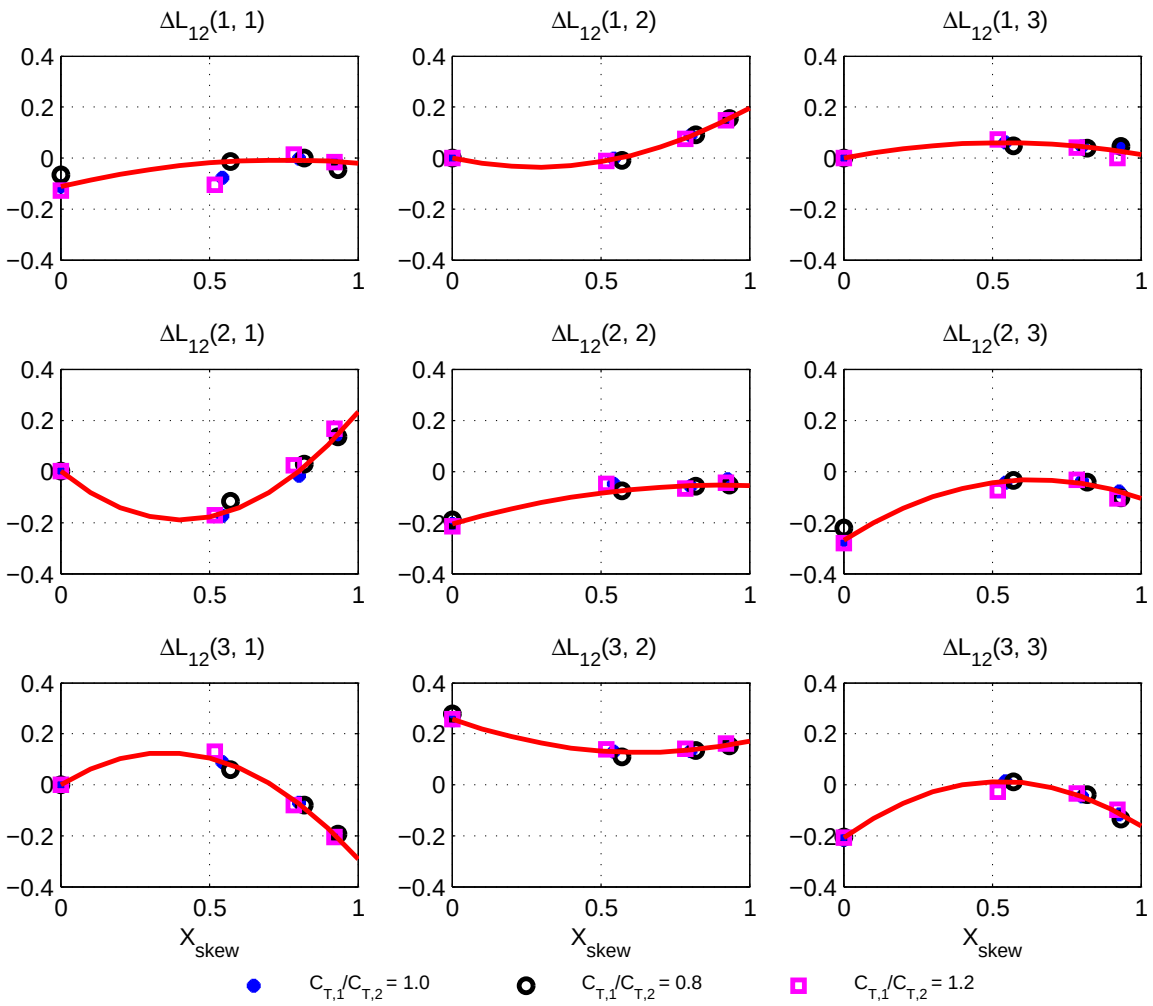

Figure 10: Curve-fitted correlation (solid line) between elements in $[\Delta L_{12}]$ and lower rotor wake skew function

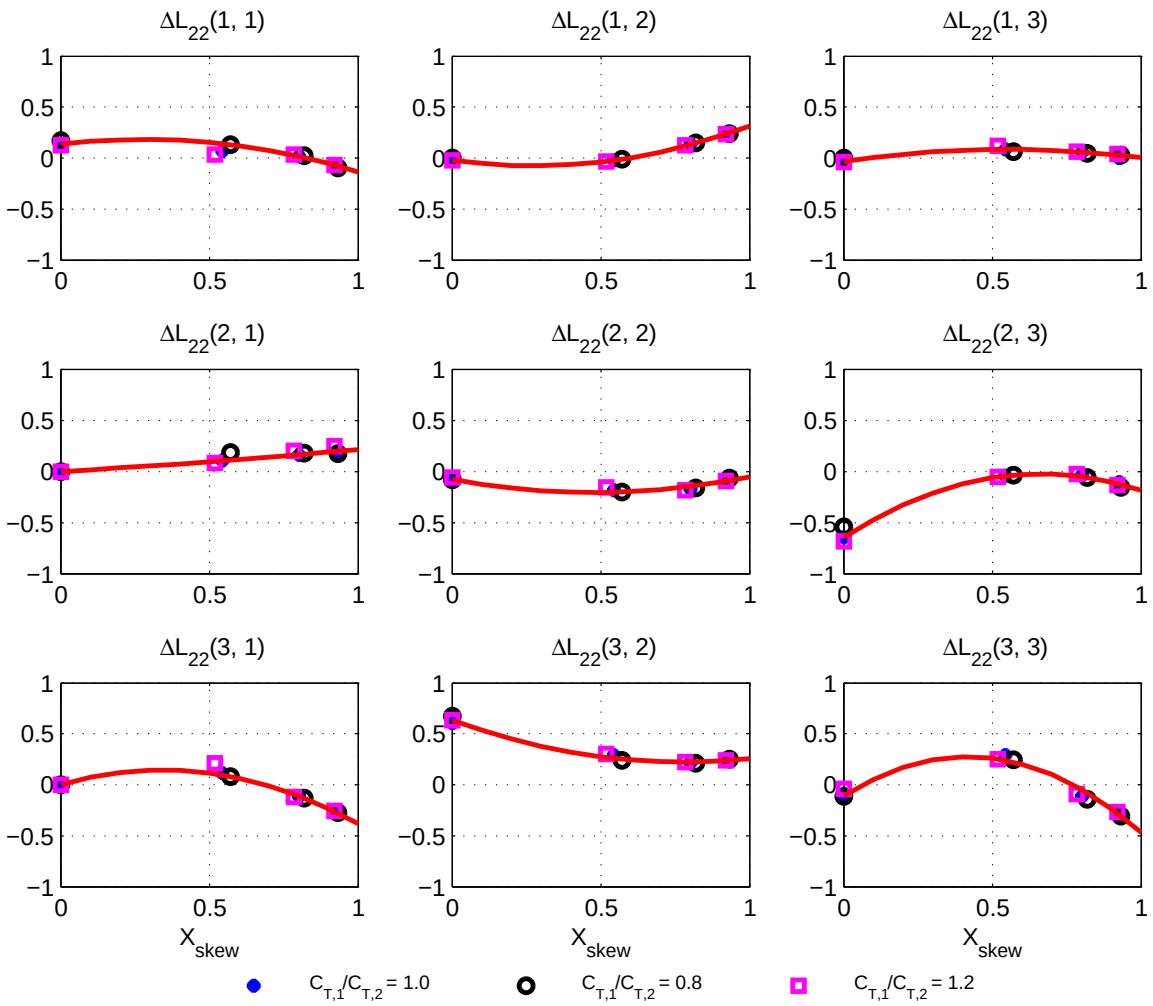

Figure 11: Curve-fitted correlation (solid line) between elements in $[\Delta L_{22}]$ and lower rotor wake skew function

Table 7: Goodness-of-fit (R^2) for curve-fitted correlation between ΔL elements and corresponding X_{skew}

ΔL blocks	R^2			ΔL blocks	R^2		
	0.9170[1]	0.9888	0.5318		0.4178	0.9969	0.7606
ΔL_{11}	0.9102	0.9893	0.9349	ΔL_{12}	0.9651	0.9399	0.9469
	0.9145	0.7153	0.9783		0.9845	0.9742	0.9690
	0.4033	0.9908	0.0925		0.9444	0.9946	0.8454
ΔL_{21}	0.4899	0.8757	0.9330	ΔL_{22}	0.8598	0.8023	0.9794
	0.8891	0.6189	0.7669		0.9869	0.9855	0.9553

[1]Values closer to 1 indicate a greater proportion of variance is accounted for by the curve fit

Alternatively, the corrections can be applied to precomputed L-matrix lookup table before simulation. Note that while R^2 for element $\Delta L_{21}(1,3)$ is very low (0.0925), the correction values are actually very small compared to other elements in the L-matrix block as observed in Fig. 9.

Finally, to evaluate the amount of error introduced when using the curve-fitted ΔL in PPSIM to compute rotor inflow states, Table. 8 summarized the comparison against VVPM results in terms of $\|A\|_2$ at selected flight conditions. The maximum difference between VVPM and curve-fitted ΔL PPSIM is about 10%, with an average value of 6%. The amount of error incurred from using curve-fitted L-matrix corrections is acceptable, seeing how this approach simplifies the application of ΔL on the original PPSIM. Furthermore, steady-state inflow state differences between original PPSIM and VVPM is reduced by at least a factor of 3 when applying the curve-fitted L-matrix corrections.

The identification and application of corrections terms to PPSIM L-matrix has shown to be effective in capturing real flow effects such as air viscosity, flow swirls and wake contractions/distortions. The focus will now shift to PPSIM M-matrix

Table 8: Comparison of $\|A\|_2$ between VVPM and curve-fitted L-matrix corrected PPSIM at selected flight conditions

Adv. ratio	$\frac{C_{T,1}}{C_{T,2}}$	VVPM	PPSIM with curve-fitted ΔL	$\frac{\|\Delta A\|_2}{\text{VVPM } \|A\|_2} \times 100\%$
Hover	0.8	1.4598×10^{-3}	1.4268×10^{-3}	7.25%
	1.0	1.5322×10^{-3}	1.5333×10^{-3}	2.21%
	1.2	1.6344×10^{-3}	1.6462×10^{-3}	4.14%
0.07	0.8	1.7224×10^{-3}	1.6803×10^{-3}	4.55%
	1.0	1.7392×10^{-3}	1.7617×10^{-3}	5.62%
	1.2	1.7713×10^{-3}	1.8503×10^{-3}	10.22%
0.12	0.8	1.3521×10^{-3}	1.3720×10^{-3}	6.80%
	1.0	1.4597×10^{-3}	1.5038×10^{-3}	6.96%
	1.2	1.6256×10^{-3}	1.6445×10^{-3}	7.05%
0.20	0.8	8.6530×10^{-4}	8.8377×10^{-4}	3.96%
	1.0	9.7976×10^{-4}	9.7237×10^{-4}	3.92%
	1.2	1.1031×10^{-3}	1.0692×10^{-3}	5.53%

which influence its dynamic responses. Frequency responses corresponding to L-matrix corrected coaxial rotor PPSIM will be compared against VVPM results.

CHAPTER V

EVALUATION OF PPSIM FREQUENCY RESPONSES

The procedure used to obtain frequency responses from VVPM simulation is similar to that of step input (see section 4.1), except that a sinusoidal frequency sweep is injected instead. The frequency sweep range is from 0.05 to 4.5 Hz, similar to those used in the dynamic response analysis carried out in Ref. [9]. A chirp signal (normalized) shown in Fig. 12 is used to carry out the frequency sweep. Next, time histories of pressure coefficients and extracted inflow states from VVPM simulation runs are input to CIFER® to generate frequency response plots.

In linear model analysis, transfer functions for original and L-matrix corrected PPSIM can be obtained analytically from Eqs. (32) and (41), respectively. In the equations, V_T's are replaced by V's in the mass flow parameter and use the values before perturbations of pressure coefficients.

5.1 Maximum Unnoticeable Added Dynamics (MUAD) Envelopes

Differences in frequency responses between VVPM and PPSIM are compared using Bode plots superimposed with bounds known as the Maximum Unnoticeable Added Dynamics (MUAD) bounds [1] shown in Fig. 13. The MUAD (pronounced "mud") envelopes were developed by engineers at McDonnell Douglas Corporation in the 1980s to examine quality of matches between higher order systems, i.e. VVPM and their low order equivalents, i.e. PPSIM. The idea is that dynamics added to the system due to mismatch falling within the limits will be too small to be noticed by a pilot. The MUAD envelopes were drawn from results of the Neal-Smith program [26]. It is found that pilots are most sensitive to changes in dynamics between 1.0∼4.0

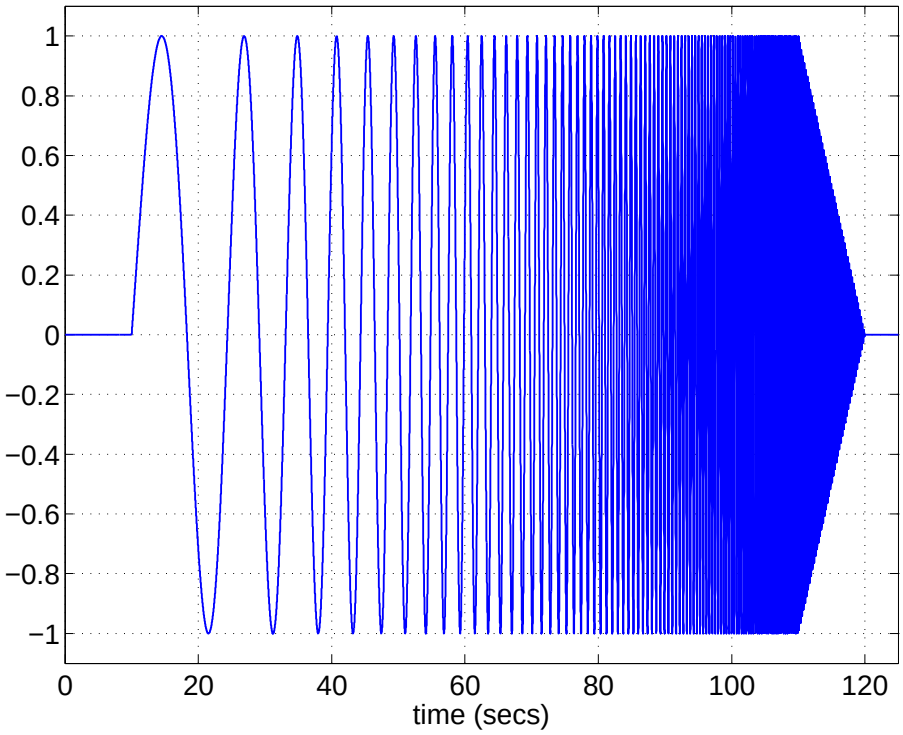

Figure 12: Normalised chirp signal used in frequency sweep

rad/s [1], resulting in the hourglass shape MUAD bounds in Fig. 13.

5.2 Computation of cost function from frequency response differences

For quantification of frequency differences between VVPM and PPSIM, a cost function, J given in Eq. (46) as described by Tischler [40] is used. In the equation, $|\Delta T|$ is the magnitude difference in dB between the two models for comparison at each frequency, ω. Similarly, $\angle\Delta T$ is the phase difference expressed in degrees at each frequency, n_ω is the number of frequency points and ω_1 and ω_{n_ω} are the starting and ending frequencies of fit, respectively. W_γ is a weighting function dependent on the value of coherence function from VVPM data at each frequency, while W_g and W_p are relative weights for magnitude and phase comparisons, respectively. As a guideline in flight dynamics modeling, a cost function of less than 50 means that differences between the two models is nearly indistinguishable in both frequency and time domains

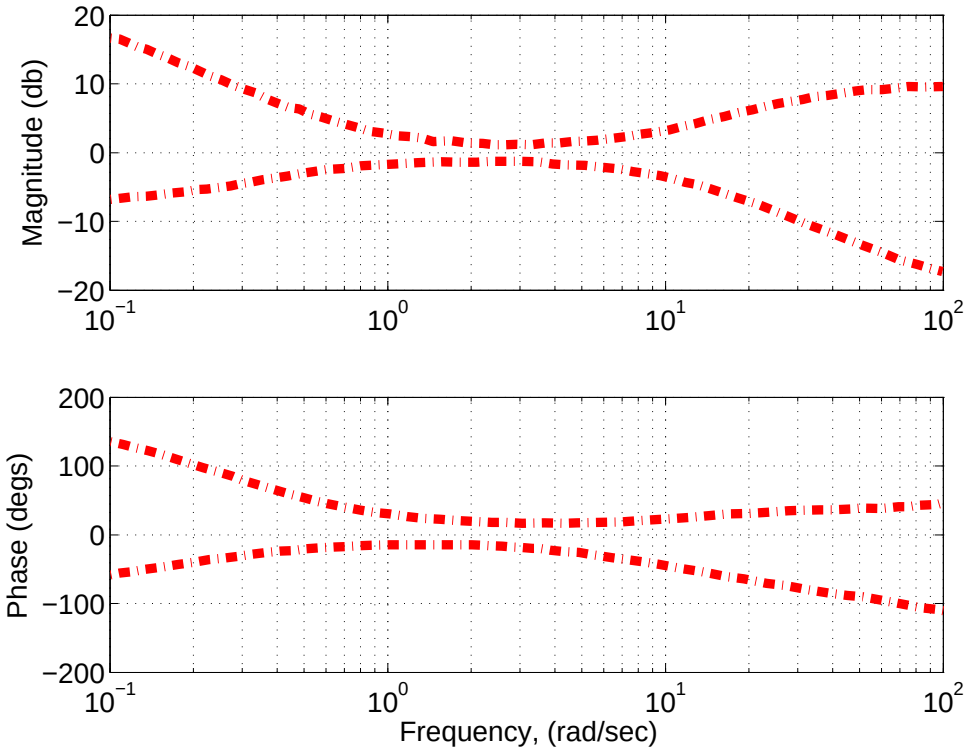

Figure 13: Envelopes of Maximum Unnoticeable Added Dynamics [1]

while a value of less than 100 generally reflects a good match between the models [40].

$$J = \frac{20}{n_\omega} \sum_{\omega_1}^{\omega_{n_\omega}} W_\gamma [W_g (|\Delta T|)^2 + W_p (\angle \Delta T)^2] \tag{46}$$

5.3 Single rotor validation

Frequency responses from VVPM single rotor model are validated against Peters-He inflow model to ensure the procedures are done correctly. Bode plots corresponding to uniform pressure coefficient perturbation in hover is shown in Fig. 14. As seen, only the uniform inflow state are excited while the fore-to-aft and side-to-side inflow states are very weak, which can be neglected. In Fig. 15, fore-to-aft and side-to-side inflow states are excited due to perturbation in fore-to-aft pressure coefficient. The side-to-side induced inflow state is due to swirl effects as seen when examining

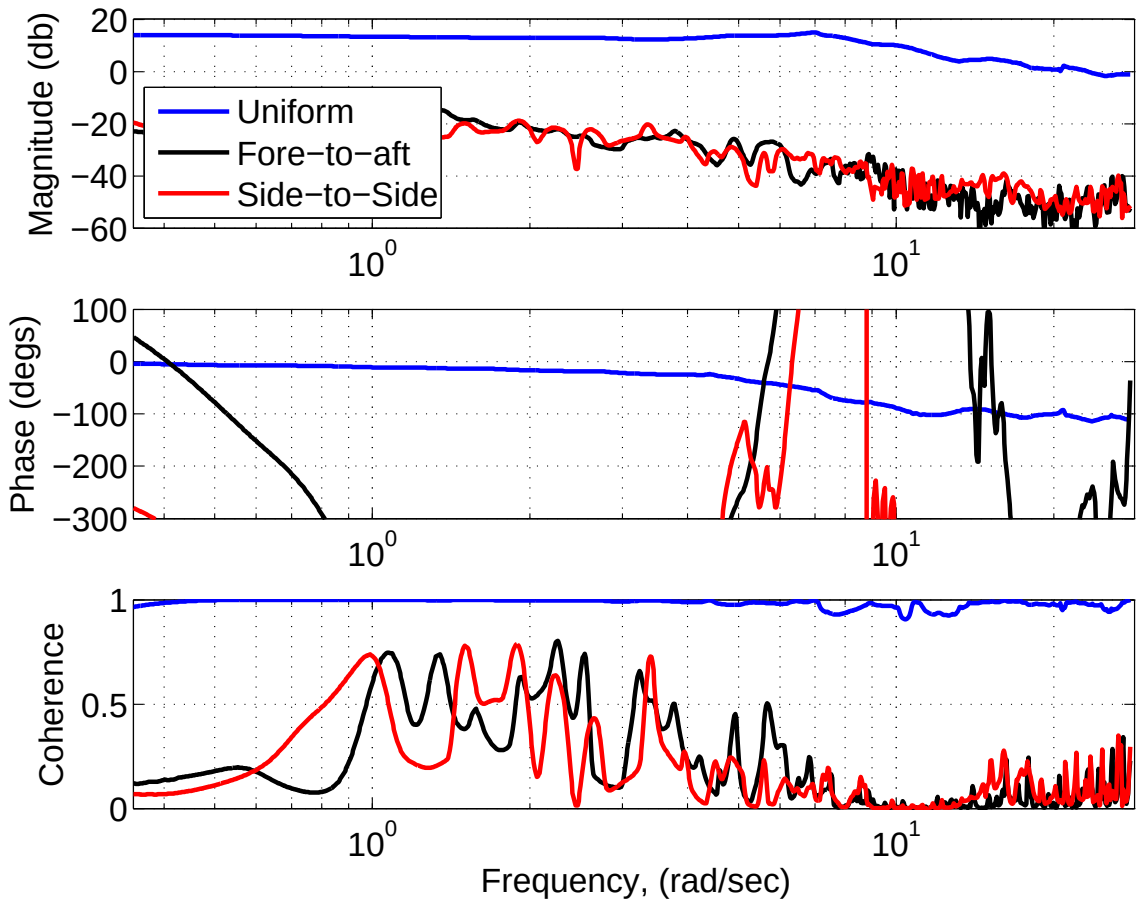

Figure 14: Bode plots of inflow states due to uniform pressure coefficient perturbation in VVPM single rotor model in hover

the single rotor L-matrix extracted from VVPM data. Frequency responses due to side-to-side pressure coefficient perturbation is similar to the fore-to-aft results due to axi-symmetric inflows in hover and is not shown.

Next, VVPM single rotor hover frequency responses are compared against Peters-He inflow model for uniform and fore-to-aft pressure coefficient perturbations. Bode plots of uniform inflow states extracted from VVPM data agrees very well with Peters-He inflow model prediction up to 4 rad/s as seen in Fig. 16. After that frequency, VVPM coherence begins to drop (indicating non-linearity in data) causing both magnitude and phase plot to deviate from Peters-He results. In Fig. 17, there are small differences between VVPM and Peters-He fore-to-aft inflow state frequency responses

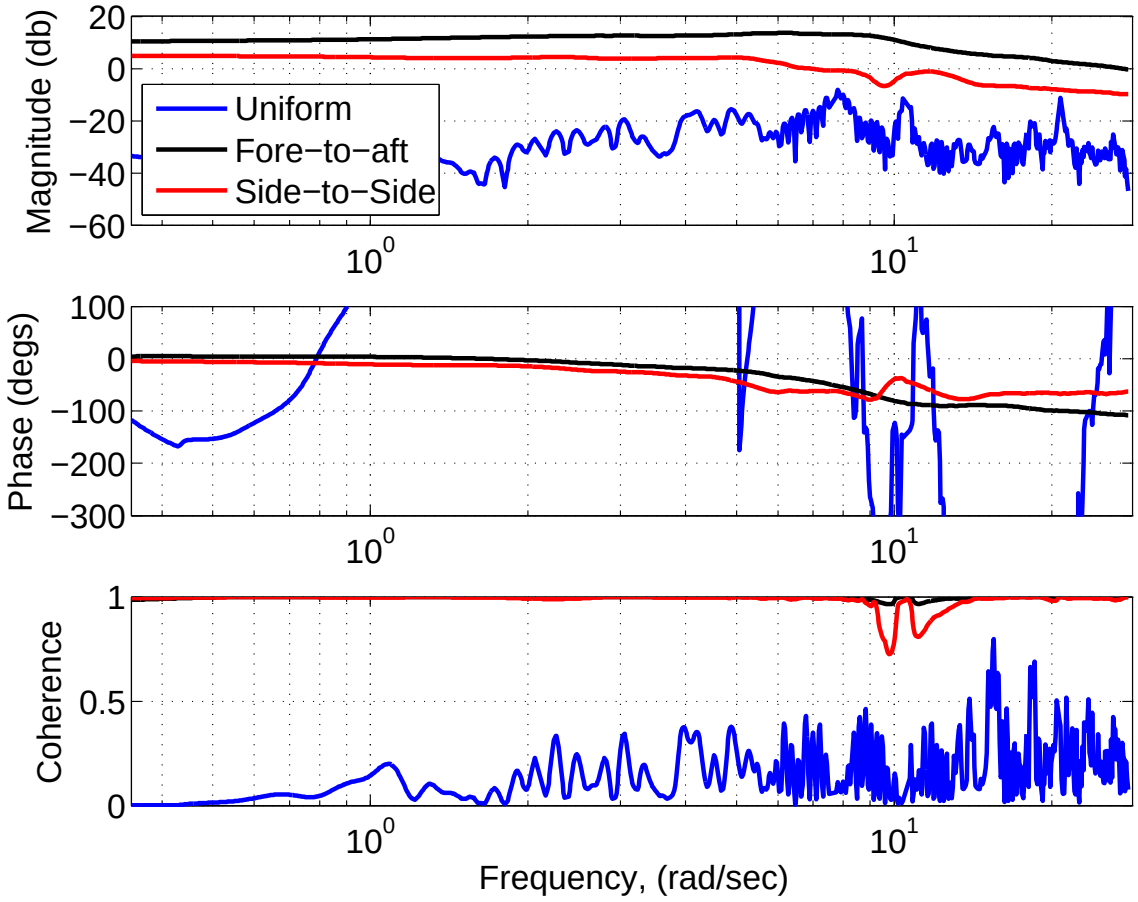

Figure 15: Bode plots of inflow states due to fore-to-aft pressure coefficient perturbation in VVPM single rotor model in hover

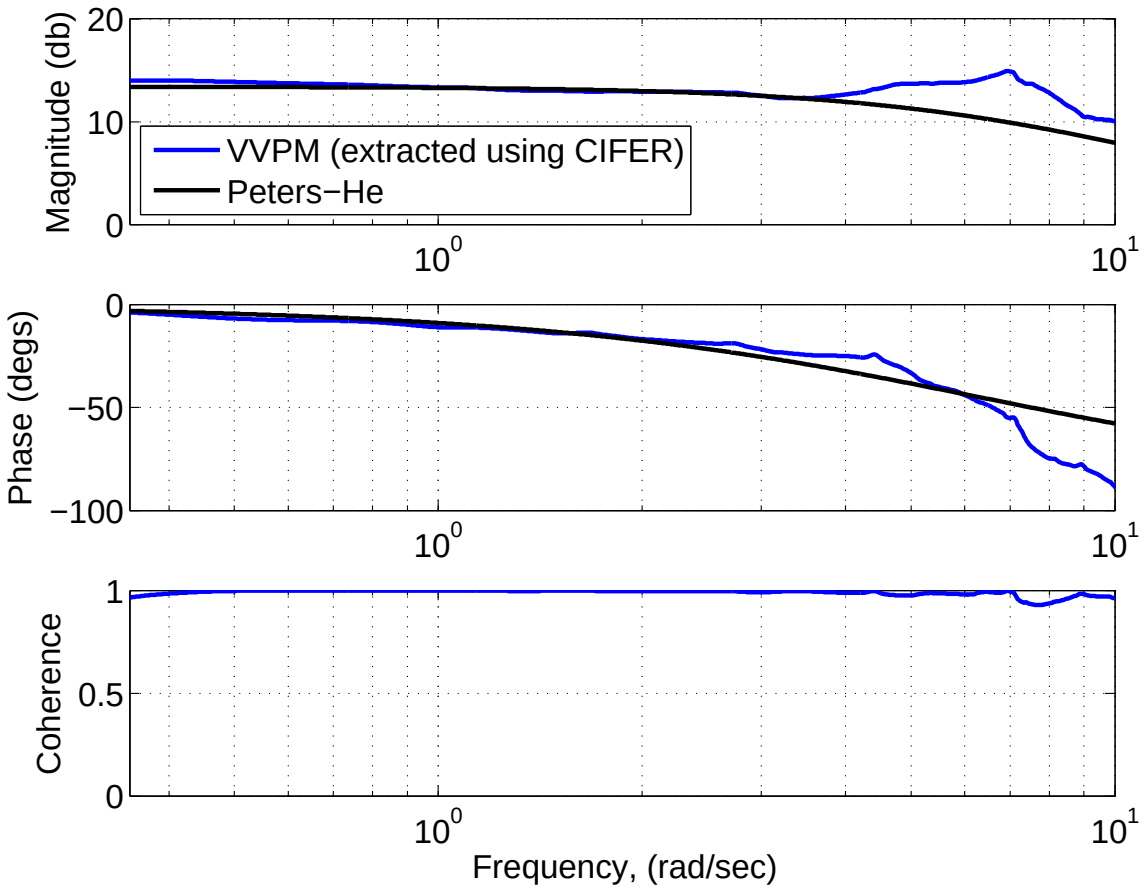

Figure 16: Validation of VVPM single rotor model uniform inflow state frequency responses in hover

at low frequencies. This observation is consistent with findings in Ref. [9], where the curve-fitted $L(2,2)$ from VVPM frequency response data showed a slightly lower value (0.5354) compare to Peters-He inflow model (0.6250). Also, slight phase differences of 5° is observed between VVPM and Peters-He inflow model at very low frequency range.

Similarly, Bode plots extracted from VVPM induced inflow data at advance ratio of 0.04 due to each pressure coefficient perturbations are analyzed. In Fig. 18, mainly the uniform and fore-to-aft inflow states are excited due to perturbation of the uniform pressure coefficient, which is expected. Coherence values for fore-to-aft inflow states begins to drop at around 4 rad/s, at approximate the same frequency where the phase

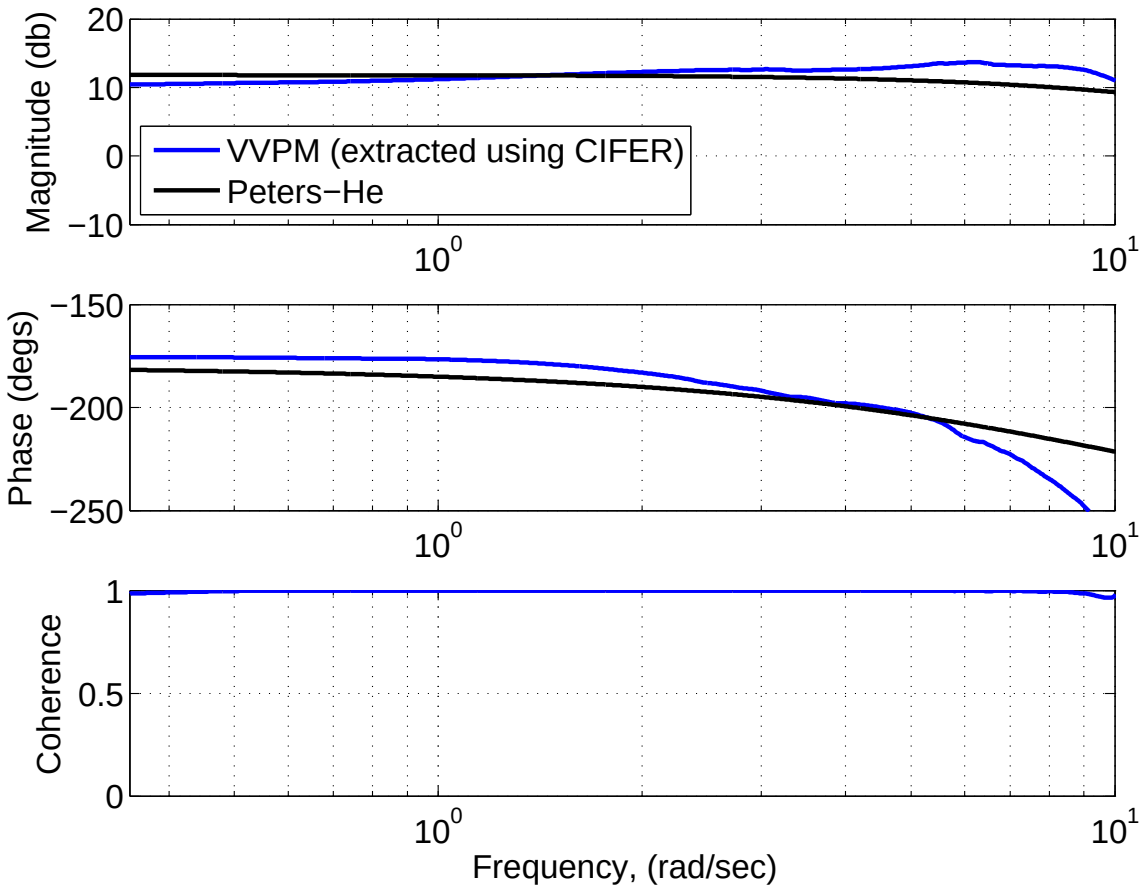

Figure 17: Validation of VVPM single rotor model fore-to-aft inflow state frequency responses in hover

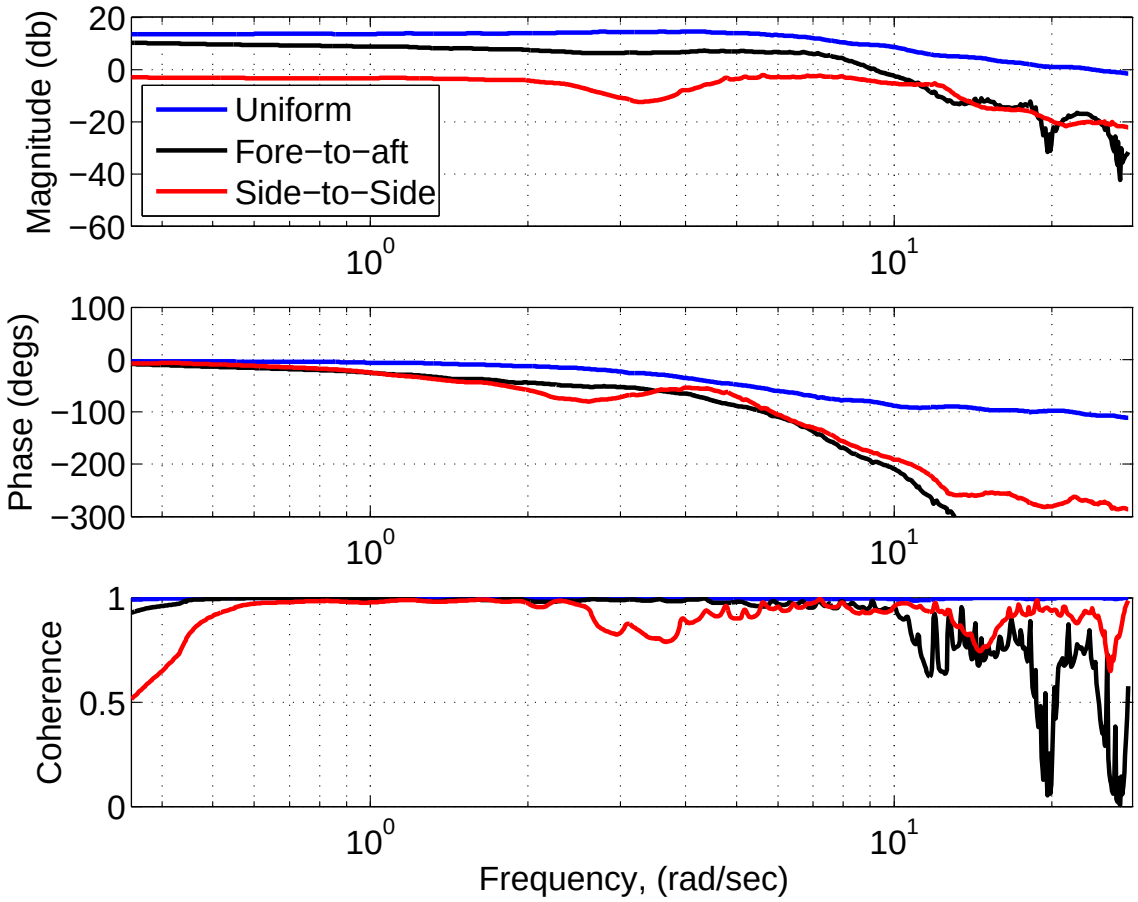

Figure 18: Bode plots of inflow states due to uniform pressure coefficient perturbation in VVPM single rotor model at advance ratio of 0.04

begins to roll off. Next, Bode plots of inflow states due to perturbation of fore-to-aft pressure coefficient in VVPM single rotor model is shown in Fig. 19. While all inflow states are excited, their magnitudes are much smaller compared to those excited by uniform and side-to-side pressure coefficient perturbations. Lastly, only side-to-side inflow states are excited with very weak fore-to-aft inflow state magnitudes as shown in Fig. 20 when subjected to side-to-side pressure coefficient perturbation.

Both uniform and fore-to-aft inflow states magnitude plots agrees well with Peters-He inflow model at low frequencies shown in Figs. 21 and 22, respectively.

Finally, frequency responses of VVPM inflow states due to fore-to-aft and side-to-side pressure coefficient perturbations also agrees well with Peters-He inflow model at

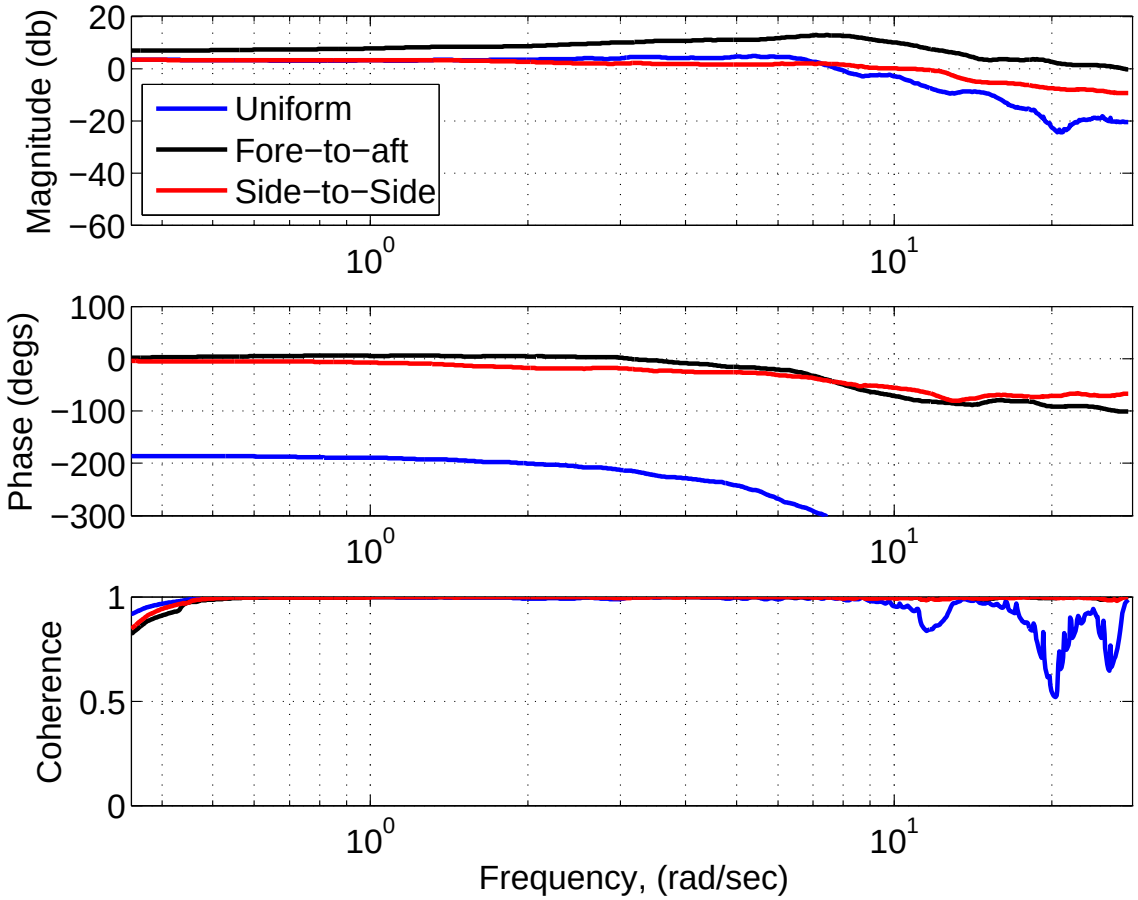

Figure 19: Bode plots of inflow states due to fore-to-aft pressure coefficient perturbation in VVPM single rotor model at advance ratio of 0.04

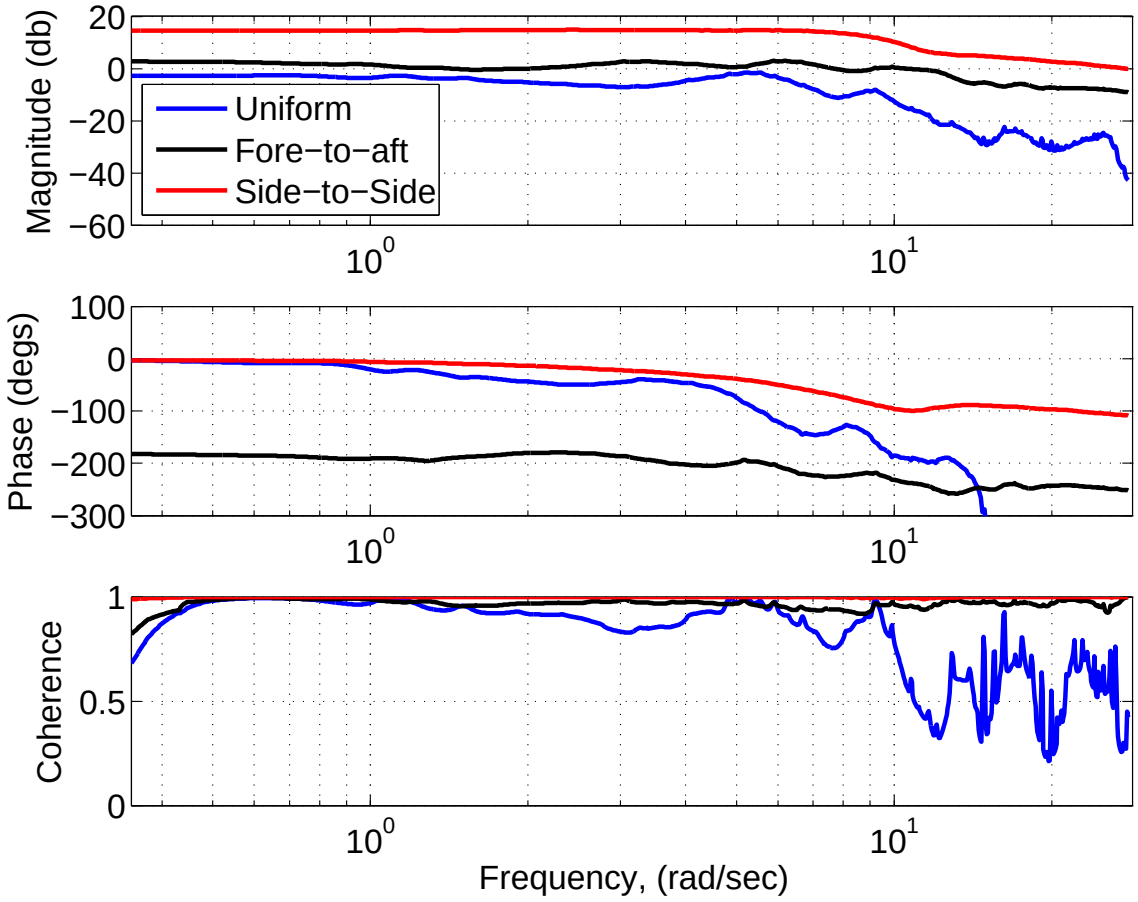

Figure 20: Bode plots of inflow states due to side-to-side pressure coefficient perturbation in VVPM single rotor model at advance ratio of 0.04

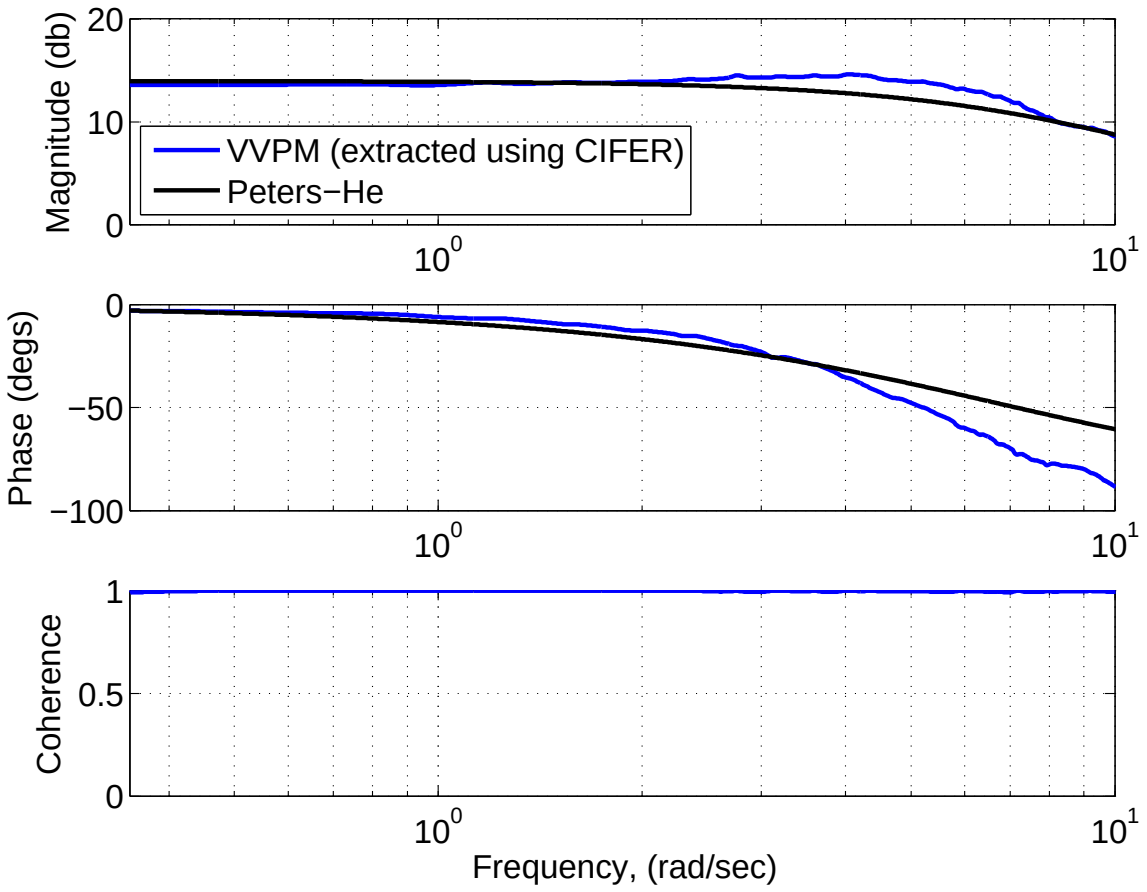

Figure 21: Validation of VVPM single rotor model uniform inflow state frequency responses due to uniform pressure coefficient perturbation at advance ratio of 0.04

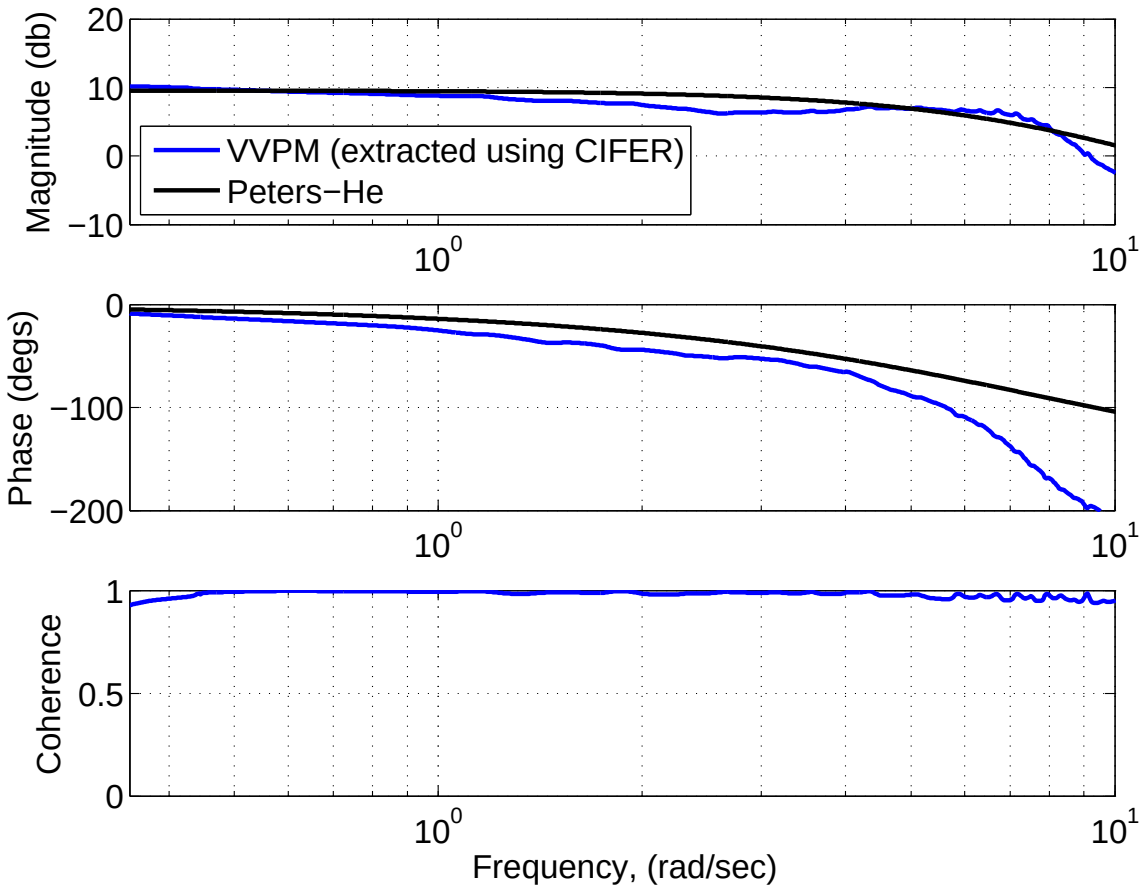

Figure 22: Validation of VVPM single rotor model fore-to-aft inflow state frequency responses due to uniform pressure coefficient perturbation at advance ratio of 0.04

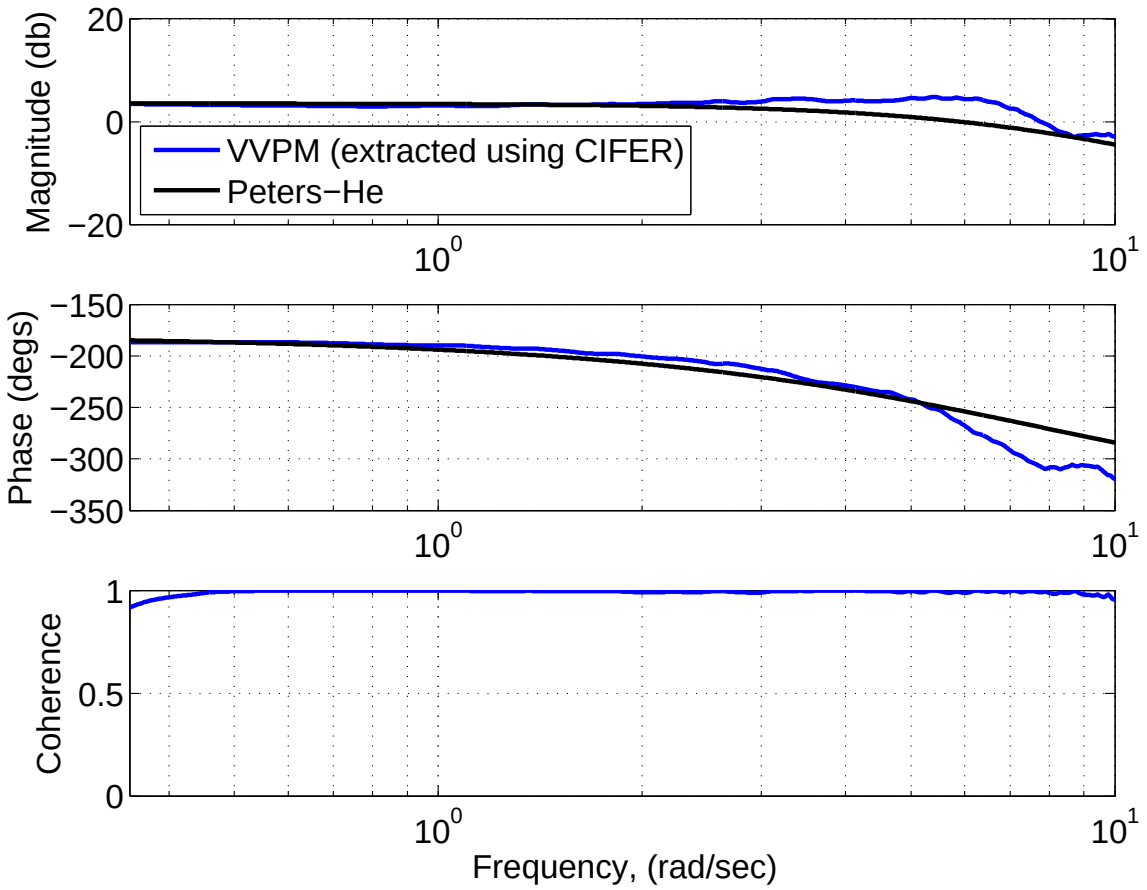

Figure 23: Validation of VVPM single rotor model uniform inflow state frequency responses due to fore-to-aft pressure coefficient perturbation at advance ratio of 0.04

advance ratio of 0.04 shown in Figs. 23 and 24, respectively. Although, side-to-side magnitude for VVPM is slightly higher than Peters-He inflow model prediction, this is likely due to wake roll-ups as explained earlier. Due to dis-symmetry of lift in forward flight, strength of vortices generated on the advancing and retreating sides are different. As such, this caused higher differences in side-to-side induced inflow states compared to potential flow.

5.4 VVPM coaxial rotor frequency responses

After validating single rotor results, frequency responses corresponding to VVPM Harrington coaxial rotor model is examined. Due to space constraints, only Bode plots due to selected pressure coefficient perturbations will be shown. Figure 25 shows

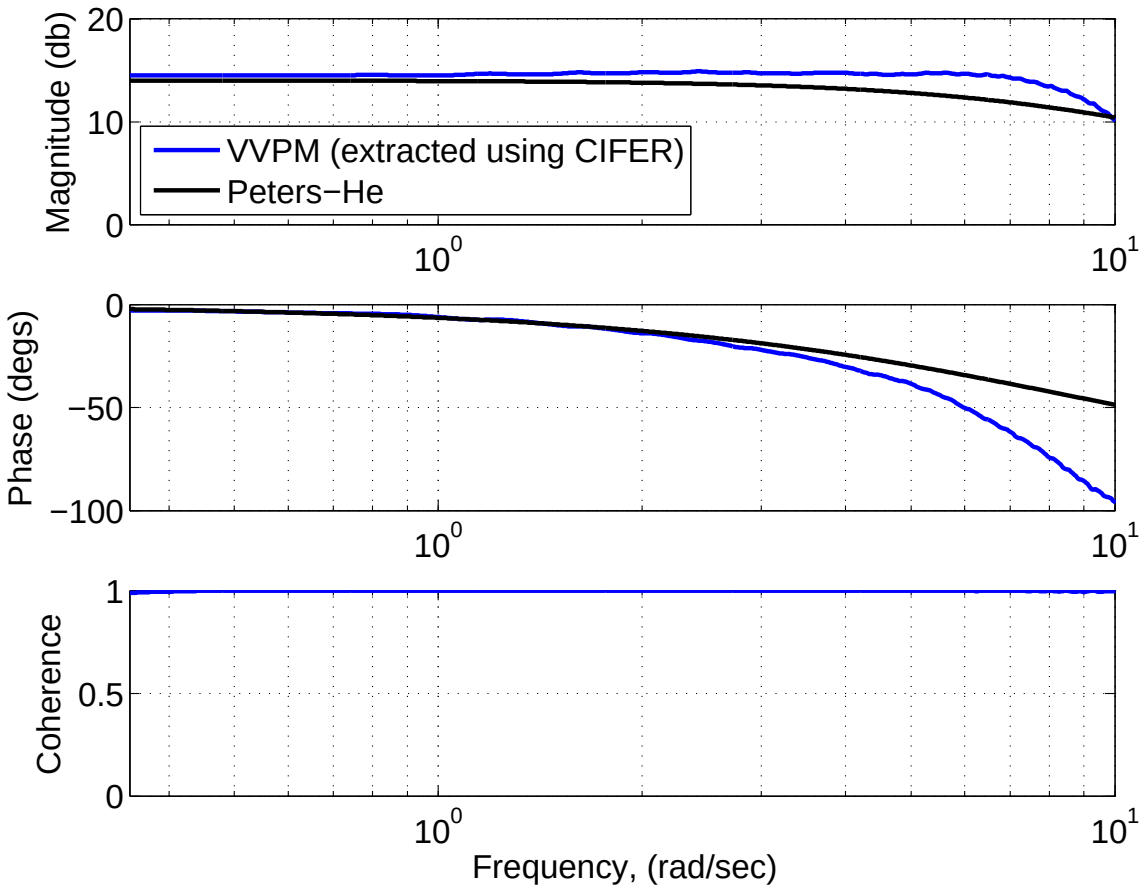

Figure 24: Validation of VVPM single rotor model side-to-side inflow state frequency responses due to side-to-side pressure coefficient perturbation at advance ratio of 0.04

the Bode plots of upper and lower rotor inflow states due to upper rotor fore-to-aft pressure coefficient excitation in hover. As seen, uniform inflow state magnitudes are very small compared to the other two components. Side-to-side inflow states at upper and lower rotors are excited due to coupling effects. In addition, lower rotor fore-to-aft and side-to-side inflow states have higher phases with increasing frequencies compared to those at the upper rotor. A possible reason is small time delay effects due to propagation of upper rotor induced velocity perturbations unto the lower rotor. Between 0.35 rad/s to 5 rad/s, inflow states frequency responses extracted from VVPM data showed coherence above 0.95, which mean the input-output correlations are linear in this region. Notice that phase plots corresponding to upper and lower rotor side-to-side inflow states are approximately -180° offset from the fore-to-aft component. This is due to flow swirl effects, i.e. cosine-sine couplings, where a positive fore-to-aft pressure coefficient perturbation causes a negative change in side-to-side inflow states (see VVPM results in Fig. 4(b)).

Next, Bode plots of inflow states due to frequency sweeps of lower rotor uniform pressure coefficient is shown in Fig. 26. As expected, only uniform inflow states are excited since the coaxial rotor model is operating in hover condition. Magnitude of upper rotor uniform inflow state is smaller compared to lower rotor, due to wake expansion above the lower rotor. In terms of phase, both upper and lower rotor uniform inflow states have almost the same values throughout the excitation frequency range. No time delay effects are observed here.

At advance ratio of 0.12, uniform and fore-to-aft inflow states at both rotors are excited due to upper rotor uniform pressure coefficient perturbation as seen in Fig. 27. The phase correspond to fore-to-aft inflow states decreases from 0° to -180°, which is characteristic of a second order transfer function. Next, Figs. 28 and 29 show the Bode plots due to upper and lower rotor fore-to-aft pressure coefficient perturbations, respectively. As seen in both figures, magnitudes for the fore-to-aft inflow states are

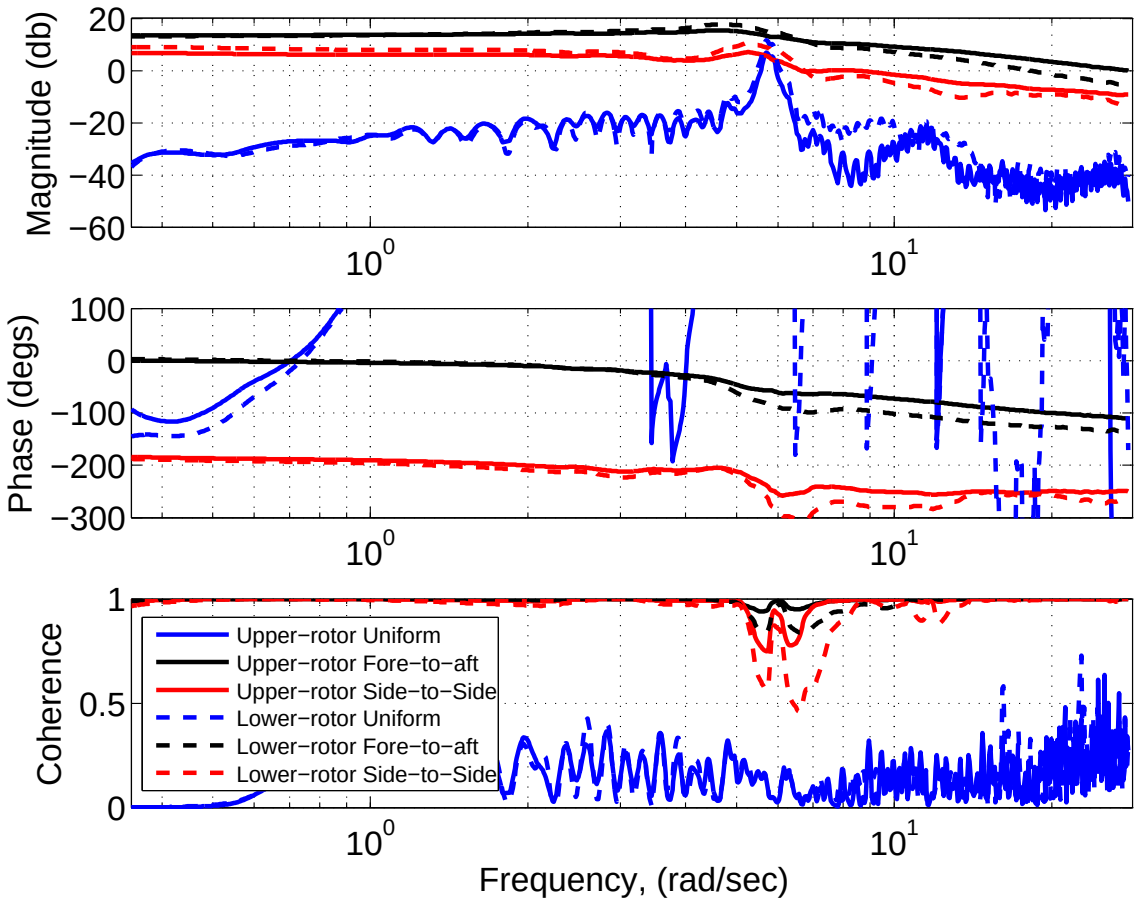

Figure 25: Bode plots of inflow states due to upper rotor fore-to-aft pressure coefficient perturbation in VVPM coaxial rotor model in hover

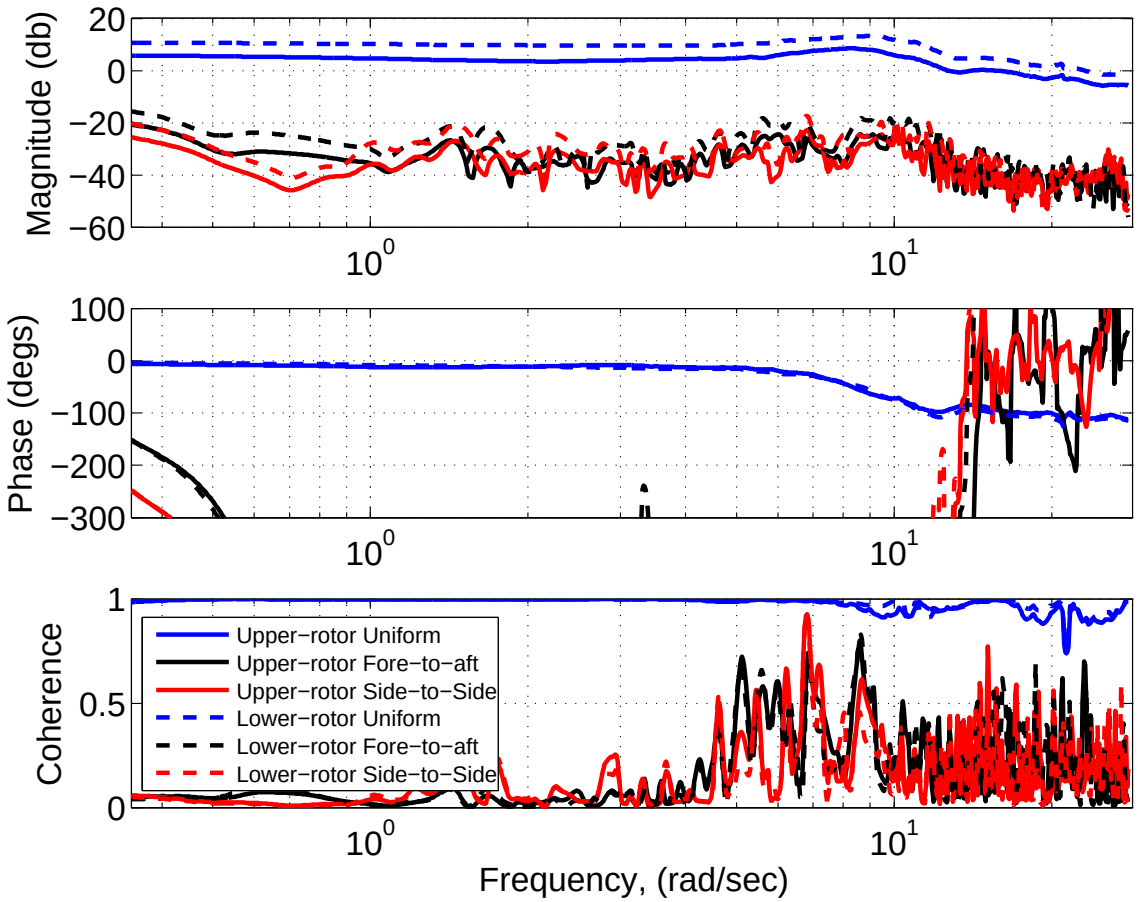

Figure 26: Bode plots of inflow states due to lower rotor uniform pressure coefficient perturbation in VVPM coaxial rotor model in hover

very small compared to other inflow state components. Also, the uniform and side-to-side inflow states are close to 0 dB, which is much smaller compared to the other cases seen so far. This means that not much inflows are induced on both upper and lower rotors due to fore-to-aft pressure coefficients perturbation at advance ratio of 0.12. In fact, this is also observed in step input case (see Figs. 6(b) and 7(b)) where magnitude of inflow state change is much smaller compare to other pressure coefficient perturbations cases. A possible reason is that at high advance ratios, vortices generated at the rotor's fore and aft region are swept downstream immediately after they are generated. As such, influences due to fore-to-aft pressure coefficient perturbations would have diffused significantly resulting in small induced inflows on the rotors. Finally, Fig. 30 shows Bode plots of inflow states due to perturbation on lower rotor side-to-side pressure coefficient. Only side-to-side inflow states on upper and lower rotors are excited, decoupled from other components. Here, strong wake roll-ups at advancing and retreating sides induced inflows at the rotors due to side-to-side pressure coefficient perturbations.

From the Bode plots results, it is seen that only on-axis responses on upper and lower rotors are significant when operating in hover. In forward flight, uniform and fore-to-aft inflow states are excited due to uniform pressure coefficient perturbations while side-to-side inflow states are decoupled from the other two components. Lastly, induced inflows due to fore-to-aft pressure coefficient perturbations are small in forward flight and can be neglected.

5.5 Frequency response comparisons between coaxial rotor PPSIM and VVPM

In this section, frequency responses from the original and L-matrix corrected PPSIM are compared against VVPM results. The comparisons are conducted for input-output responses that have good coherence (0.9 and above) across a range of frequencies and with considerable excitation, i.e. magnitude above 3 dB. The reason

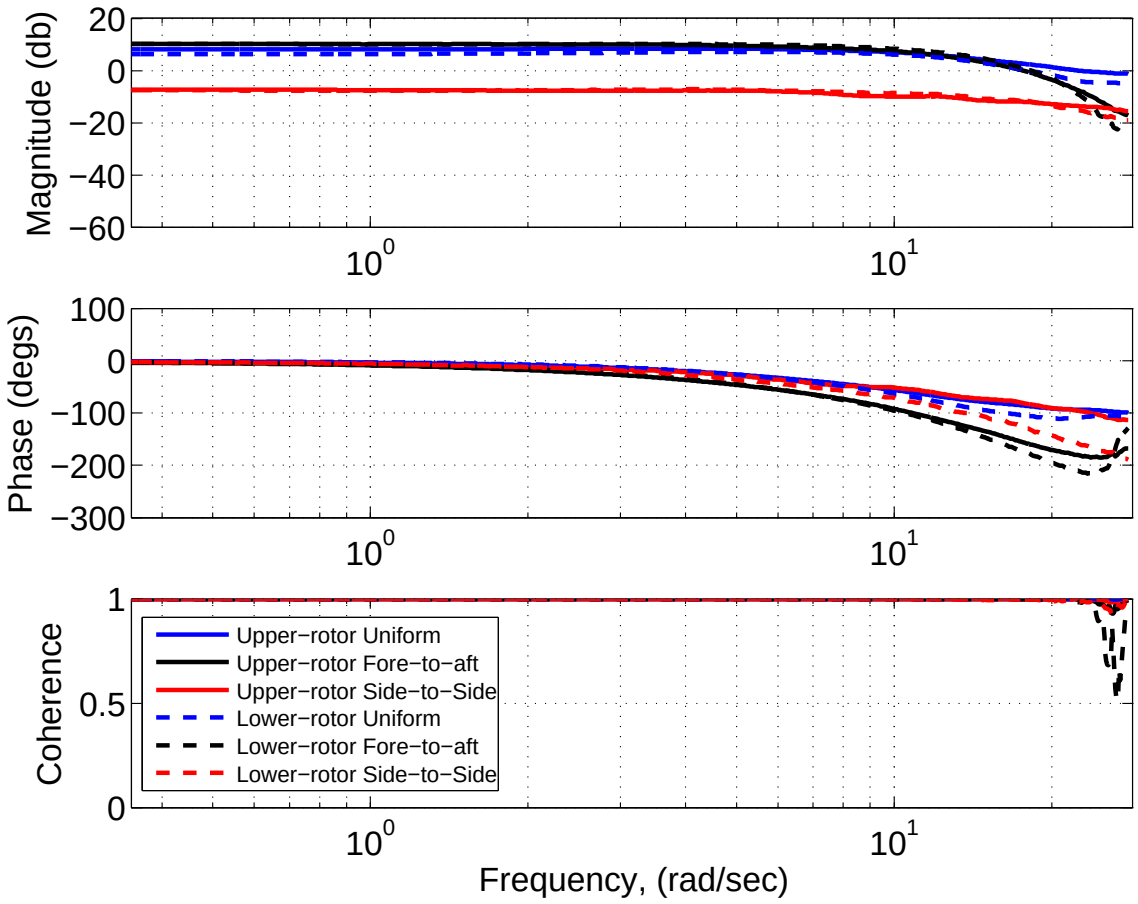

Figure 27: Bode plots of inflow states due to upper rotor uniform pressure coefficient perturbation in VVPM coaxial rotor model at advance ratio of 0.12

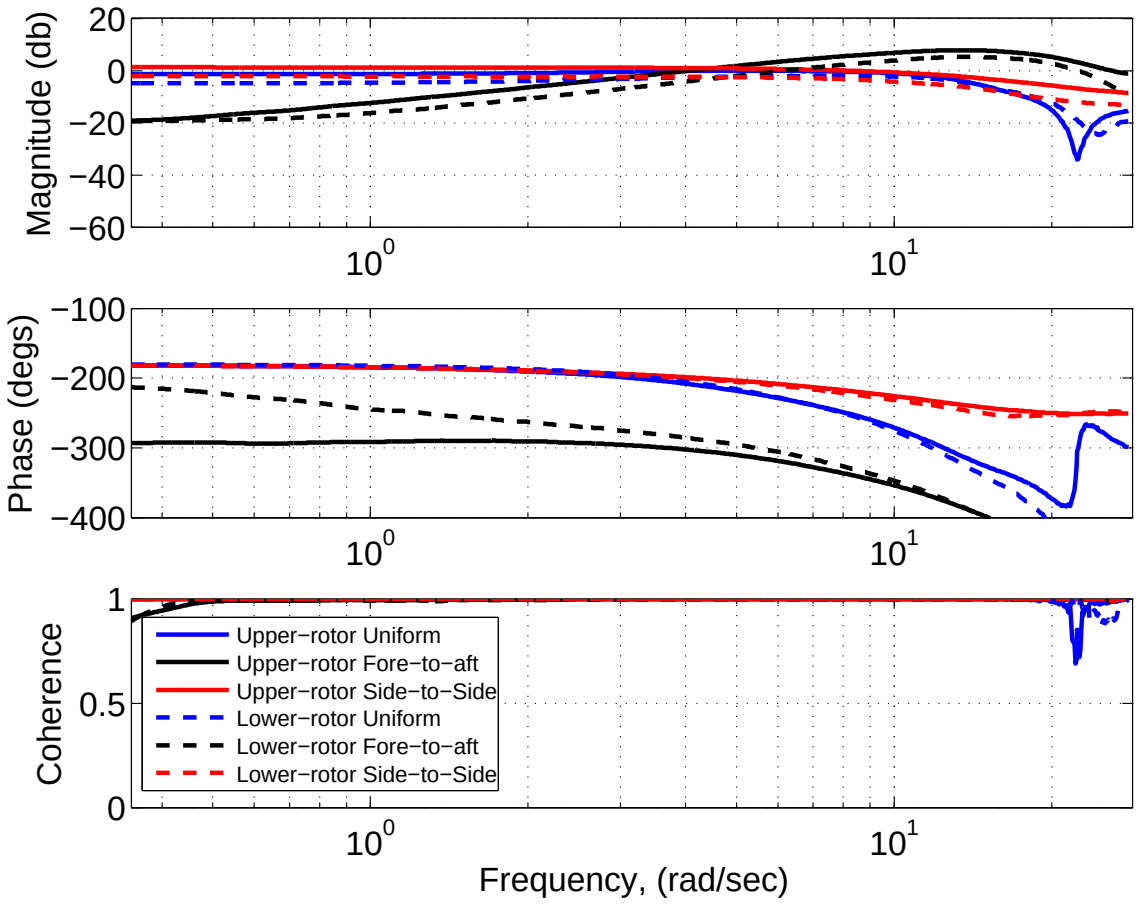

Figure 28: Bode plots of inflow states due to upper rotor fore-to-aft pressure coefficient perturbation in VVPM coaxial rotor model at advance ratio of 0.12

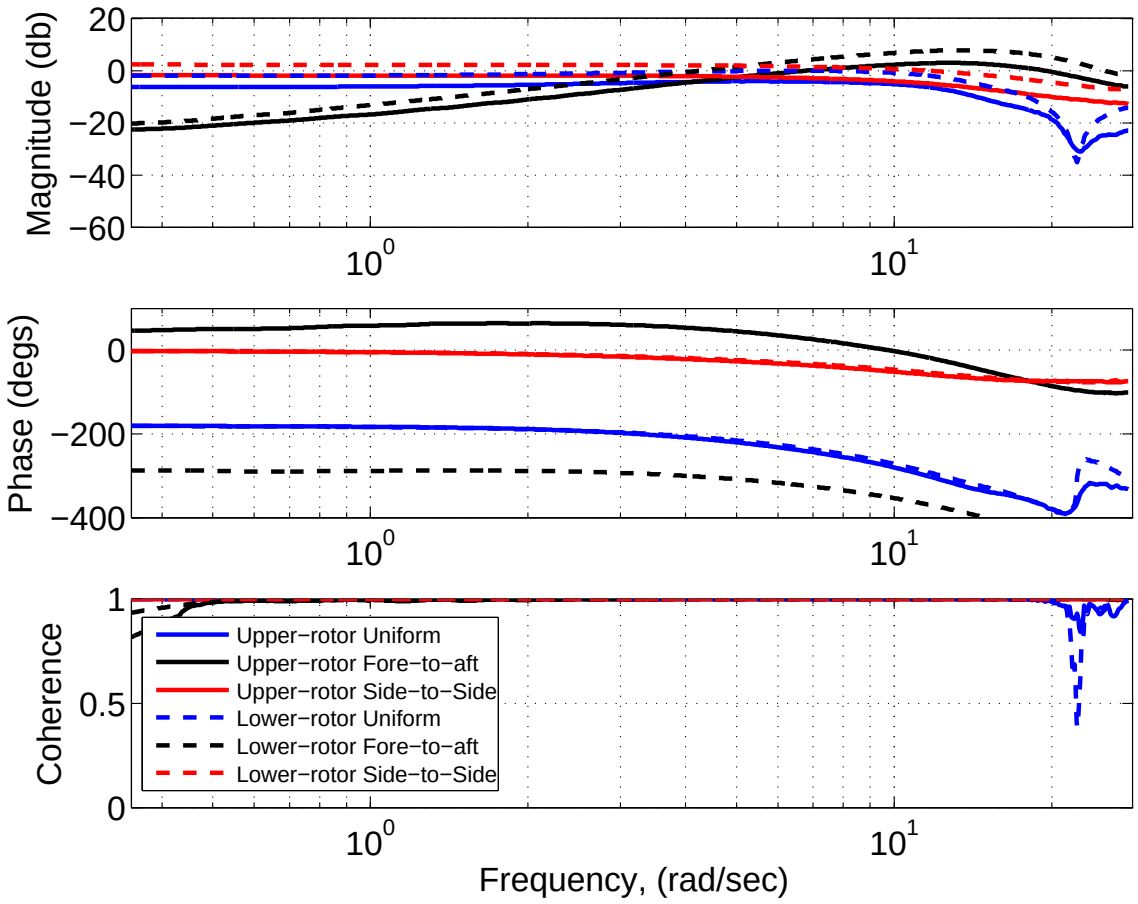

Figure 29: Bode plots of inflow states due to lower rotor fore-to-aft pressure coefficient perturbation in VVPM coaxial rotor model at advance ratio of 0.12

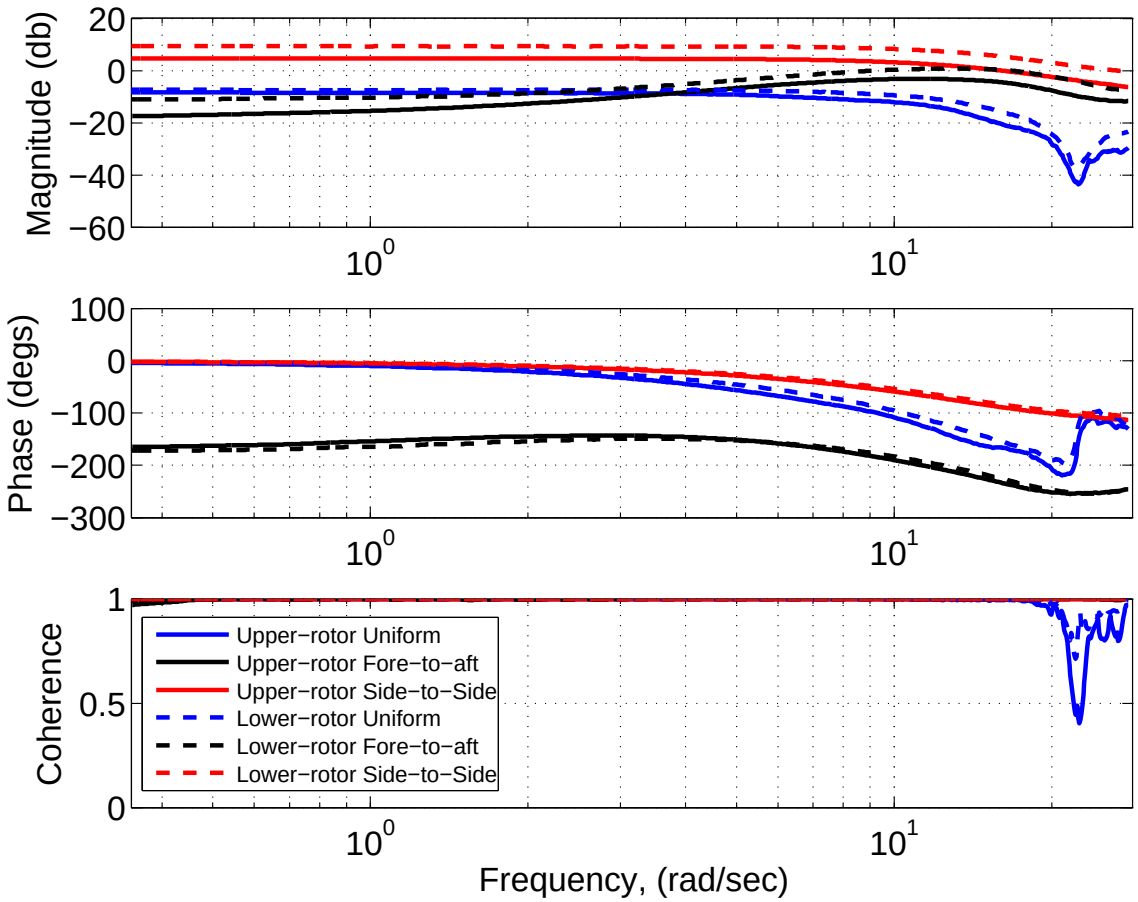

Figure 30: Bode plots of inflow states due to lower rotor side-to-side pressure coefficient perturbation in VVPM coaxial rotor model at advance ratio of 0.12

is that transfer functions corresponding to PPSIM are obtained from a linear model and computation of cost functions due to differences between PPSIM and VVPM frequency responses are meaningful if coherence is close to unity, i.e. all frequency points are equally important. Next, induced inflows that are weakly or not excited by pressure coefficient perturbations may not have much effects on flight dynamics, and therefore are not considered for comparison.

Both original and L-matrix corrected PPSIM frequency responses are compared against VVPM and the cost functions are summarized in Table. 9. The cost functions are computed based on frequency responses between $0.35 \sim 5$ rad/s as this is the region where coherence for VVPM data are above 0.95. Furthermore, low frequency excitation (0.1∼1 rad/s) are important for identification of speed derivatives in flight dynamics analysis [25]. The cost functions are broken down into values due to magnitude and phase differences to provide more insights. Majority of the total cost function corresponding to L-matrix corrected PPSIM shows reduction in value compared to original PPSIM except for a few cases where there are no change or became worst. In cases where total cost functions got worst, i.e. case 4 and 6 in Table. 9, the main reason is an increase in phase cost function. Bode plots corresponding to case 1, 4 and 10 are selected for detailed comparison and analysis.

In Fig. 31 where input is upper rotor uniform pressure coefficient and output is upper uniform inflow states, L-matrix corrected PPSIM magnitude plot matches closely with VVPM compared to the original PPSIM. PPSIM phase plot remains unaffected by L-matrix corrections. Note that L-matrix corrections are computed based on step input results, i.e. zero frequency. As such, some magnitude (and phase) differences between L-matrix corrected PPSIM and VVPM are expected. The main objective here is to show that there is a reduction in magnitude differences by applying the L-matrix corrections, compared to original PPSIM. Differences in frequency responses between original, L-matrix corrected PPSIM and VVPIM are

Table 9: Frequency response differences between original, L-matrix corrected PPSIM and VVPM in hover

Case No.	Input[2]	Output	PPSIM Model	Cost function[1] (0.35 ∼ 5 rad/s) Magnitude	Phase	Total
1	$(\tau_1^{0c})_1$	$(\alpha_1^{0c})_1$	Original	20.7	1.8	22.5
			L-mat corr.	3.6	1.7	5.3
2		$(\alpha_1^{0c})_2$	Original	2.3	0.8	3.0
			L-mat corr.	4.0	6.3	10.2
3	$(\tau_2^{1c})_1$	$(\alpha_2^{1c})_1$	Original	19.8	3.7	23.6
			L-mat corr.	19.6	3.9	23.5
4		$(\alpha_2^{1c})_2$	Original	76.3	13.6	89.9
			L-mat corr.	74.9	31.9	106.8
5	$(\tau_2^{1s})_1$	$(\alpha_2^{1s})_1$	Original	20.6	3.7	24.3
			L-mat corr.	19.9	3.7	23.6
6		$(\alpha_2^{1s})_2$	Original	76.1	13.4	89.5
			L-mat corr.	70.5	29.1	99.6
7	$(\tau_1^{0c})_2$	$(\alpha_1^{0c})_1$	Original	153.8	22.4	176.2
			L-mat corr.	18.8	15.8	34.7
8		$(\alpha_1^{0c})_2$	Original	24.0	9.5	33.5
			L-mat corr.	5.7	6.8	12.5
9	$(\tau_2^{1c})_2$	$(\alpha_2^{1c})_1$	Original	198.0	57.3	255.3
			L-mat corr.	174.2	64.7	238.9
10		$(\alpha_2^{1c})_2$	Original	190.7	8.0	198.7
			L-mat corr.	93.5	19.3	112.8
11	$(\tau_2^{1s})_2$	$(\alpha_2^{1s})_1$	Original	198.2	57.3	255.5
			L-mat corr.	128.7	55.0	183.7
12		$(\alpha_2^{1s})_2$	Original	187.0	8.0	195.1
			L-mat corr.	67.2	15.5	82.7

[1]Computed using Eq. (46)
[2]Bracket subscript '1' and '2' corresponds to upper and lower rotors, respectively

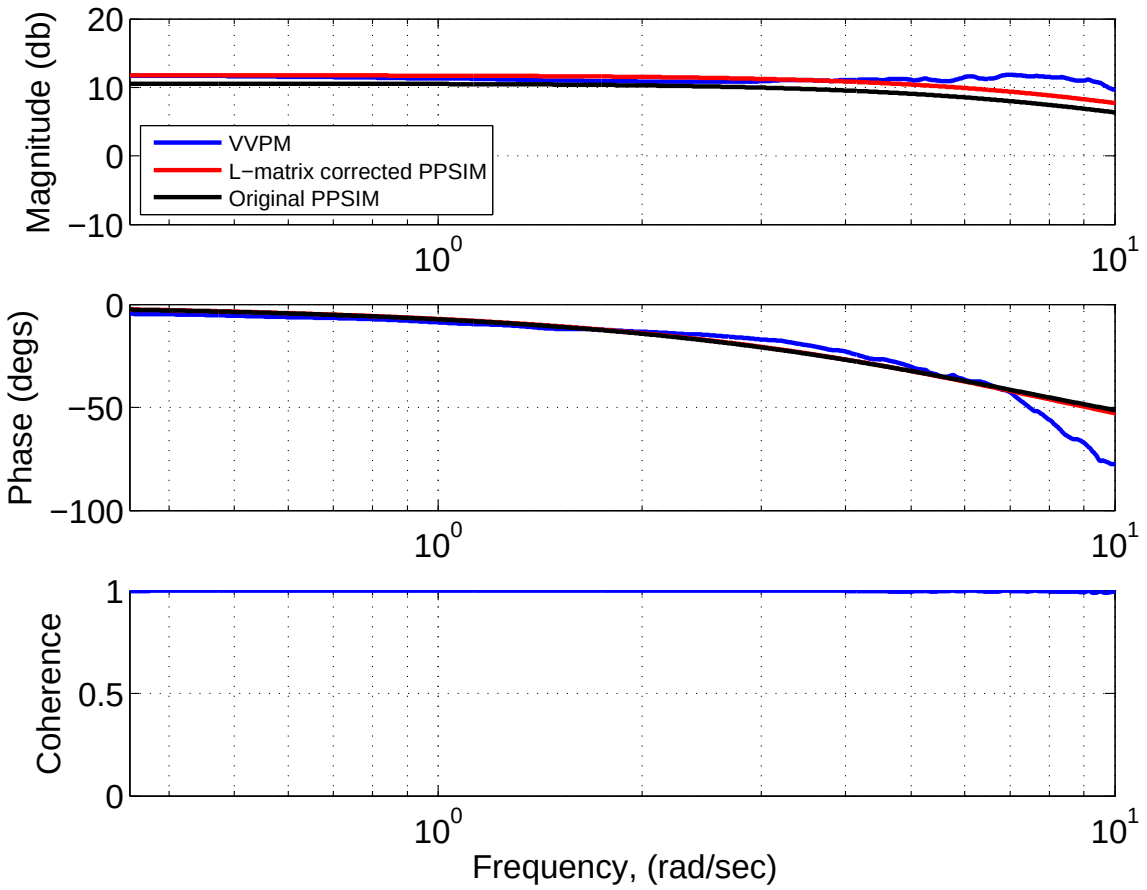

Figure 31: Bode plot comparison between original, L-matrix corrected PPSIM and VVPM for upper rotor uniform inflow states due to upper rotor uniform pressure coefficient perturbation in hover, i.e. case 1 in Table. 9

shown in Fig. 32, with MUAD envelopes superimposed. Note that cost functions due to magnitude (J_{mag}) and phase (J_{phase}) are indicated on the plot for each model for easy reference. Both magnitude and phase differences correspond to L-matrix corrected and original PPSIM fall within the mismatch bounds. In addition, the cost function for each model is less than 50. This means that cost function of 50 or less corresponds to frequency response differences (compared to VVPM) staying within the MUAD envelopes for the range of frequencies considered. In other words, the pilot will not be able to distinguish the dynamic differences between VVPIM or PPSIM over 0.35∼5.0 rad/s due to upper rotor thrust perturbation in hover.

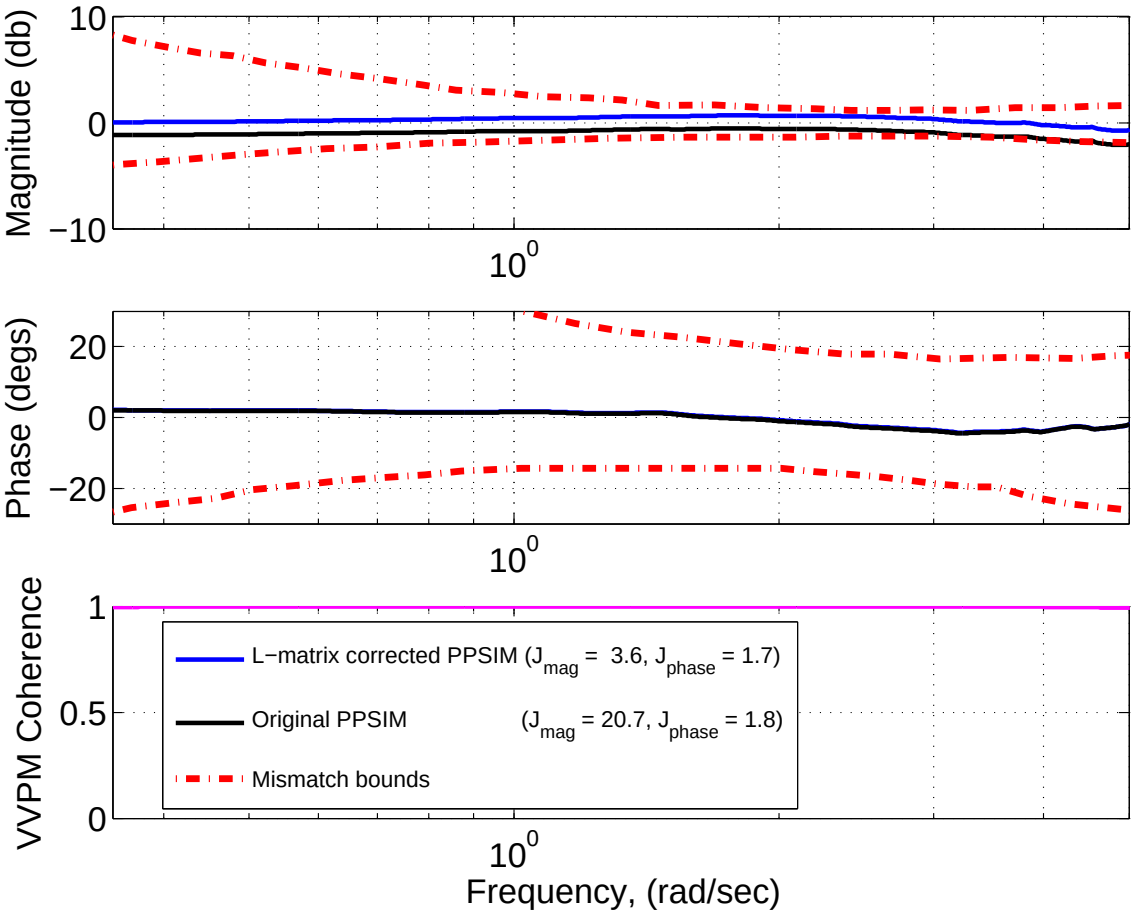

Figure 32: Frequency response differences (0.35∼5.0 rad/s) between original, L-matrix corrected PPSIM and VVPM for case 1 in Table. 9

Next, Bode plots for lower rotor fore-to-aft inflow states due to upper rotor pressure coefficient is examined in Fig. 33. At the frequency range between 0.35∼1.2 rad/s, magnitude plot for L-matrix corrected PPSIM are close to VVPM. After 1.2 rad/s, VVPM magnitude starts to increase before rolling off. As a result, there are considerable magnitude differences between VVPM and L-matrix corrected PPSIM between 1.2∼5.0 rad/s, contributing significantly to the total cost function. Furthermore, some differences in phase between L-matrix corrected PPSIM and VVPM are also observed. Figure 34 shows the corresponding differences in magnitude and phase. For magnitude, both original and L-matrix corrected PPSIM exceeds the mismatch bounds towards the higher frequency range. As such, this result in cost functions exceeding 50 but within the 100 value range. This means that in terms of handling qualities, the pilot will experience slight differences in dynamics between VVPM and PPSIM over 3.0∼5.0 rad/s, which is still satisfactory. For phase difference, the plot corresponding to L-matrix corrected PPSIM are close to the bounds between 1.0∼2.0 rad/s, resulting in higher phase cost function compared to original PPSIM.

In Fig. 35, input is lower rotor fore-to-aft pressure coefficient perturbation and output is lower rotor fore-to-aft inflow state change. L-matrix corrections improve the match in magnitude between PPSIM and VVPM over 1.2∼5.0 rad/s as shown by almost 50% drop in magnitude cost function compared to original PPSIM. Again, slight deterioration in terms of phase performance are observed due to application of L-matrix corrections. From Fig. 36, it is noticed that magnitude differences for original PPSIM lies outside the mismatch bound for most of the frequency range. As such, the cost function is close to 200, twice the acceptable value. For L-matrix corrected PPSIM, only slight violation of the bounds is noticed, resulting in a magnitude cost function of less than 100.

Similar analysis is also performed on coaxial rotor operating at advance ratio of 0.12 where the cost functions are found in Table. 10. Overall, L-matrix corrections

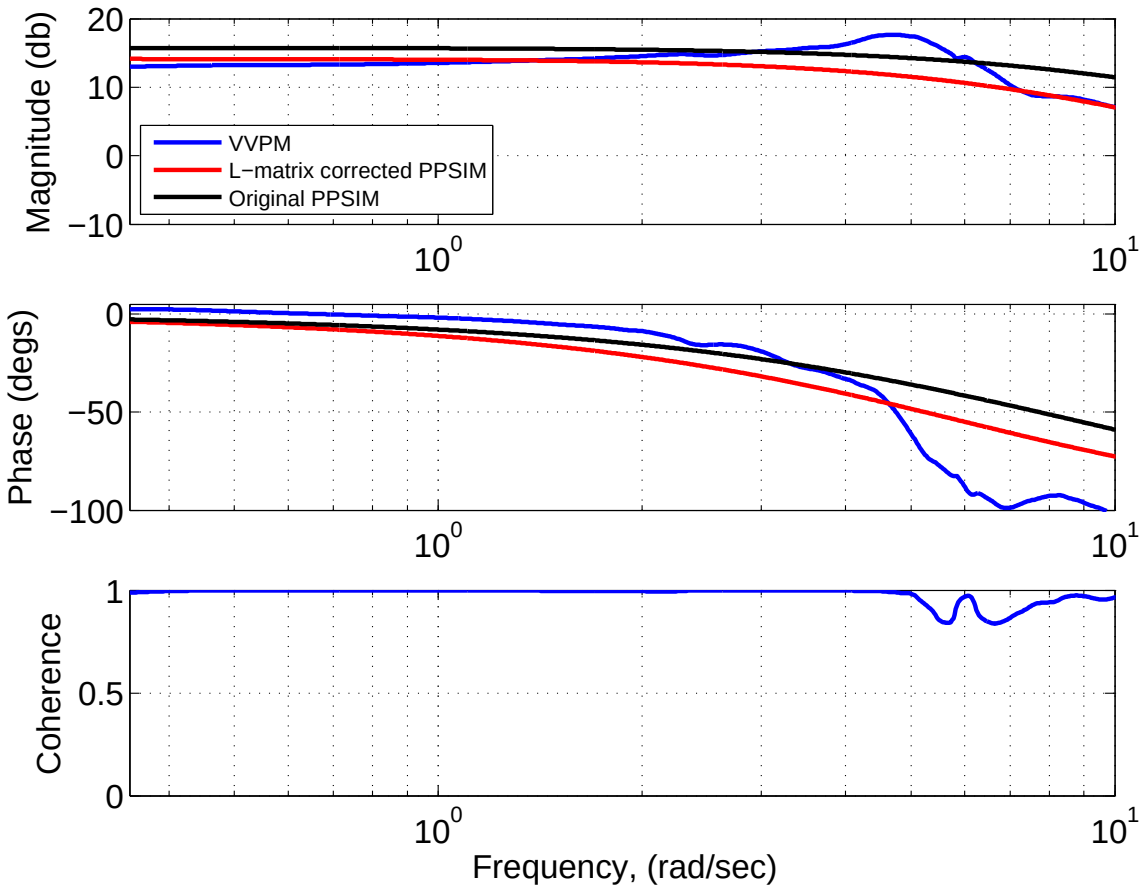

Figure 33: Bode plot comparison between original, L-matrix corrected PPSIM and VVPM for lower rotor fore-to-aft inflow states due to upper rotor fore-to-aft pressure coefficient perturbation in hover, i.e. case 4 in Table. 9

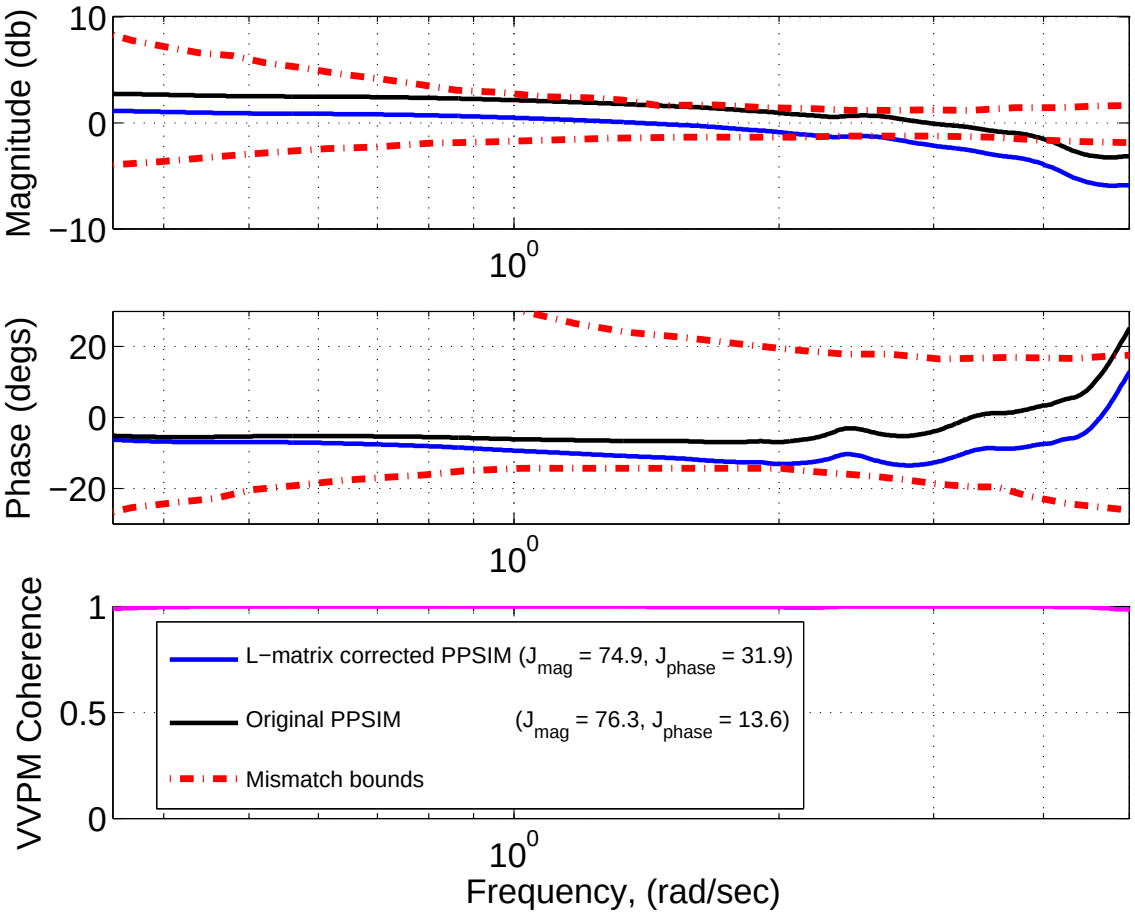

Figure 34: Frequency response differences (0.35∼5.0 rad/s) between original, L-matrix corrected PPSIM and VVPM for case 4 in Table. 9

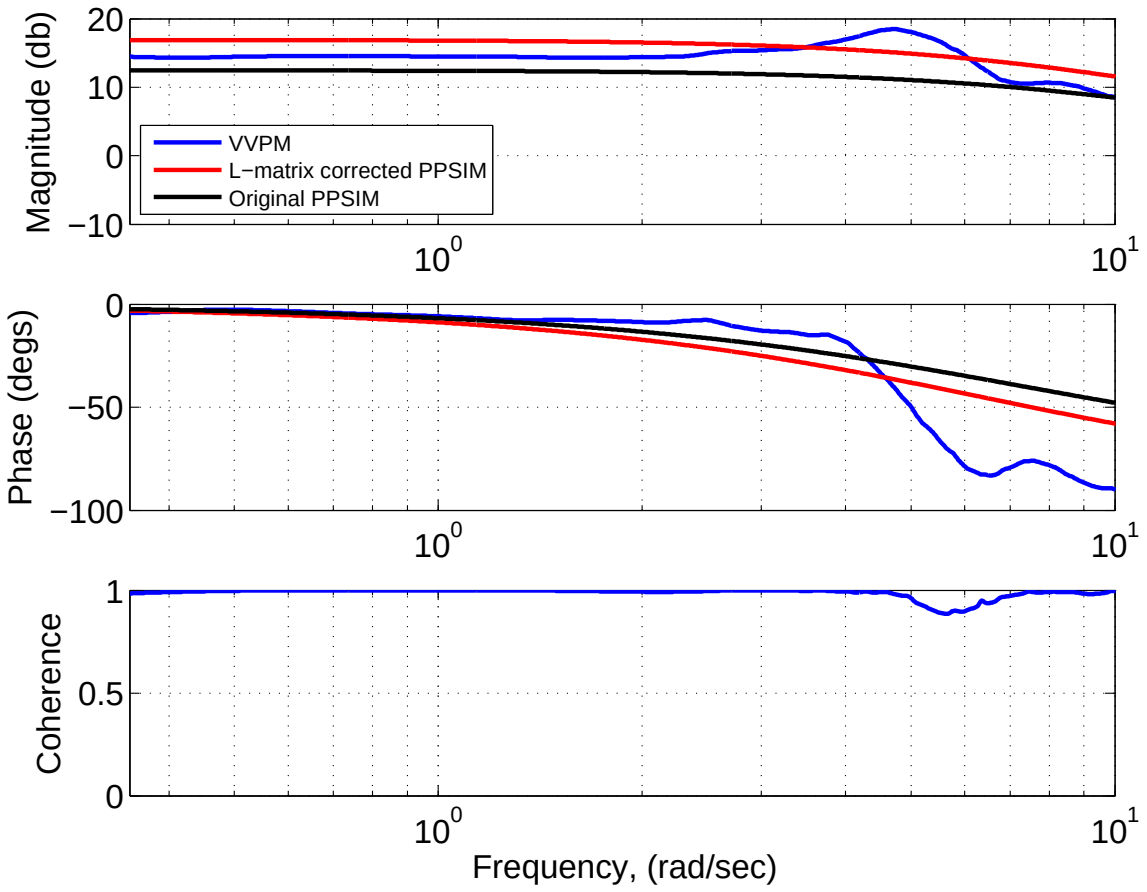

Figure 35: Bode plot comparison between original, L-matrix corrected PPSIM and VVPM for lower rotor fore-to-aft inflow states due to lower rotor fore-to-aft pressure coefficient perturbation in hover, i.e. case 10 in Table. 9

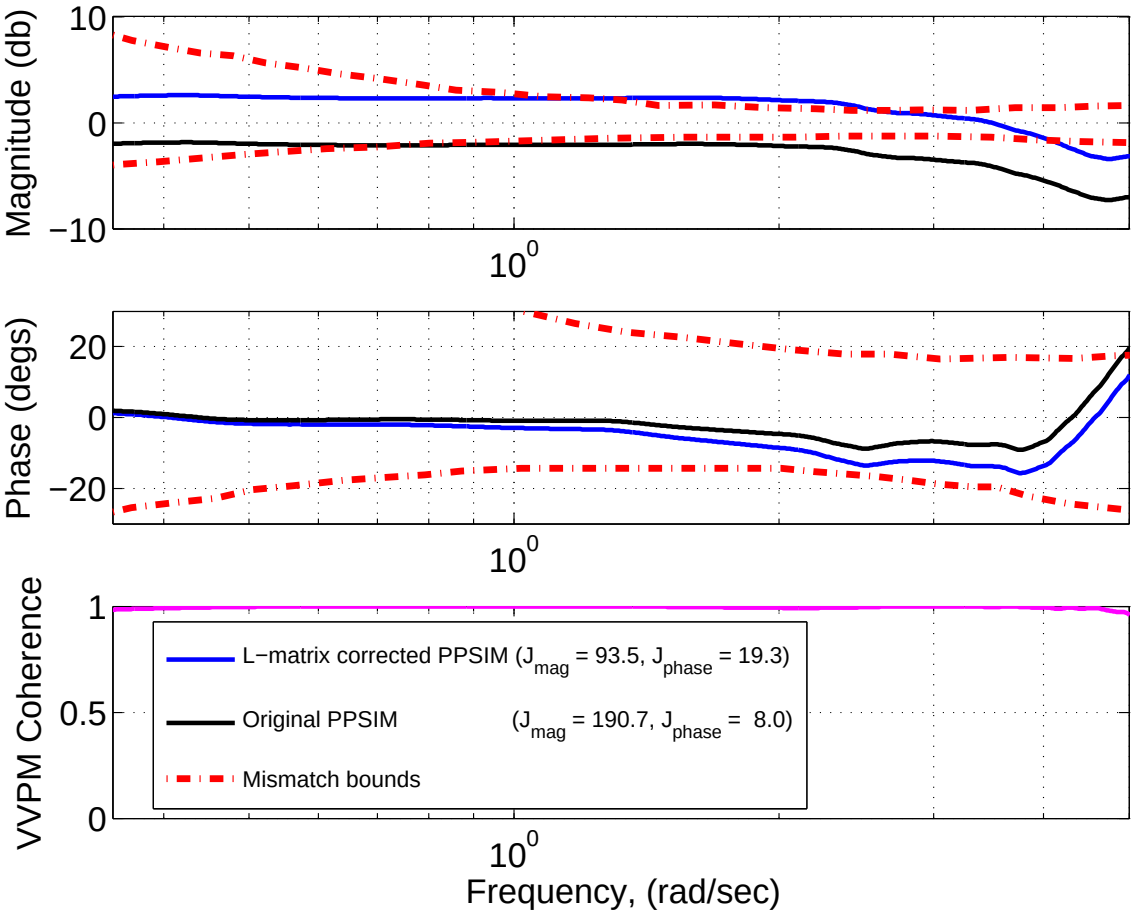

Figure 36: Frequency response differences (0.35∼5.0 rad/s) between original, L-matrix corrected PPSIM and VVPM for case 10 in Table. 9

are effective in reducing magnitude differences between PPSIM and VVPM over a range of frequencies (0.35∼5 rad/s); although in some cases, it also cause a slight increase in phase differences.

Figure 37 shows the Bode plot comparisons corresponding to excitation of lower rotor side-to-side inflow state due to upper rotor side-to-side pressure coefficient perturbation, i.e. case 6 in Table. 10. Clearly, L-matrix corrected PPSIM magnitude plot almost overlap VVPM plot up to 10 rad/s. In terms of phase plot, L-matrix corrected PPSIM is also very close to VVPM values over the same frequency range. This is clearly illustrated in Fig. 38 where both magnitude and phase differences for L-matrix corrected PPSIM lies within the MUAD envelopes over the entire frequency range considered.

Frequency responses for lower rotor fore-to-aft inflow states due to upper rotor uniform pressure coefficient perturbation at advance ratio of 0.12 are shown in Fig. 39. Similarly, magnitude plots for L-matrix corrected PPSIM are very close to that of VVPM. However, this resulted in higher phase differences between L-matrix corrected PPSIM and VVPM as reflected by higher phase cost function compared to original PPSIM. Magnitude differences correspond to original PPSIM are close to the mismatch bound as seen in Fig. 40, resulting in slightly above 50 in terms of magnitude cost function.

Analysis on frequency responses between original, L-matrix corrected PPSIM and VVPM are carried out using both Bode plots and computation of cost functions over the range 0.35∼5.0 rad/s. For cost function below 50, differences in frequency responses lie within the MUAD envelopes. This means that a pilot is not able to distinguish additional dynamics due to mismatch between a higher order model and its lower order equivalence. Cost function between 50 and 100 indicates there are some frequencies where the differences lie outside of the bounds, which is still satisfactory from handling qualities point of view. Above a value of 200 for cost function means

Table 10: Frequency response differences between original, L-matrix corrected PP-SIM and VVPM at advance ratio of 0.12

				Cost function[1] (0.35 $\sim$ 5 rad/s)		
Case No.	Input[2]	Output	PPSIM Model	Magnitude	Phase	Total
1	$(\tau_1^{0c})_1$	$(\alpha_1^{0c})_1$	Original	26.1	2.5	28.6
			L-mat corr.	6.2	1.3	7.5
2		$(\alpha_2^{1c})_1$	Original	0.8	6.5	7.3
			L-mat corr.	0.1	15.5	15.5
3		$(\alpha_1^{0c})_2$	Original	31.9	2.5	34.4
			L-mat corr.	10.7	0.7	11.3
4		$(\alpha_2^{1c})_2$	Original	12.0	5.2	17.3
			L-mat corr.	3.6	7.7	11.2
5	$(\tau_2^{1s})_1$	$(\alpha_2^{1s})_1$	Original	280.5	2.2	282.7
			L-mat corr.	92.5	0.1	92.6
6		$(\alpha_2^{1s})_2$	Original	349.7	10.8	360.5
			L-mat corr.	6.6	0.8	7.4
7	$(\tau_1^{0c})_2$	$(\alpha_1^{0c})_1$	Original	11.5	2.2	13.7
			L-mat corr.	11.8	1.1	12.9
8		$(\alpha_2^{1c})_1$	Original	0.1	4.8	5.0
			L-mat corr.	2.3	7.8	10.1
9		$(\alpha_1^{0c})_2$	Original	6.8	3.2	10.0
			L-mat corr.	12.7	1.3	14.0
10		$(\alpha_2^{1c})_2$	Original	51.9	6.1	58.0
			L-mat corr.	0.4	11.8	12.2
11	$(\tau_2^{1s})_2$	$(\alpha_2^{1s})_1$	Original	237.0	3.7	240.6
			L-mat corr.	191.8	1.7	193.5
12		$(\alpha_2^{1s})_2$	Original	333.9	1.8	338.7
			L-mat corr.	253.7	0.6	254.3

[1]Computed using Eq. (46)
[2]Bracket subscript '1' and '2' corresponds to upper and lower rotors, respectively

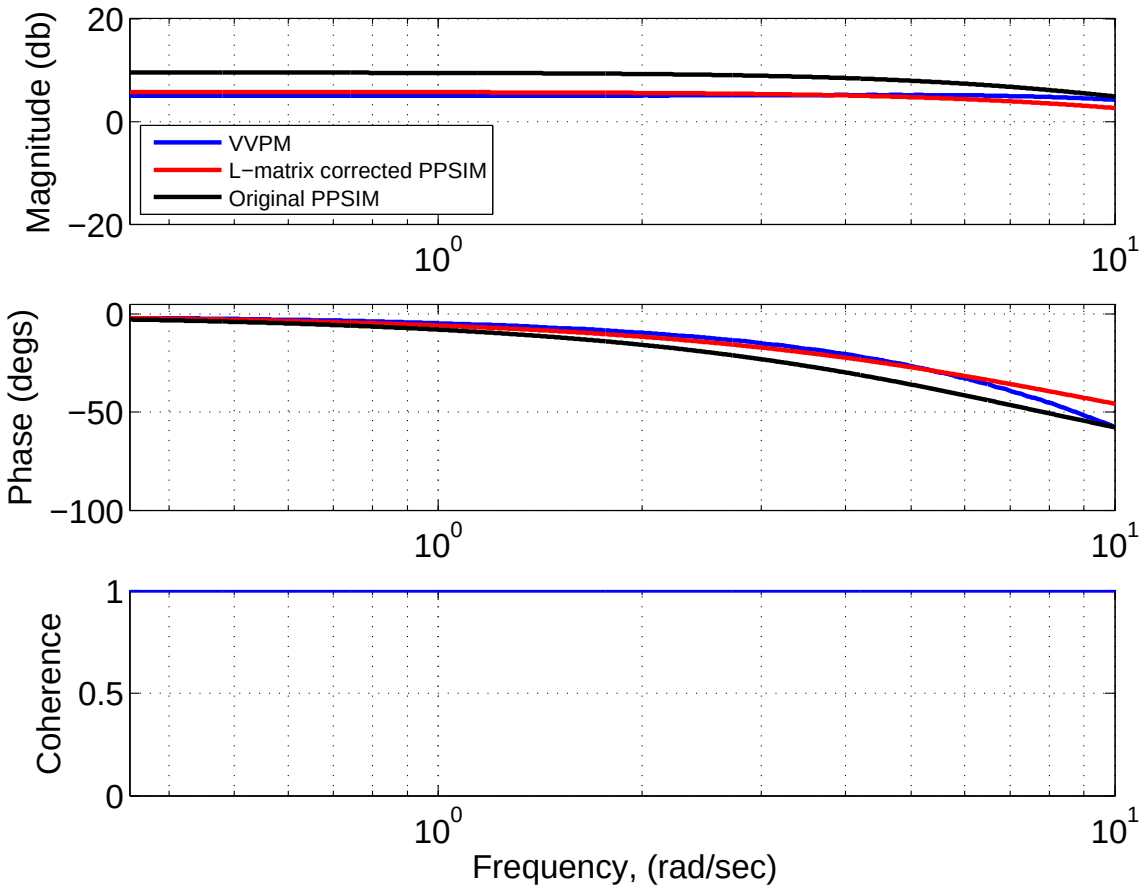

Figure 37: Bode plot comparison between original, L-matrix corrected PPSIM and VVPM for lower rotor side-to-side inflow states due to upper rotor side-to-side pressure coefficient perturbation at advance ratio of 0.12, i.e. case 6 in Table. 10

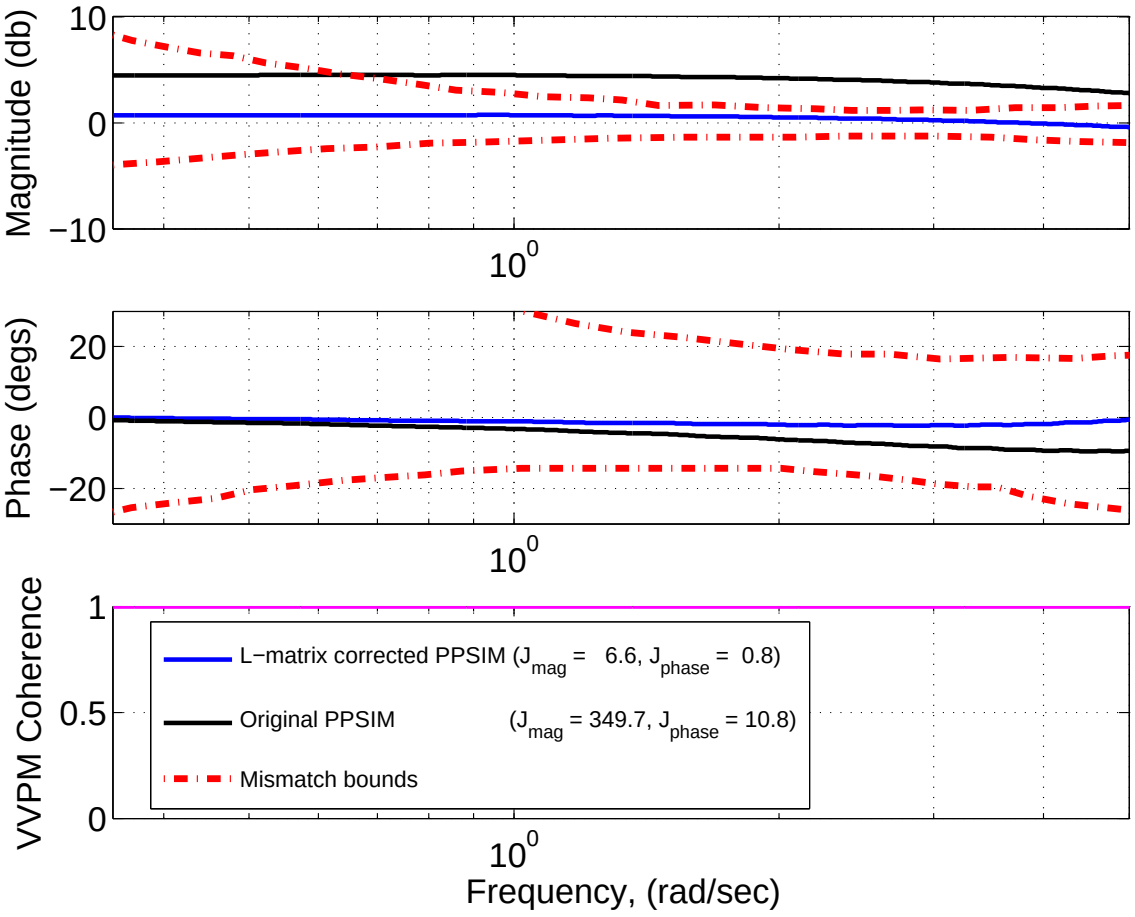

Figure 38: Frequency response differences (0.35∼5.0 rad/s) between original, L-matrix corrected PPSIM and VVPM for case 6 in Table. 10

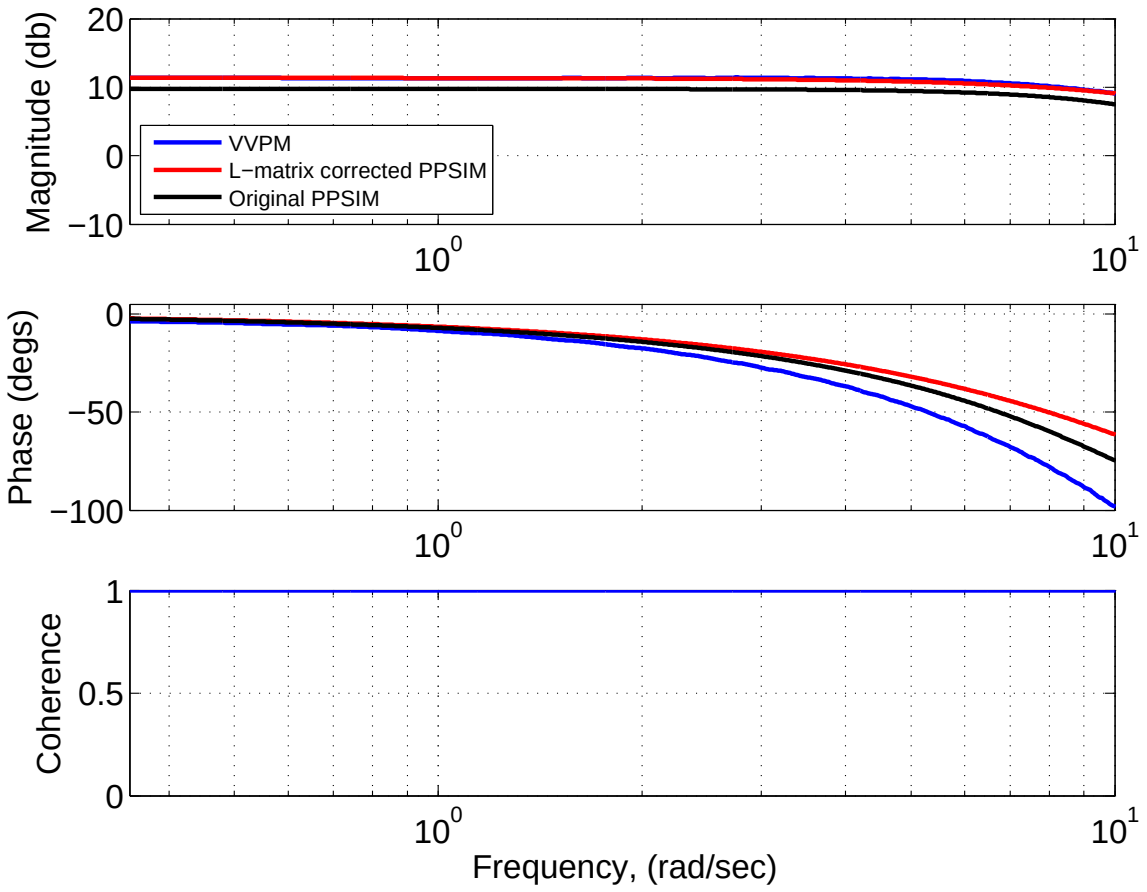

Figure 39: Bode plot comparison between original, L-matrix corrected PPSIM and VVPM for lower rotor fore-to-aft inflow states due to lower rotor uniform pressure coefficient perturbation at advance ratio of 0.12, i.e. case 10 in Table. 10

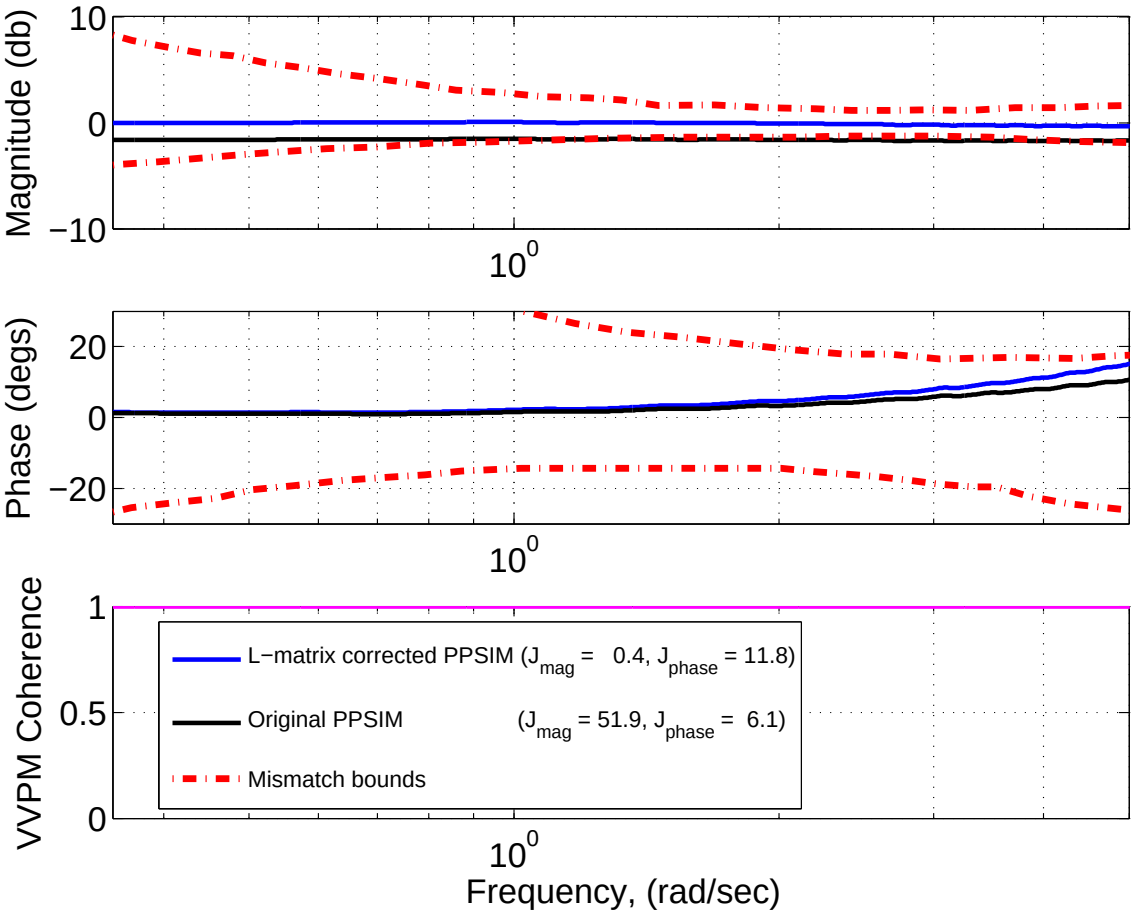

Figure 40: Frequency response differences (0.35∼5.0 rad/s) between original, L-matrix corrected PPSIM and VVPM for case 10 in Table. 10

that frequency response differences are outside of the MUAD envelopes for significant portion of frequency range. This may result in a 1 pilot rating change in the Copper-Harper scale [2].

While the corrections to L-matrix are effective in reducing differences in magnitude between PPSIM and VVPM over frequency range of 0.35∼5 rad/s, it also introduced undesirable phase differences. In order to address this, some elements in PPSIM M-matrix can be modified to improve its phase correlations with VVPM.

CHAPTER VI

MODIFICATIONS TO PPSIM M-MATRIX

In this section, a methodology on improving L-matrix corrected PPISM phase responses with VVPM data is shown. Elements in PPSIM off-diagonal M-matrix blocks are modified to change its phase. Just like rotor-to-rotor steady-state interference are captured in L-matrix off-diagonal blocks, dynamic effects due to presence of other rotors are modeled in $[M_{12}]$ and $[M_{21}]$. The objective is to minimize the cost function (over a frequency range) between L-matrix corrected PPSIM and VVPM by modifying elements in off-diagonal M-matrix blocks.

6.1 Procedures on using CIFER® DERVID

CIFER® *DERVID* identifies parameters in a state-space model by fitting its frequency responses to given frequency response data using the secant optimization algorithm. It also allows selection of parameters to vary during the fitting process while keeping the rest constant. In other words, by re-writing L-matrix corrected PPSIM inflow equation to be of similar form defined in *DERVID*, elements in off-diagonal M-matrix can be modified to reduce its phase differences with VVPM. The procedures are summarized below.

1. Calculate matrix coefficients from L-matrix corrected PPSIM that is compatible with the state-space structure defined in *DERVID*.

2. Input the coefficients into *DERVID* and fixed all parameters, except for elements in off-diagonal M-matrix.

3. Allow the function to run until the solution converges.

Table 11: Modifications to elements in off-diagonal PPSIM M-matrix blocks

Hover					
Elements[1]	New value	Original value	Elements	New value	Original value
$M_{12}(1,1)$	-0.5251	-0.5370	$M_{21}(1,1)$	-0.7538	-0.5370
$M_{12}(2,2)$	-0.3320	-0.2216	$M_{21}(2,2)$	-0.3219	-0.2216
$M_{12}(3,3)$	-0.3556	-0.2216	$M_{21}(3,3)$	-0.3607	-0.2216
Adv. ratio = 0.12					
Elements	New value	Original value	Elements	New value	Original value
$M_{12}(1,1)$	-0.3956	-0.5370	$M_{21}(1,1)$	-0.3757	-0.5370
$M_{12}(2,2)$	-0.0875	-0.2216	$M_{21}(2,2)$	-0.1488	-0.2216
$M_{12}(3,3)$	-0.1765	-0.2216	$M_{21}(3,3)$	-0.1991	-0.2216

[1]First index is row number and second index is column

4. Convert the newly identified elements in off-diagonal M-matrix blocks to same form used in PPSIM.

6.2 Evaluation of improved PPSIM frequency responses

Modifications to off-diagonal M-matrix block elements are summarized in Table. 11, calculated from CIFER® *DERVID* output. Note each M-matrix block in PPSIM is a diagonal 3-by-3 matrix. As seen, the elements are slightly changed to improve L-matrix corrected PPSIM frequency responses match with VVPM data. Also notice that the new elements in $[M_{12}]$ is not the same as $[M_{21}]$ unlike the original case. This reflects the differences between upper and lower rotor pressure coefficients dynamic effects on each other's inflow states; which is reasonable since flow fields on both rotors are not the same. Furthermore, elements associated with cosine and sine parts, i.e. indices (2,2) and (3,3) are close but not the same in the new off-diagonal M-matrix elements. Again, this illustrated the complex coupling effects between upper and lower rotors, which is obviously over-simplified in the original off-diagonal M-matrix elements.

New values of elements in $[M_{12}]$ and $[M_{21}]$ are applied to the L-matrix corrected

PPSIM which is now known as the *improved* PPSIM for evaluation. To avoid cluttering, only cases from Tables. 9 and 10 where phase differences became worst after correcting for L-matrix elements are shown. In addition, significant reduction in phase differences due to modification of off-diagonal M-matrix elements are presented as well. The results are summarized in Table. 12. As seen, total cost function corresponding to improved PPSIM are the smallest among the 3 three PPSIM model considered. Both dynamic and steady-state rotor-to-rotor induced inflow effects are accounted for in the M- and L-matrices, respectively. In some cases, i.e. Table. 9, case 11, modifying elements in off-diagonal M-matrix elements further reduce phase cost function from 55.0 to 9.8. As such, it is shown that the new off-diagonal M-matrix elements are effective in improving L-matrix corrected PPSIM phase responses.

After detailed analysis of dynamic responses from the original, L-matrix corrected and improved PPSIM against VVPM data at different flight conditions, the results are consolidated to give an overall assessment. Similar to steady-state analysis where $\|A\|_2$ is used to represent all inflow state changes corresponding to every pressure coefficient perturbations, an average cost function is computed to evaluate the effectiveness of modifying off-diagonal M-matrix elements. At each advance ratio, cost function corresponding to each input-output frequency response or cases are summed up and a mean value is calculated. The results corresponding to hover as well as advance ratio of 0.07$\sim$0.20 are found in Table. 13.

Among the 3 PPSIM models, the improved version showed the lowest average total cost function for hover, low, medium and high advance ratios. The average magnitude cost functions for improved PPSIM are about 20$\sim$50 % lower than the original PPSIM and the average phase cost functions are reduced compared to L-matrix corrected PPSIM. In other words, the methodology of incorporating L-matrix corrections and modifications to off-diagonal M-matrix elements is effective in improving the coaxial rotor PPSIM frequency as well as steady-state response correlations with VVPM

Table 12: Cost function comparisons between original, L-matrix corrected and improved PPSIM

			Cost function[1] (0.35 ∼ 5 rad/s)		
Table	Case No.	PPSIM Model	Magnitude	Phase	Total
9	4	Original	76.3	13.6	89.9
		L-mat corr.	74.9	31.9	106.8
		Improved[2]	48.2	13.0	61.2
	6	Original	76.1	13.4	89.5
		L-mat corr.	70.5	29.1	99.6
		Improved	48.5	12.9	61.3
	9	Original	198.0	57.3	255.3
		L-mat corr.	174.2	64.7	238.9
		Improved	175.6	12.4	188.0
	10	Original	190.7	8.0	198.7
		L-mat corr.	93.5	19.3	112.8
		Improved	93.7	6.9	100.6
	11	Original	198.2	57.3	255.5
		L-mat corr.	128.7	55.0	183.7
		Improved	121.6	9.8	131.4
	12	Original	187.0	8.0	195.1
		L-mat corr.	67.2	15.5	82.7
		Improved	64.5	6.0	70.5
10	2	Original	0.8	6.5	7.3
		L-mat corr.	0.1	15.5	15.5
		Improved	0.1	0.6	0.6
	4	Original	12.0	5.2	17.3
		L-mat corr.	3.6	7.7	11.2
		Improved	3.9	0.8	4.7
	8	Original	51.9	6.1	58.0
		L-mat corr.	0.4	11.8	12.2
		Improved	1.0	0.2	1.2

[1]Computed using Eq. (46)
[2]L-matrix elements corrected and modifications to off-diagonal M-matrix elements

Table 13: Comparison of average cost functions at different advance ratios

		Average cost function (0.35 $\sim$ 5 rad/s)		
Advance ratio	PPSIM Model	Magnitude	Phase	Total
Hover	Original	97.3	16.6	113.9
	L-mat corr.	56.7	21.2	77.9
	Improved	51.9	7.9	59.8
0.07	Original	89.6	4.9	94.6
	L-mat corr.	73.0	9.6	82.6
	Improved	72.8	6.0	78.8
0.12	Original	112.1	4.3	116.4
	L-mat corr.	49.4	4.2	53.6
	Improved	48.6	2.1	50.7
0.20	Original	150.1	1.0	151.1
	L-mat corr.	25.1	1.0	26.1
	Improved	24.8	0.8	25.6

data. The objectives listed at the beginning of this thesis have been achieved.

CHAPTER VII

CONCLUSION AND RECOMMENDATIONS

For prediction of rotor induced inflows, higher fidelity models such as vorticity-based methods are computational expensive, which may not satisfy real-time requirements in flight simulators. A finite state dynamic inflow model has been developed for multi-rotor configurations from potential flow theory. Its formulation is based on superposition of individual rotor's pressure potential in the flow field and the inflow equation is similar in structure to the Peters-He inflow model. The apparent mass matrix (M-matrix) and influence coefficient matrix (L-matrix) are made up of N-by-N matrix blocks where N is the number of rotors in the configuration. Diagonal blocks accounts for self-induced inflow states due to the rotor pressure coefficients; same as those used in Peters-He inflow model. Rotor-to-rotor interference induced inflows are captured by off-diagonal blocks in the M- and L-matrices. Elements in the off-diagonal blocks are functions of relative separation distances between the rotors. In addition, elements in the L-matrix are functions of the rotor's wake skew angle, calculated using momentum theory. Unlike elements in the diagonal blocks, closed-form solutions for elements in the off-diagonal blocks have not been found. They are computed numerically and stored in lookup table indexed by wake skew functions before use in real-time flight simulations. The multi-rotor dynamic inflow model has been simplified to a coaxial rotor configuration and is known as the coaxial rotor Pressure Potential Superposition Inflow model (coaxial rotor PPSIM). Steady-state and dynamic inflow state responses from coaxial rotor PPSIM are evaluated against higher fidelity models.

7.1 Conclusion

The results presented support the following conclusions:

1. In hover and low advance ratios, steady-state induced inflow results from the Viscous Vortex Particle Method (VVPM) show that cosine-sine couplings are significant but is neglected in coaxial rotor PPSIM.

2. From VVPM data, it is found that effects of lower rotor pressure loading step change on upper rotor induced inflows is weaker than predicted by the coaxial rotor PPSIM.

3. At higher advance ratios, L-matrix extracted from VVPM results are comparable to that of coaxial rotor PPSIM; indicating that the flow fields are behaving more like potential flows.

4. A system identification approach has been developed for capturing real flow effects in the coaxial rotor PPSIM L-matrix. It has been shown to be effective in improving L-matrix corrected PPSIM steady-state inflow state correlations with VVPM data at different flight conditions.

5. Elements in the L-matrix correction terms are insensitive to different upper and lower rotor thrust coefficient ratios. A second order curve-fitted correlations between the corrections and wake skew functions are found for ease of implementation.

6. While comparing frequency responses from the L-matrix corrected PPSIM against VPPM data, it is found that in some cases, the corrections caused phase differences between the two models to increase.

7. Modifications to off-diagonal M-matrix blocks in L-matrix corrected PPSIM are effective in reducing the phase differences at low frequency ranges (0.35∼5 rad/s).

8. The improved PPSIM (with L-matrix corrections and M-matrix modifications) have shown to have closer correlations with VVPM steady-state and dynamic responses over a range of flight conditions, compared to the original coaxial rotor PPSIM.

The main contributions of this thesis are summarized below:

1. Formulated a finite state dynamic inflow model (based on pressure potential superposition) that can be used for any generic rotor configurations.

2. Developed and evaluated a methodology on identifying corrections to the coaxial rotor PPSIM L-matrix, capturing real flow effects such as swirls, wake contractions/distortions and diffusion effects that were neglected in the original formulation.

3. Improved dynamic responses of the finite state coaxial rotor inflow model with higher fidelity model frequency response data at low frequencies range through modification of elements in off-diagonal M-matrix blocks.

7.2 Recommendations

The following is recommended for future work:

1. Extend the finite state multi-rotor dynamic inflow model to other configurations, such as tandem rotors, for use in real-time flight simulators or handling qualities evaluations.

2. Modeling of real flow effects using a viscous decay function or effective wake skew angles in the inflow model and compare the results against the L-matrix corrections identified in this thesis.

3. Study effects of rotor shaft-tilts and side-slips on induced inflow predictions of the multi-rotor inflow model.

4. Implementation of finite state multi-rotor inflow model in real-time flight simulators such as FLIGHTLAB® for pilot-in-the-loop simulations.

APPENDIX A

ELLIPSOIDAL COORDINATE SYSTEM

The ellipsoidal coordinate system, $(\nu, \eta, \bar{\psi})$ is defined as

$$\bar{x} = -\sqrt{1-\nu^2}\sqrt{1+\eta^2}\cos(\bar{\psi}) \tag{A.1}$$

$$\bar{y} = \sqrt{1-\nu^2}\sqrt{1+\eta^2}\sin(\bar{\psi}) \tag{A.2}$$

$$\bar{z} = -\nu\eta \tag{A.3}$$

where the values of $\nu, \eta, \bar{\psi}$ are restricted to the following ranges

$$-1 \leq \nu \leq 1 \tag{A.4}$$

$$0 \leq \eta \leq \infty \tag{A.5}$$

$$0 \leq \bar{\psi} \leq 2\pi \tag{A.6}$$

A sketch of the ellipsodial coordinate system viewed in the $\bar{x} - \bar{z}$ plane in shown in Fig. A.1. The surfaces for ν = constant are hyperboloids while the η = constant surfaces are ellipsoids, both families of surfaces being azimuthally symmetric about the $\bar{z}$ axis. For the special case $\eta = 0$ represents the two faces of the disc, and ν changes sign as one crosses the disc. Lastly, $\bar{\psi}$ is the azimuth angle measure from the negative $\bar{x}$ axis, with counterclockwise direction when viewed along the positive $\bar{z}$ axis. The inverse of Eqs. (A.1) through (A.3) is given as

$$\nu = \frac{-sign(\bar{z})}{\sqrt{2}}\sqrt{(1-\bar{s}) + \sqrt{(1-\bar{s})^2 + 4\bar{z}^2}} \tag{A.7}$$

$$\eta = \frac{1}{\sqrt{2}}\sqrt{(\bar{s}-1) + \sqrt{(\bar{s}-1)^2 + 4\bar{z}^2}} \tag{A.8}$$

$$\bar{\psi} = \tan^{-1}\left(\frac{-\bar{y}}{\bar{x}}\right) \tag{A.9}$$

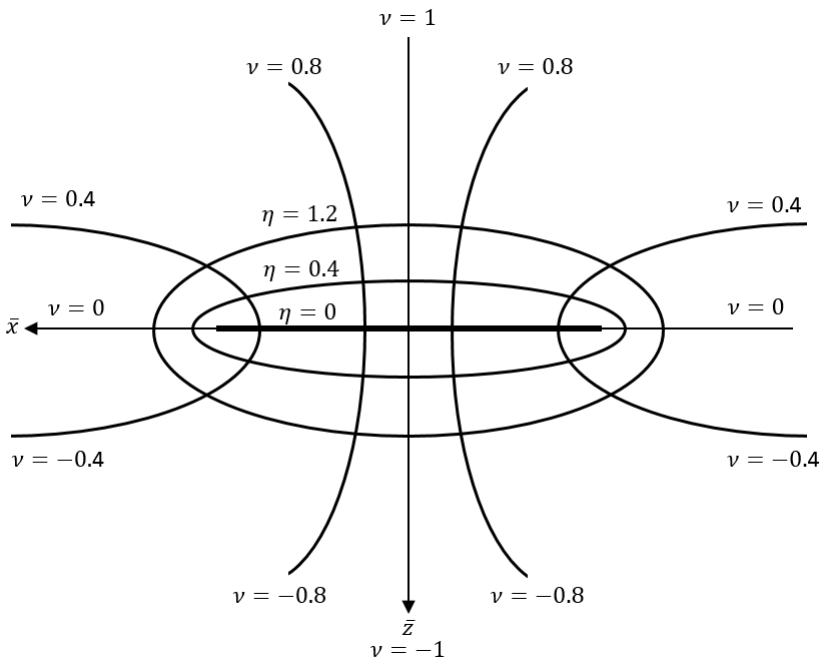

Figure A.1: Ellipsoidal coordinate system

where

$$\bar{s} = \bar{x}^2 + \bar{y}^2 + \bar{z}^2 \tag{A.10}$$

The Laplace's equation, $\vec{\nabla}^2\Phi = 0$ written in ellipsoidal coordinate system takes the form [12]

$$\frac{\partial}{\partial\nu}\left[(1-\nu^2)\frac{\partial\Phi}{\partial\nu}\right] + \frac{\partial}{\partial\eta}\left[(1+\eta^2)\frac{\partial\Phi}{\partial\eta}\right] + \frac{\partial}{\partial\bar{\psi}}\left[\frac{(\nu^2+\eta^2)}{(1-\nu^2)(1+\eta^2)}\frac{\partial\Phi}{\partial\bar{\psi}}\right] = 0 \tag{A.11}$$

Using the method of separation of variables, the solution to Eq. (A.11) is expressed by multiplication of three separated parts, each which are only function of $\nu, \eta, \bar{\psi}$, respectively.

$$\Phi(\nu, \eta, \bar{\psi}) = V(\nu)N(\eta)W(\bar{\psi}) \tag{A.12}$$

By applying Eq. (A.12) to Eq. (A.11), the Laplace equation is separated into the following three equations

$$\frac{d^2W}{d\bar{\psi}^2} + m^2W = 0 \tag{A.13}$$

$$\frac{d}{d\nu}\left[(1-\nu^2)\frac{dV}{d\nu}\right] + \left[-\frac{m^2}{1-\nu^2} + n(n+1)\right]V = 0 \tag{A.14}$$

$$\frac{d}{d\eta}\left[(1+\eta^2)\frac{dN}{d\eta}\right] + \left[\frac{m^2}{1+\eta^2} - n(n+1)\right]N = 0 \tag{A.15}$$

where m and n are the constants of separation, which can be considered as the harmonic number and radial mode number, respectively in dynamic wake analysis. It is clear that Eqs. (A.14) and (A.15) are forms of Legendre's associated differential equations [22]. The general solutions to Eq. (A.14) are $P_n^m(\nu)$ and $Q_n^m(\nu)$, which are the associated Legendre function of the first and second kind, respectively. Similarly, $P_n^m(i\eta)$ and $Q_n^m(i\eta)$ are general solutions to Eq. (A.15).

APPENDIX B

NORMALIZED ASSOCIATED LEGENDRE FUNCTIONS

The normalized associated Legendre functions of the first and second kind are defined as

$$\bar{P}_n^m = (-1)^m \frac{P_n^m(\nu)}{\rho_n^m} \tag{B.1}$$

$$\bar{Q}_n^m = \frac{Q_n^m(i\eta)}{Q_n^m(i0)} \tag{B.2}$$

where

$$(\rho_n^m)^2 = \int_0^1 [P_n^m(\nu)]^2 d\nu = \frac{1}{2n+1}\frac{(n+m)!}{(n-m)!} \tag{B.3}$$

$$Q_n^m(i0) = (-1)^{m+n+1}(i)^{n+1}\frac{(n+m-1)!!}{(n-m)!!}, \quad m+n = odd \tag{B.4}$$

All required values of $\bar{P}_n^m(\nu)$ and $\bar{Q}_n^m(i\eta)$ are computed numerically based on the following recurrence equations

$$\bar{P}_{n+1}^m(\nu) = \sqrt{\frac{(2n+3)(2n+1)}{(n+1)^2-m^2}}\left[\nu\bar{P}_n^m(\nu) - \sqrt{\frac{(n^2-m^2)}{(4n^2-1)}}\bar{P}_{n-1}^m(\nu)\right] \tag{B.5}$$

$$\bar{Q}_{n+1}^m(i\eta) = \frac{(2n+1)}{(n+1-m)} i\frac{\eta Q_n^m(i0)}{Q_{n+1}^m(i0)}\bar{Q}_n^m(i\eta) - \frac{(n+m)}{(n+1-m)}\frac{Q_{n-1}^m(i0)}{Q_{n+1}^m(i0)}\bar{Q}_{n-1}^m(i\eta) \tag{B.6}$$

where

$$\bar{P}_0^0(\nu) = 1 \tag{B.7}$$

$$\bar{P}_1^0(\nu) = \sqrt{3}\nu \tag{B.8}$$

$$\bar{Q}_0^0(i\eta) = \frac{2}{\pi}\tan^{-1}\frac{1}{\eta} \tag{B.9}$$

$$\bar{Q}_1^0(i\eta) = 1 - \eta\tan^{-1}\frac{1}{\eta} \tag{B.10}$$

$$\bar{P}_n^m(\nu) = \sqrt{\frac{(n-m)!}{(n+m)!}}(1-\nu^2)^{\frac{m}{2}}\frac{d^m}{d\nu^m}\bar{P}_n^0(\nu) \tag{B.11}$$

$$\bar{Q}_n^m(i\eta) = \frac{Q_n^0(i0)}{Q_n^m(i0)}(1+\eta^2)^{\frac{m}{2}}\frac{d^m}{d\eta^m}\bar{Q}_n^0(i\eta) \tag{B.12}$$

The derivatives of $\bar{P}_n^m(\nu)$ and $\bar{Q}_n^m(i\eta)$ are given as

$$(1-\nu^2)\frac{d\bar{P}_n^m(\nu)}{d\nu} = (n+m)\frac{\rho_{n-1}^m}{\rho_n^m}\bar{P}_{n-1}^m(\nu) - n\nu\bar{P}_n^m(\nu) \tag{B.13}$$

$$(1+\eta^2)\frac{d\bar{Q}_n^m(i\eta)}{d\eta} = i(n+m)\frac{Q_{n-1}^m(i0)}{Q_n^m(i0)}\bar{Q}_{n-1}^m(i\eta) + n\eta\bar{Q}_n^m(i\eta) \tag{B.14}$$

Finally, the orthogonal property of $\bar{P}_n^m(\nu)$ are given as

$$\int_0^1 \bar{P}_n^m(\nu)\bar{P}_j^m(\nu)d\nu = \delta_n^j \tag{B.15}$$

where both $n+m$ and $j+m$ must be either odd or even.

APPENDIX C

MULTI-ROTOR PPSIM M- AND L-MATRICES

Since calculation of the M- and L-matrices elements involves two rotors, it is appropriate to define the coordinate system used for consistency. As shown in Fig. C.1, the reference coordinate system is located at the 'Receiving' rotor's hub. The 'Active' rotor is located at some distances away from the 'Receiving' rotor along the vertical or Z-axis ($\bar{h}$), longitudinal or X-axis ($\bar{d}$) and lateral or Y-axis ($\bar{l}$) directions, respectively. These distances are normalised with respect to the 'Receiving' rotor radius.

In Eqs. (C.1) through (C.6), the coordinate system corresponding to the 'Receiving' rotor is denoted as 'R' whereas those corresponding to the 'Active' rotor is denoted as 'A'. As an example, elements in $[L_{12}]$ are computed by treating rotor 1 as the 'Receiving' rotor and rotor 2 as the 'Active' rotor. On a similar token, elements in $[L_{21}]$ are computed by treating rotor 2 as the 'Receiving' rotor and rotor 1 as the 'Active' rotor.

By definition, M-matrix is inverse of the E-operator such that $[M] = [E]^{-1}$. Each element in $[E_{RA}]$ is

$$E^{0m}_{jn,\cos} = \frac{1}{2\pi}\int_0^{2\pi}\int_0^1 \nu_R \bar{P}^0_j(\nu_R)\frac{\partial(\bar{P}^m_n(\nu_A)\bar{Q}^m_n(\eta_A)\cos(m\bar{\psi}_A))}{\partial \bar{z}_R} d\nu_R d\bar{\psi}_R \tag{C.1}$$

$$E^{rm}_{jn,\cos} = \frac{1}{\pi}\int_0^{2\pi}\int_0^1 \nu_R \bar{P}^r_j(\nu_R)\cos(r\bar{\psi}_R)\frac{\partial(\bar{P}^m_n(\nu_A)\bar{Q}^m_n(\eta_A)\cos(m\bar{\psi}_A))}{\partial \bar{z}_R} d\nu_R d\bar{\psi}_R \tag{C.2}$$

$$E^{rm}_{jn,\sin} = \frac{1}{\pi}\int_0^{2\pi}\int_0^1 \nu_R \bar{P}^r_j(\nu_R)\sin(r\bar{\psi}_R)\frac{\partial(\bar{P}^m_n(\nu_A)\bar{Q}^m_n(\eta_A)\sin(m\bar{\psi}_A))}{\partial \bar{z}_R} d\nu_R d\bar{\psi}_R \tag{C.3}$$

For elements in $[L_{RA}]$

$$L^{0m}_{jn,\cos} = \frac{1}{2\pi}\int_0^{2\pi}\int_0^1 \nu_R \bar{P}^0_j(\nu_R)\int_0^\infty \frac{\partial(\bar{P}^m_n(\nu_A)\bar{Q}^m_n(\eta_A)\cos(m\bar{\psi}_A))}{\partial \bar{z}_R} d\xi_A d\nu_R d\bar{\psi}_R \tag{C.4}$$

$$L^{rm}_{jn,\cos} = \frac{1}{\pi}\int_0^{2\pi}\int_0^1 \nu_R \bar{P}^r_j(\nu_R)\cos(r\bar{\psi}_R)\int_0^\infty \frac{\partial(\bar{P}^m_n(\nu_A)\bar{Q}^m_n(\eta_A)\cos(m\bar{\psi}_A))}{\partial \bar{z}_R} d\xi_A d\nu_R d\bar{\psi}_R \tag{C.5}$$

$$L^{rm}_{jn,\sin} = \frac{1}{\pi}\int_0^{2\pi}\int_0^1 \nu_R \bar{P}^r_j(\nu_R)\sin(r\bar{\psi}_R)\int_0^\infty \frac{\partial(\bar{P}^m_n(\nu_A)\bar{Q}^m_n(\eta_A)\sin(m\bar{\psi}_A))}{\partial \bar{z}_R} d\xi_A d\nu_R d\bar{\psi}_R \tag{C.6}$$

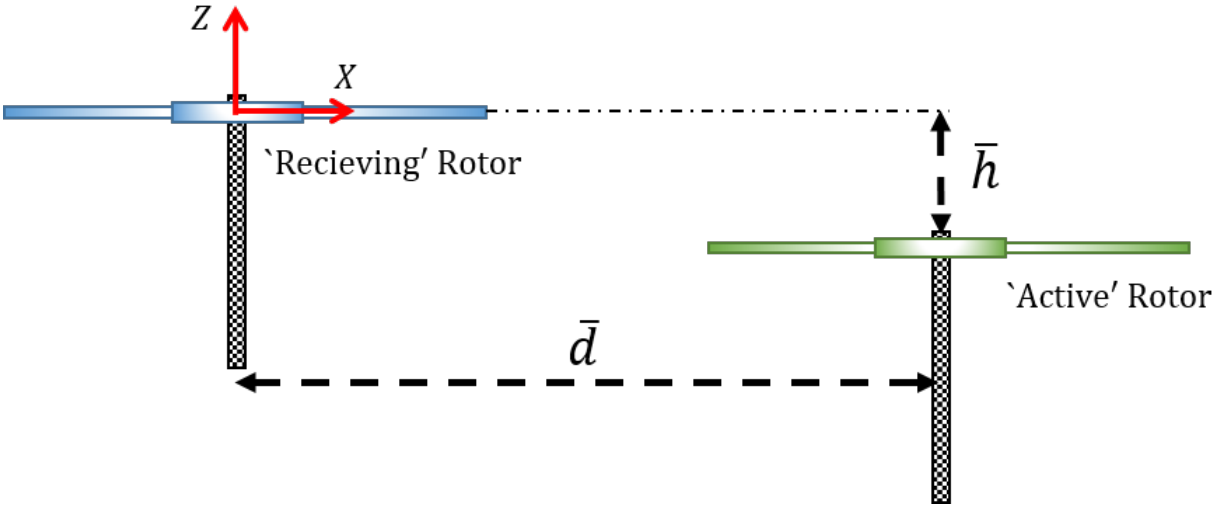

(a) Side view

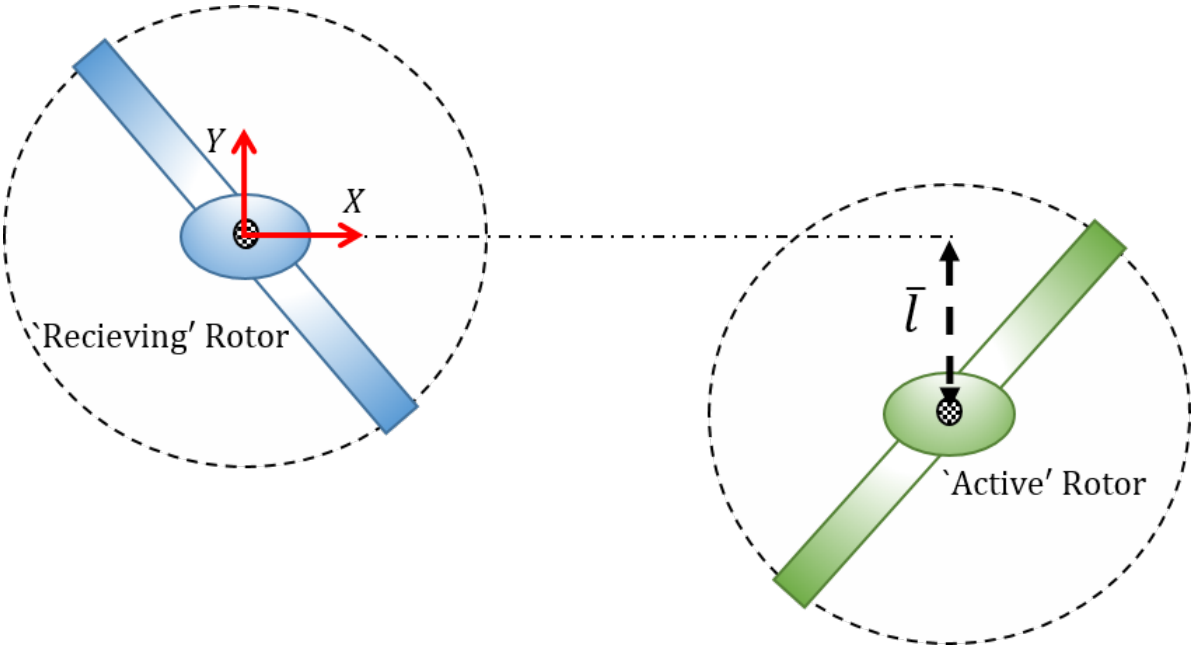

(b) Top view

Figure C.1: Coordinate system used to compute elements in multi-rotor PPSIM M- and L-matrices

APPENDIX D

COAXIAL ROTOR PPSIM M- AND L-MATRICES

The inflow equation corresponding to coaxial rotor PPSIM is given as

$$\begin{bmatrix} M_{11} & M_{12} \\ M_{21} & M_{22} \end{bmatrix} \begin{Bmatrix} \overset{*}{\alpha}_1 \\ \overset{*}{\alpha}_2 \end{Bmatrix} + \begin{bmatrix} V_{m1} & 0 \\ 0 & V_{m2} \end{bmatrix} \begin{bmatrix} L_{11} & L_{12} \\ L_{21} & L_{22} \end{bmatrix}^{-1} \begin{Bmatrix} \alpha_1 \\ \alpha_2 \end{Bmatrix} = \begin{Bmatrix} \tau_1/2 \\ \tau_2/2 \end{Bmatrix} \tag{D.1}$$

where

$$\begin{bmatrix} M_{11} & M_{12} \\ M_{21} & M_{22} \end{bmatrix} := \begin{bmatrix} E_{11} & E_{12} \\ E_{21} & E_{22} \end{bmatrix}^{-1} \tag{D.2}$$

Each element in the E-matrix blocks are computed using Eqs. (D.3) through (D.14).

For $[E_{11}]$,

$$E^{0m}_{jn,\cos} = \frac{1}{2\pi}\int_0^{2\pi}\int_0^1 \nu_1 \bar{P}^0_j(\nu_1)\frac{\partial(\bar{P}^m_n(\nu_1)\bar{Q}^m_n(i\eta_1)\cos(m\bar{\psi}_1))}{\partial z_1}d\nu_1 d\bar{\psi}_1 \tag{D.3}$$

$$E^{rm}_{jn,\cos} = \frac{1}{\pi}\int_0^{2\pi}\int_0^1 \nu_1 \bar{P}^r_j(\nu_1)\cos(r\bar{\psi}_1)\frac{\partial(\bar{P}^m_n(\nu_1)\bar{Q}^m_n(i\eta_1)\cos(m\bar{\psi}_1))}{\partial z_1}d\nu_1 d\bar{\psi}_1 \tag{D.4}$$

$$E^{rm}_{jn,\sin} = \frac{1}{\pi}\int_0^{2\pi}\int_0^1 \nu_1 \bar{P}^r_j(\nu_1)\sin(r\bar{\psi}_1)\frac{\partial(\bar{P}^m_n(\nu_1)\bar{Q}^m_n(i\eta_1)\sin(m\bar{\psi}_1))}{\partial z_1}d\nu_1 d\bar{\psi}_1 \tag{D.5}$$

For $[E_{12}]$,

$$E^{0m}_{jn,\cos} = \frac{1}{2\pi}\int_0^{2\pi}\int_0^1 \nu_1 \bar{P}^0_j(\nu_1)\frac{\partial(\bar{P}^m_n(\nu_2)\bar{Q}^m_n(i\eta_2)\cos(m\bar{\psi}_2))}{\partial z_1}d\nu_1 d\bar{\psi}_1 \tag{D.6}$$

$$E^{rm}_{jn,\cos} = \frac{1}{\pi}\int_0^{2\pi}\int_0^1 \nu_1 \bar{P}^r_j(\nu_1)\cos(r\bar{\psi}_1)\frac{\partial(\bar{P}^m_n(\nu_2)\bar{Q}^m_n(i\eta_2)\cos(m\bar{\psi}_2))}{\partial z_1}d\nu_1 d\bar{\psi}_1 \tag{D.7}$$

$$E^{rm}_{jn,\sin} = \frac{1}{\pi}\int_0^{2\pi}\int_0^1 \nu_1 \bar{P}^r_j(\nu_1)\sin(r\bar{\psi}_1)\frac{\partial(\bar{P}^m_n(\nu_2)\bar{Q}^m_n(i\eta_2)\sin(m\bar{\psi}_2))}{\partial z_1}d\nu_1 d\bar{\psi}_1 \tag{D.8}$$

For $[E_{22}]$,

$$E^{0m}_{jn,\cos} = \frac{1}{2\pi}\int_0^{2\pi}\int_0^1 \nu_2 \bar{P}^0_j(\nu_2)\frac{\partial(\bar{P}^m_n(\nu_2)\bar{Q}^m_n(i\eta_2)\cos(m\bar{\psi}_2))}{\partial z_2}d\nu_2 d\bar{\psi}_2 \tag{D.9}$$

$$E^{rm}_{jn,\cos} = \frac{1}{\pi}\int_0^{2\pi}\int_0^1 \nu_2 \bar{P}^r_j(\nu_2)\cos(r\bar{\psi}_2)\frac{\partial(\bar{P}^m_n(\nu_2)\bar{Q}^m_n(i\eta_2)\cos(m\bar{\psi}_2))}{\partial z_2}d\nu_2 d\bar{\psi}_2 \tag{D.10}$$

$$E^{rm}_{jn,\sin} = \frac{1}{\pi}\int_0^{2\pi}\int_0^1 \nu_2 \bar{P}^r_j(\nu_2)\sin(r\bar{\psi}_2)\frac{\partial(\bar{P}^m_n(\nu_2)\bar{Q}^m_n(i\eta_2)\sin(m\bar{\psi}_2))}{\partial z_2}d\nu_2 d\bar{\psi}_2 \tag{D.11}$$

For $[E_{21}]$,

$$E^{0m}_{jn,\cos} = \frac{1}{2\pi}\int_0^{2\pi}\int_0^1 \nu_2 \bar{P}^0_j(\nu_2)\frac{\partial(\bar{P}^m_n(\nu_1)\bar{Q}^m_n(i\eta_1)\cos(m\bar{\psi}_1))}{\partial z_2}d\nu_2 d\bar{\psi}_2 \tag{D.12}$$

$$E^{rm}_{jn,\cos} = \frac{1}{\pi}\int_0^{2\pi}\int_0^1 \nu_2 \bar{P}^r_j(\nu_2)\cos(r\bar{\psi}_2)\frac{\partial(\bar{P}^m_n(\nu_1)\bar{Q}^m_n(i\eta_1)\cos(m\bar{\psi}_1))}{\partial z_2}d\nu_2 d\bar{\psi}_2 \tag{D.13}$$

$$E^{rm}_{jn,\sin} = \frac{1}{\pi}\int_0^{2\pi}\int_0^1 \nu_2 \bar{P}^r_j(\nu_2)\sin(r\bar{\psi}_2)\frac{\partial(\bar{P}^m_n(\nu_1)\bar{Q}^m_n(i\eta_1)\sin(m\bar{\psi}_1))}{\partial z_2}d\nu_2 d\bar{\psi}_2 \tag{D.14}$$

Notice that for $[E_{11}]$ and $[E_{22}]$, the equations are similar to those in Peters-He inflow model [31] where closed-form solutions have been found. On the other hand, elements in $[E_{12}]$ and $[E_{21}]$ have to be numerically calculated before use in real-time flight simulations.

Next, the elements in the L-matrix are computed from Eqs. (D.15) through (D.26).

For $[L_{11}]$,

$$L^{0m}_{jn,\cos} = \frac{1}{2\pi}\int_0^{2\pi}\int_0^1 \nu_1 \bar{P}^0_j(\nu_1)\int_0^\infty \frac{\partial(\bar{P}^m_n(\nu_1)\bar{Q}^m_n(i\eta_1)\cos(m\bar{\psi}_1))}{\partial z_1}d\xi_1 d\nu_1 d\bar{\psi}_1 \tag{D.15}$$

$$L^{rm}_{jn,\cos} = \frac{1}{\pi}\int_0^{2\pi}\int_0^1 \nu_1 \bar{P}^r_j(\nu_1)\cos(r\bar{\psi}_1)\int_0^\infty \frac{\partial(\bar{P}^m_n(\nu_1)\bar{Q}^m_n(i\eta_1)\cos(m\bar{\psi}_1))}{\partial z_1}d\xi_1 d\nu_1 d\bar{\psi}_1 \tag{D.16}$$

$$L^{rm}_{jn,\sin} = \frac{1}{\pi}\int_0^{2\pi}\int_0^1 \nu_1 \bar{P}^r_j(\nu_1)\sin(r\bar{\psi}_1)\int_0^\infty \frac{\partial(\bar{P}^m_n(\nu_1)\bar{Q}^m_n(i\eta_1)\sin(m\bar{\psi}_1))}{\partial z_1}d\xi_1 d\nu_1 d\bar{\psi}_1 \tag{D.17}$$

For $[L_{12}]$,

$$L^{0m}_{jn,\cos} = \frac{1}{2\pi}\int_0^{2\pi}\int_0^1 \nu_1 \bar{P}^0_j(\nu_1)\int_0^\infty \frac{\partial(\bar{P}^m_n(\nu_2)\bar{Q}^m_n(i\eta_2)\cos(m\bar{\psi}_2))}{\partial z_1} d\xi_2 d\nu_1 d\bar{\psi}_1 \tag{D.18}$$

$$L^{rm}_{jn,\cos} = \frac{1}{\pi}\int_0^{2\pi}\int_0^1 \nu_1 \bar{P}^r_j(\nu_1)\cos(r\bar{\psi}_1)\int_0^\infty \frac{\partial(\bar{P}^m_n(\nu_2)\bar{Q}^m_n(i\eta_2)\cos(m\bar{\psi}_2))}{\partial z_1} d\xi_2 d\nu_1 d\bar{\psi}_1 \tag{D.19}$$

$$L^{rm}_{jn,\sin} = \frac{1}{\pi}\int_0^{2\pi}\int_0^1 \nu_1 \bar{P}^r_j(\nu_1)\sin(r\bar{\psi}_1)\int_0^\infty \frac{\partial(\bar{P}^m_n(\nu_2)\bar{Q}^m_n(i\eta_2)\sin(m\bar{\psi}_2))}{\partial z_1} d\xi_2 d\nu_1 d\bar{\psi}_1 \tag{D.20}$$

For $[L_{22}]$,

$$L^{0m}_{jn,\cos} = \frac{1}{2\pi}\int_0^{2\pi}\int_0^1 \nu_2 \bar{P}^0_j(\nu_2)\int_0^\infty \frac{\partial(\bar{P}^m_n(\nu_2)\bar{Q}^m_n(i\eta_2)\cos(m\bar{\psi}_2))}{\partial z_2} d\xi_2 d\nu_2 d\bar{\psi}_2 \tag{D.21}$$

$$L^{rm}_{jn,\cos} = \frac{1}{\pi}\int_0^{2\pi}\int_0^1 \nu_2 \bar{P}^r_j(\nu_2)\cos(r\bar{\psi}_2)\int_0^\infty \frac{\partial(\bar{P}^m_n(\nu_2)\bar{Q}^m_n(i\eta_2)\cos(m\bar{\psi}_2))}{\partial z_2} d\xi_2 d\nu_2 d\bar{\psi}_2 \tag{D.22}$$

$$L^{rm}_{jn,\sin} = \frac{1}{\pi}\int_0^{2\pi}\int_0^1 \nu_2 \bar{P}^r_j(\nu_2)\sin(r\bar{\psi}_2)\int_0^\infty \frac{\partial(\bar{P}^m_n(\nu_2)\bar{Q}^m_n(i\eta_2)\sin(m\bar{\psi}_2))}{\partial z_2} d\xi_2 d\nu_2 d\bar{\psi}_2 \tag{D.23}$$

For $[L_{21}]$,

$$L^{0m}_{jn,\cos} = \frac{1}{2\pi}\int_0^{2\pi}\int_0^1 \nu_2 \bar{P}^0_j(\nu_2)\int_0^\infty \frac{\partial(\bar{P}^m_n(\nu_1)\bar{Q}^m_n(i\eta_1)\cos(m\bar{\psi}_1))}{\partial z_2} d\xi_1 d\nu_2 d\bar{\psi}_2 \tag{D.24}$$

$$L^{rm}_{jn,\cos} = \frac{1}{\pi}\int_0^{2\pi}\int_0^1 \nu_2 \bar{P}^r_j(\nu_2)\cos(r\bar{\psi}_2)\int_0^\infty \frac{\partial(\bar{P}^m_n(\nu_1)\bar{Q}^m_n(i\eta_1)\cos(m\bar{\psi}_1))}{\partial z_2} d\xi_1 d\nu_2 d\bar{\psi}_2 \tag{D.25}$$

$$L^{rm}_{jn,\sin} = \frac{1}{\pi}\int_0^{2\pi}\int_0^1 \nu_2 \bar{P}^r_j(\nu_2)\sin(r\bar{\psi}_2)\int_0^\infty \frac{\partial(\bar{P}^m_n(\nu_1)\bar{Q}^m_n(i\eta_1)\sin(m\bar{\psi}_1))}{\partial z_2} d\xi_1 d\nu_2 d\bar{\psi}_2 \tag{D.26}$$

Similarly, closed-form solutions corresponding to $[L_{11}]$ and $[L_{22}]$ have been found in Peters-He inflow model, while elements in $[L_{12}]$ and $[L_{21}]$ are precomputed numerically and stored in a lookup table indexed by wake skew function, $\mathrm{X_{skew}} = \tan\frac{\chi_{\mathrm{mom}}}{2}$. Numerical results for three-state coaxial rotor PPSIM $[L_{21}]$ corresponding to different rotors separation distance (normalised by rotor radius) at various upper rotor $\mathrm{X_{skew}}$

are shown in Fig. D.1. Elements in $[L_{21}]$ relates upper rotor pressure coefficients on the lower rotor inflow states under steady-state condition. An interesting thing to note is that even at separation distance of 10 rotor radius ($\bar{h} = 10$) between both rotors at very low advance ratios, upper rotor wake effects still have considerable influences on the lower rotor. This is because PPSIM is formulated based on potential flow assumption where viscous effects are neglected. Hence, the flow does not dissipate but continue to propagate downstream onto the lower rotor. However, as wake skew angle increases, upper rotor wake is skewed downstream which reduces its impingement area onto lower rotor disk. This effect can be seen clearly for the case of $\bar{h} = 10$ where the elements stay close to zero for most of $\mathrm{X_{skew}}$.

Figure. D.2 shows the variations of elements in $[L_{12}]$ with different lower rotor $\mathrm{X_{skew}}$. Here, $[L_{12}]$ relates upper rotor inflow states due to the lower rotor pressure coefficients. Unlike the previous case, effect of lower rotor wake on upper rotor inflow is very small. This is expected since the wake are washed downstream with minimal interaction with upper rotor disk. Notice that at higher separation distance of 1.5 and 10 rotor radius, there is almost no interference effects on the upper rotor.

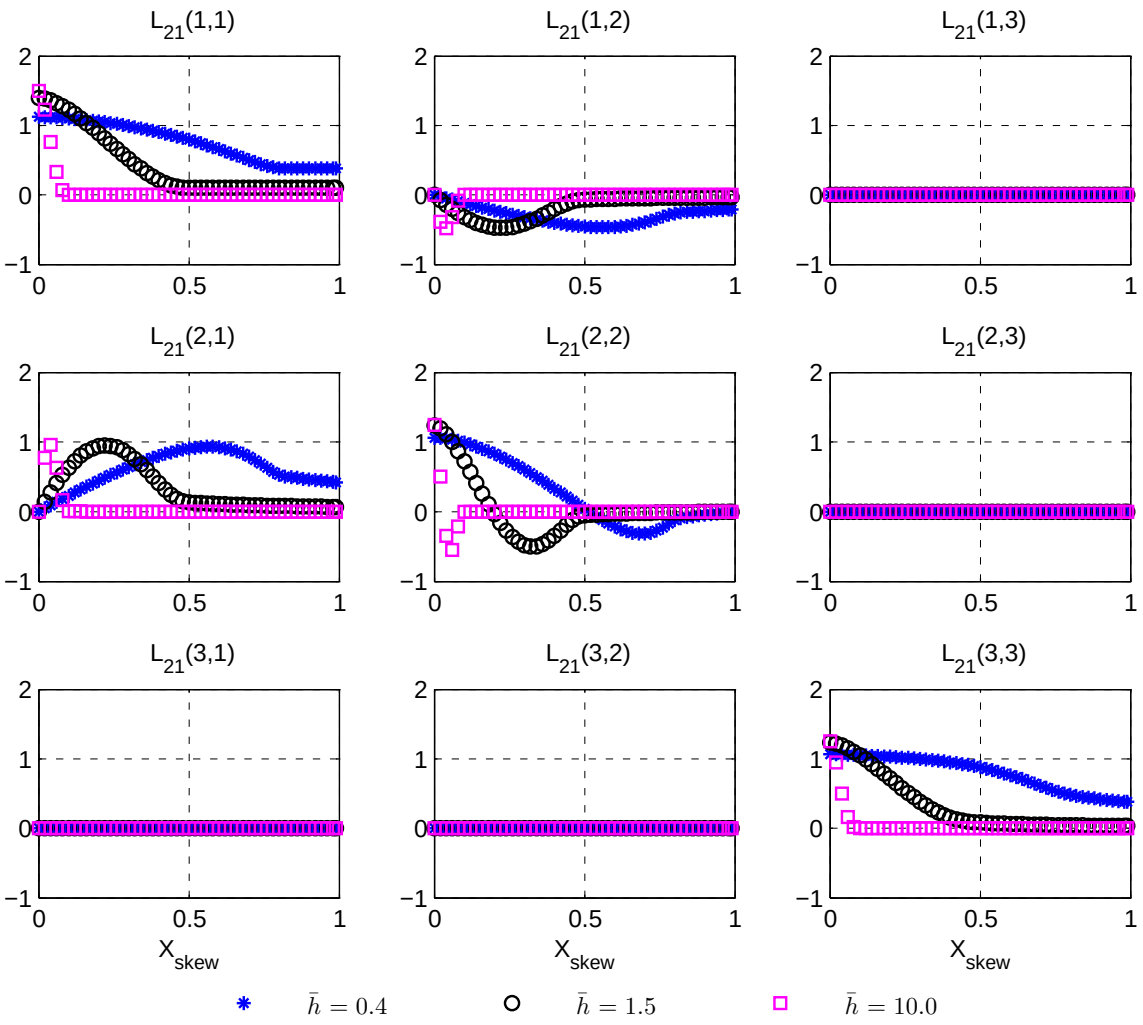

Figure D.1: Precalculated elements in three-state coaxial rotor PPSIM $[L_{21}]$ corresponding to different rotors separation distances, $\bar{h}$

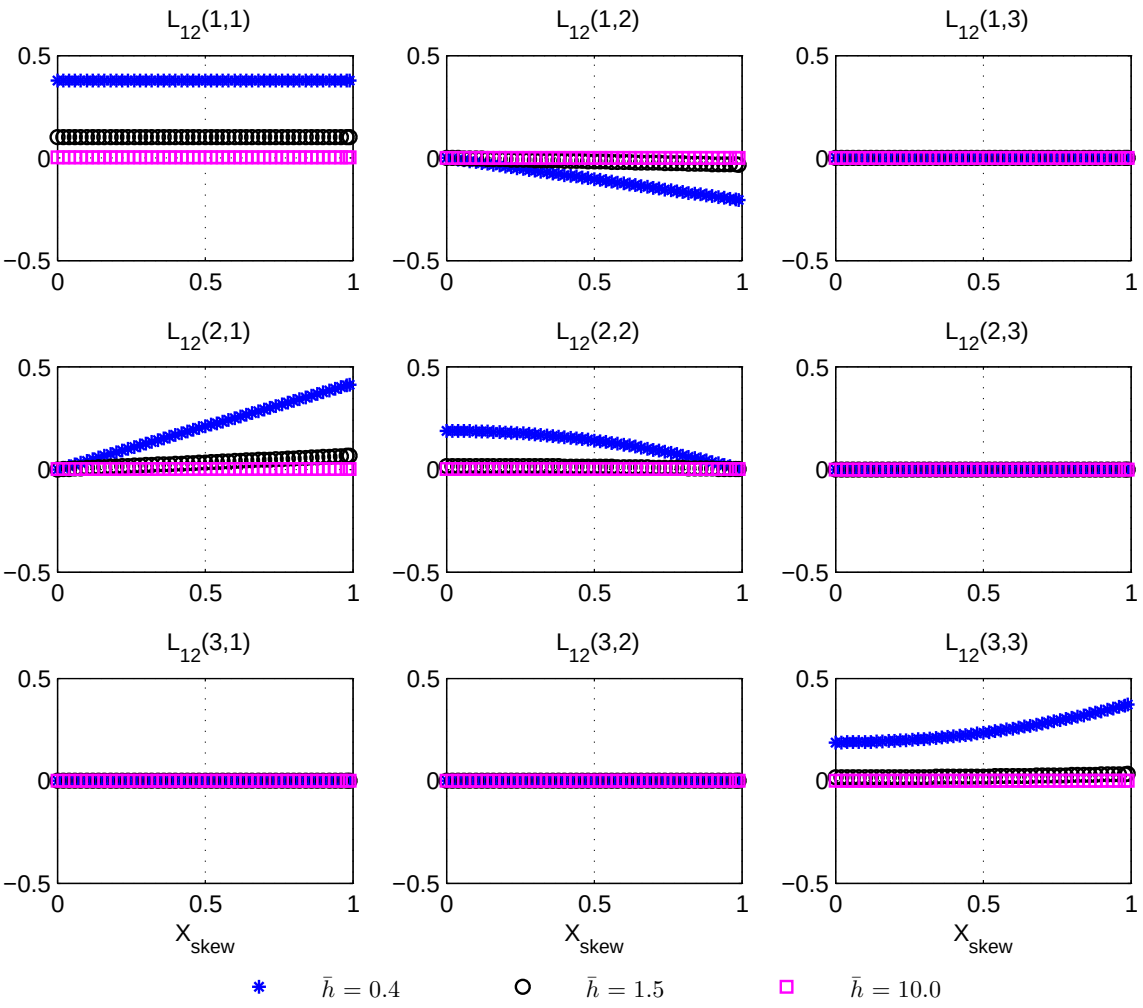

Figure D.2: Precalculated elements in three-state coaxial rotor PPSIM $[L_{12}]$ corresponding to different rotors separation distances, $\bar{h}$

REFERENCES

[1] "Department of Defense Interface Standard, Flying Qualities of Piloted Aircraft," Tech. Rep. MIL-STD-1797A, Notice 3, 2004.

[2] Adams, R., Buffington, J., Sparks, A., and S.S., B., "An Introduction to Multivariable Flight Control System Design," Tech. Rep. WL-TR-92-3110, 1992.

[3] Advanced Rotorcraft Technology, Inc., *FLIGHTLAB X-Analysis User Manual*, July 2013.

[4] Cameron, C., Karpatne, A., and Sirohi, J., "Performance and Vibratory Hub Loads of a Mach-Scale Coaxial Rotor in Hover," in *Proceedings of the AHS 70th Annual Forum, Montréal, Canada*, May 2014.

[5] Chen, R. and Hindson, W. S., "Influence of Dynamic Inflow on the Helicopter Vertical Response," NASA Technical Memorandum 88327, June 1986.

[6] Egolf, T., Reed, E., Rajmohan, N., and Sankar, L., "A Hybrid CFD Method for Coaxial Rotor Performance Prediction in Forward Flight," Presented at the AHS Aeromechanics Specialist's Conference, San Francisco, California, Jan. 2010.

[7] Harrington, R., "Full-Scale Tunnel Investigation of the Static Thrust Performance of a Coaxial Helicopter Rotor," NACA TN 2318, Mar. 1951.

[8] He, C. and Peters, D., "An Aeroelastic Analysis with a Generalised Wake," Proceedings of the AHS International Technical Specialist's Meeing on Rotorcraft Basic Research, Mar. 1991.

[9] He, C., Syal, M., Tischler, M. B., and Juhasz, O., "State-space Inflow Model Identification from Viscous Vortex Particle Method for Advanced Rotorcraft Configurations," in *Proceeedings of the 73rd Annual Forum*, May 2017.

[10] He, C. and Zhao, J., "A Real Time Finite State Induced Flow Model Augmented with High Fidelity Viscous Vortex Particle Simulation," in *Proceedings of the AHS 64th Annual Forum*, May 2008.

[11] He, C. and Zhao, J., "Modeling Rotor Wake Dynamics with Viscous Vortex Particle Method," *AIAA Journal*, vol. 47, 2009.

[12] Joglekar, M. and Loewy, R., "An Actuator-Disc Analysis of Helicopter Wake Geometry and the Corresponding Blade Response," USAAVLABS Technical Report 69-66, Dec. 1970.

[13] Kim, H. W. and Brown, R. E., "A Comparison of Coaxial and Conventional Rotor Performance," *Journal of the American Helicopter Society*, vol. 55, Jan. 2010.

[14] Kim, J., Sankar, L. N., and Prasad, J. V. R., "Application of a Navier-Stokes Free Wake Hybrid Methodology to the Harrington Coaxial Rotor," in *Proceedings of the AHS Technical Meeting on Aeromechanics Design for Vertical Lift, San Francisco, California*, Jan. 2016.

[15] Koehl, A., Rafaralahy, H., Boutayeb, M., and Martinez, B., "Aerodynamic Modelling and Experimental Identification of a Coaxial-Rotor UAV," *Journal of Intelligent and Robotic Systems*, vol. 68, 2012.

[16] Kong, Y. B., Prasad, J. V. R., and He, C., "Finite State Coaxial Rotor Inflow Model Enhancements using System Identification," *Journal of the American Helicopter Society*, 2018. Submitted manuscript under review.

[17] Kong, Y. B., Prasad, J. V. R., Sankar, L. N., and He, C., "Finite State Inflow Flow Model for Coaxial Rotor configuration," *Journal of the American Helicopter Society*, 2018. Submitted manuscript under review.

[18] Kong, Y. B., Prasad, J. V. R., Sankar, L. N., and Kim, J., "Finite State Coaxial Rotor Inflow Model Improvements via System Identification," Proceedings of the AHS 72nd Annual Forum, West Palm Beach, Florida, May 2016.

[19] Kong, Y. B., Prasad, J. V. R., Sankar, L. N., and Peters, D. A., "Finite State Coaxial Rotor Inflow Model System Identification using Perturbation approach," Presented at the Asia-Australian Rotorcraft Forum, Singapore, Nov. 2016.

[20] Kundak, N., Rhinehart, M., and Mettler, B., "Modeling and Control Design for Miniature Autonomous Coaxial Rotorcraft," in *Proceedings of the AHS 64th Annual Forum, Montréal, Canada*, May 2008.

[21] Lakshminarayan, V. K. and Baeder, J. D., "High-Resolution Computational Investigation of Trimmed Coaxial Rotor Aerodynamics in Hover," *Journal of the American Helicopter Society*, vol. 54, 2009.

[22] Lebedev, N. N., *Special Functions and Their Applications*. Englewood Cliffs, N.J., Prentice-Hall, Rev. English ed. translated and edited by Richard, A.S. ed., 1965.

[23] Lim, J. W., McAlister, K. W., and Johnson, W., "Hover Performance Correlation for Full-Scale and Model-Scale Coaxial Rotors," *Journal of the American Helicopter Society*, vol. 54, 2009.

[24] McAlister, K. W. and Tung, C., "Experimental Study of a Hovering Coaxial Rotor with highly Twisted Blades," in *Proceedings of the AHS 64th Annual Forum, Montréal, Canada*, May 2008.

[25] Mettler, B., Tischler, M., and Kanade, T., "System Identification Modeling of a Model-Scale Helicopter," Tech. Rep. CMU-RI-TR-00-03, Carnegie Mellon University, Pittsburgh, PA, 2000.

[26] Neal, T. and Smith, R., "An In-Flight Investigation to Develop Control System Design Critera for Fighter Airplanes," Tech. Rep. AFFDL-TR-70-74, Volume I, 1970.

[27] Nischint, R., *Application of Hybrid Methodology to Rotors in Steady and Maneuvering fFlight*. PhD thesis, Georgia Institute of Technology, Aug. 2010.

[28] Nowak, M., Prasad, J. V. R., and Peters, D., "Development of a Finite State Model for a Coaxial Rotor in Forward Flight," in *Proceedings of the AHS 70th Annual Forum*, May 2014.

[29] Nowak, M., Prasad, J. V. R., Xin, H., and Peters, D. A., "A Potential Flow Model for Coaxial Rotors in Forward Flight," in *Proceedings of the 39th European Rotorcraft Forum, Moscow, Russia*, 2013.

[30] Ormiston, R. A. and Peters, D. A., "Hingeless Helicopter Rotor Response with Nonuniform Inflow and Elastic Blade Bending," *Journal of Aircraft*, vol. 9, Apr. 1972.

[31] Peters, D. and He, C., "Finite State Induced Flow Models Part II: Three-Dimensional Rotor Disk," *Journal of Aircraft*, vol. 32, Mar. 1995.

[32] Peters, D. A., "Hingeless Rotor Frequency Response with Unsteady Inflow," in *Rotorcraft Dynamics*, NASA, Jan. 1974.

[33] Peters, D. A., Barwey, D., and Su, A., "An Integrated Airloads-Inflow Model for Use in Rotor Aeroelasticity and Control Analysis," in *Proceedings of the 47th Annual National Forum of the American Helicopter Society, Phoenix, Arizona*, May 1994.

[34] Peters, D. A., Boyd, D. D., and He, C., "Finite-State Induced Flow Model for Rotors in Hover and Forward Flight," *Journal of the American Helicopter Society*, vol. 34, Oct. 1989.

[35] Peters, D. A. and He, C., "Correlation of Measured Induced Velocities with a Finite-State Wake Model," *Journal of the American Helicopter Society*, vol. 36, pp. 59–70, 1991.

[36] Pitt, D. M. and Peters, D. A., "Theoretical Prediction of Dynamic Inflow Derivatives," *Vertica*, vol. 5, Mar. 1981.

[37] Rand, O. and Khromov, V., "Free-Wake Based Dynamic Inflow Model for Hover, Forward and Maneuvering Flight," in *Proceedings of the American Helicopter Society 72nd Annual Forum, West Palm Beach, FL*, May 2016.

[38] Rand, O., Khromov, V., Hersey, S., Celi, R., J. O., and Tischler, M., "Linear Inflow Model Extraction from High-Fidelity Aerodynamic Models for Flight Dynamics Applications," in *Proceedings of the American Helicopter Society 71st Annual Forum, Virginia Beach, VA*, May 2015.

[39] Su, A., Yoo, K. M., and Peters, D. A., "Extension and Validation of an Unsteady Wake Model for Rotors," *Journal of Aircraft*, vol. 29, pp. 374–383, 1992.

[40] Tischler, M. B. and Remple, R. K., *Aircraft and Rotorcraft System Identification*. American Institute of Aeronautics, 2012.

[41] US Army Research, Development, and Engineering Command, *Rotorcraft Comprehensive Analysis System User's Manual*, Aug. 2012.

[42] Wayne, J., *Rotorcraft Aeromechanics*. Cambridge University Press, 2013.

[43] Whitehouse, G. R. and Boschitsch, A. H., "Innovative Grid-Based Vorticity-Velocity Solver for Analysis of Vorticity-Dominated Flows," *AIAA Journal*, vol. 53, pp. 1655–1669, 2015.

[44] Whitehouse, G. R., Boschitsch, A. H., Quackenbush, T. R., Wachspress, D. A., and Brown, R. E., "Novel Eulerian Vorticity Transport Wake Module for Rotorcraft Flow Analysis," in *63rd Annual Forum of the American Helicopter Society, Virgina Beach, VA*, May 2007.

[45] Whitehouse, G. R., Boschitsch, A. H., Smith, M. J., Lynch, C. E., and Brown, R. E., "Investigation of Mixed Element Hybrid Grid-Based CFD Methods for Rotorcraft Flow Analysis," in *66th Annual Forum of the American Helicopter Society, Phoenix, AZ*, May 2010.

[46] Whitehouse, G. R. and Tadghighi, H., "Investigation of Hybrid Grid-Based CFD Methods for Rotorcraft Flow Analysis," *Journal of the American Helicopter Society*, vol. 56, pp. 1–10, 2011.

[47] Xin, H., Goss, J., and Parkes, C., "Development of a Three-State Rotor Interfence Model and Application to Coaxial Rotor Inflow Modeling," Presented at the Fifth Decennial AHS Aeromechanics Specialists' Conference, San Francisco, California, Jan. 2014.

[48] Yoon, S., Chan, W. M., and Pulliam, T. H., "Computations of Torque-Balanced Coaxial Rotor Flows," in *AIAA SciTech Forum, Grapevine, Texas*, Jan. 2017.

[49] Yoon, S., Lee, H. C., and Pulliam, T. H., "Computational Study of Flog Interactions in Coaxial Rotors," in *Proceedings of the AHS Technical Meeting on Aeromechanics Design for Vertical Lift, San Francisco, California*, Jan. 2016.

[50] Zhao, J. and He, C., "Real-Time Simulation of Coaxial Rotor Configurations with Combined Finite State Dynamic Wake and VPM," in *Proceedings of the AHS 70th Annual Forum*, May 2014.

VITA

Yong-Boon received his Bachelor and Master of Science degrees in Mechanical Engineering from the National University of Singapore, Singapore. He was accepted to the School of Aerospace Engineering at the Georgia Institute of Technology in Fall 2013 and passed his qualifying exams a year later. His research interest focuses on simulation and modeling of rotor inflows, especially in multi-rotor configurations. Yong-Boon took part in the 31st AHS Graduate Student Design Competition in 2014 and his team won the top place. He is currently a member of the American Helicopter Society.